



**University of  
Nottingham**

UK | CHINA | MALAYSIA

# **Additively-Manufactured tooling solutions for Orthopedic surgeries**

By Bixuan Wang

Supervisors Prof. Haonan Li

Dr. Yinfeng He

Dr. Kean How Cheah

Dr. Salman Ijaz

A PhD thesis submitted for the degree of PhD of  
Mechanical Engineering of Nottingham University

Department of Mechanical, Materials, and  
Manufacturing Engineering

March 2025

**(This page is left blank)**

## **Abstract**

Orthopedic conditions such as craniosynostosis and osteonecrosis of the femoral head (ONFH) are highly concerning due to their high incidence rates, surgical complexity, and potential for severe postoperative complications. In craniosynostosis surgery, grinding techniques can generate the risk of thermal buildup, which poses a serious threat to surrounding brain or nerve tissues and irreversible complications. In ONFH surgery, it also involves complex procedures (including incision, guide wire insertion, drilling, curettage, and bone implantation), which introduces significant risks such as fractures and recurrent non-traumatic bone necrosis.

To address the above issues, three innovative surgical tooling solutions are developed using additive manufacturing techniques in this thesis.

### **(i) Ceramic hollow grinding tool**

For craniosynostosis surgery, the 3D-printed ceramic hollow grinding tool is proposed and fabricated to facilitate the coolant delivery into the bone grinding area, thereby generating more effective cooling performance. The CFD simulation and experiments prove that the new design enables more coolant to reach the surgery zone, limiting the heat accumulation and flushing away removed bone debris. In the in vivo test, the new tool produces less apoptosis and edema area to the rat brain in comparison with that of conventional tools.

### **(ii) Closed-loop temperature control grinding device**

For craniosynostosis surgery, the novel grinding device is proposed to continuously monitor the grinding temperature and precisely apply coolant

## **Abstract**

---

when needed. The customized grinding tool is created with the embedded temperature sensors and the coolant channels. Our device effectively maintains the grinding surface temperature within the surgeon-defined range, with the latency of less than 1 second. Furthermore, our design not only ensures the coolant spray outlets remain unobstructed by debris during grinding, but also effectively removes debris at the interface. Our design might reduce the risk of potential complications, such as bone hyperplasia.

### **(iii) Multifunctional ceramic tool**

For ONFH surgery, the multifunctional ceramic surgery tool is innovatively designed and additively manufactured for early-stage ONFH treatment. The multifunctional tool can not only act as a drilling tool, but also retain itself in the drilled hole as a bone scaffold. At the meantime, the tool can delivery active ingredient (Vitamin C) for fast recovery. The proposed tool is additively manufactured with the inter-connected pore structures (with the porosity of 50%, 70% and 80%). The tool not only meets required mechanical properties, but also shows drug releasing function with controllable diffusion rates in the experiments. The ceramic tool with Vitamin C coating also enhances cell adhesion and accelerates cell growth based on the osteoblast induction assessment.

The above three designed tools minimize complication occurrence in craniosynostosis and ONFH surgery, opening new opportunities for the development of orthopedic surgical tools using additive manufacturing technology.

## Acknowledgements

I would like to sincerely thank my supervisor Prof. Haonan Li. His every look and every word were tremendous encouragement to me. From the beginning of my PhD journey, his recognition and appreciation made me quickly find direction in my research topics. During moments of setbacks and discouragement, he helped me find new ideas and never gave up on me. When my paper was accepted, he encouraged and affirmed me, and reminded me that continuous breakthroughs lead to greater achievements. While I was presenting in front of the audience, his affirmative and gratified eyes always made me unforgettable.

I feel very fortunate to have met my supervisor Prof. Haonan Li, and it is a great honor to be a member of his research group. During my four years of pursuing my PhD, he had fully supported my research, providing all the necessary experimental conditions, including funding, equipment, and personnel. It allowed me to experience the convenience and freedom of conducting experiments. He was always patient and meticulous. His word-by-word revisions of my thesis and his tireless guidance on my questions, have made me realize the silent dedication and meticulous care that a teacher provides to their students.

At the same time, I would like to sincerely thank Prof. Yinfeng He for his guidance and support in my work. During the last two years of my PhD, from

## Acknowledgements

---

selecting the topic to conducting experiments and writing the paper, everything was completed under his careful guidance and was successfully accepted. His profound theoretical foundation, rich practical experience, and rigorous academic attitude in the field of additive manufacturing have greatly benefited me.

Secondly, I would also like to thank Director Peng Wei, Director Jin Mei, Dr. Wei Su, Dr. Ying Chen from the First Affiliated Hospital of Ningbo University, and Qi Huan, Long Shanshan, and Su Jie. I am grateful for your assistance providing for some of my experiments. It was your strong support that made the implementation and successful completion of the experiments possible.

Finally, I would like to thank my junior colleagues in the research group, my undergraduate students, my friends, and my family. (YChendan Tang, Chenglong Hua, Qingfeng Li et, al.) Your companionship and support were my driving force and precious treasures in my life. Thank you all. The road ahead is still long, and I will always carry a grateful heart, taking each step steadily to create my own future. I know that on this journey, you are all right by my side.

## Originality Statement and Helps from Technicians

In this thesis, I received a few of assistance from technicians, including

1 - Helps from medical technologist with guidance and experimentation in the direction of medicine.

Except for the above helps, I hereby declare that all the other efforts in this academic dissertation are taken by myself under the guidance of my supervisors.

To the best of my knowledge, the work presented in this dissertation is original and does not contain any research achievements published or written by others.

A handwritten signature in black ink, appearing to be in Chinese characters, located below the text of the originality statement.

Author signature

# Research Ethics Checklist for Staff and Research Students



## Research Ethics Checklist for Staff and Research Students

### [strongly informed by the ESRC (2012) Framework for Research Ethics]

A checklist should be completed for **every** research project or thesis where the research involves the **participation of people, the use of secondary datasets or archives relating to people and/or access to field sites or animals**. It will be used to identify whether a full application for ethics approval needs to be submitted.

**You must not begin data collection or approach potential research participants until you have completed this form, received ethical clearance, and submitted this form for retention with the appropriate administrative staff.**

The principal investigator or, where the principal investigator is a student, the supervisor, is responsible for exercising appropriate professional judgement in this review.

Completing the form includes providing brief details about yourself and the research in Sections 1 and 2 and ticking some boxes in Sections 3 and/or 4 or 5, **Ticking a shaded box in Sections 3, 4 or 5 requires further action by the researcher.** Two things need to be stressed:

- Ticking one or more shaded boxes does **not** mean that you cannot conduct your research as currently anticipated; however, it does mean that further questions will need to be asked and addressed, further discussions will need to take place, and alternatives may need to be considered or additional actions undertaken.
- Avoiding the shaded boxes does **not** mean that ethical considerations can subsequently be 'forgotten'; on the contrary, research ethics - for everyone and in every project - should involve an ongoing process of reflection and debate.

If you have **not** ticked any shaded boxes, please submit the completed form to the Faculty's Research Ethics Officers, with any further required documents, for approval and record-keeping.

If you have ticked any shaded boxes **you will need to describe more fully how you plan to deal with the ethical issues raised by your research.** Please submit this completed form to the Faculty's Research Ethics Officers, who will decide whether your project requires further review by the UNNC Research Integrity and Ethics Committee and/or whether further information needs to be provided.

The following checklist is a starting point for an ongoing process of reflection about the ethical issues concerning your study.

Ticket No.: REQ2024090454  
Approval No: FOSE-202425-002

SECTION 1: THE RESEARCHER(S)	
1.1 Name of principal researcher:*	<input type="text" value="Bixuan Wang"/>
1.2 Status: *	<input type="radio"/> Staff <input checked="" type="radio"/> Postgraduate research student
1.3 Faculty/Department:*	<input type="text" value="FoSE"/>
1.4 Email address: *	<input type="text" value="BIXUAN.WANG@NOTTINGHAM.EDU.CN"/>
1.5 Names of internal project members (if applicable):	<input type="text"/>
1.6 Names of external project members (if applicable):	<input type="text" value="Preventing Thermal Osteonecrosis through 3D Printed Ceramic Grinding Tool"/>
1.7 Names of Supervisors (if applicable):	<input type="text"/>
1.8 I have read the <i>University of Nottingham's Code of Research Conduct and Research Ethics (2023)</i> and agree to abide by it: <a href="#">Code-of-research-conduct-and-research-ethics.pdf*</a>	<input checked="" type="radio"/> YES
1.9 (If applicable) I have familiarized myself with the <i>Research Ethics Guidance for Social Media and Internet Mediated Research</i> accessible at: <a href="#">Social Media Research final v1 13 June 2023.pdf *</a>	<input checked="" type="radio"/> YES <input type="radio"/> N/A
1.10 FoSE - Please read the <a href="#">List of Points to consider when submitting and Ethics Review (taken from ESRC (2012) Framework for Research Ethics)</a> and attach your response. *	<input type="text" value="LIST OF POINTS TO CONSIDER"/>

## Research Ethics Checklist for Staff and Research Students

2.1: Title of project:*	<p>Please provide brief details about your proposed research, as indicated in each section.</p> <div style="border: 1px solid #ccc; padding: 5px; min-height: 50px;">                     Preventing Thermal Osteonecrosis through 3D Printed Ceramic Grinding Tool                 </div>
2.2: Proposed start date and end date of the project:*	<div style="display: flex; align-items: center; gap: 10px;"> <input style="width: 60px;" type="text" value="2024-09-20"/> ~ <input style="width: 60px;" type="text" value="2024-10-01"/> </div>
2.3: Research question(s) or aim(s)*	<div style="border: 1px solid #ccc; padding: 5px; min-height: 50px;"> <p>Research Aim: To design a hollow ceramic grinding tool enabled by additive manufacturing that minimizes the occurrence of complications such as osteonecrosis due to high surgical temperatures. The specific problems being address are in the inability: (i) restrict the heat accumulations, and remove excessive bone debris. (ii) less apoptosis and edema area to the rat brain.</p> </div>
2.4: Summary of method(s) of data collection*	<div style="border: 1px solid #ccc; padding: 5px; min-height: 50px;"> <p>Sprague Dawley rats, aged 6 to 8 weeks, were selected for the study and divided into three groups: the control group, the conventional solid tool group, and the proposed hollow tool group (n=6). The procedure was as follows: each rat was anesthetized with ketamine (60 mg/kg i.p. for rats; 100 mg/kg i.p. for mice) and then secured on an animal operating table. The fur on the rat's head was shaved and cleansed with iodine before making an incision. The skin and muscle tissue of the head were then cut away to fully expose the skull. The grinding tool was used to grind the skull at the</p> </div>
2.5: Proposed site(s) of data collection *	<div style="border: 1px solid #ccc; padding: 5px; min-height: 50px;"> <p>All data is collected in the animal laboratory of the First Affiliated Hospital of Ningbo University. The animal laboratory is located in Room 2010, 20th floor, Construction Bank Building, First Affiliated Hospital of Ningbo University. The data collection method is detailed in Section 2.4. The collected data is stored at the First Affiliated Hospital of Ningbo University.</p> </div>
2.6: How will access to participants and/or sites be gained? *	<div style="border: 1px solid #ccc; padding: 5px; min-height: 50px;"> <p>Wei Su is a doctor at the First Affiliated Hospital of Ningbo University, responsible for the animal experiments in this project. Wei Su is aware of the animal experiment purpose of this project and understands his role in the animal experiment.</p> </div>

### SECTION 3: RESEARCH INVOLVING USE OF SECONDARY DATASETS OR ARCHIVES RELATING TO PEOPLE

If your research involves use of secondary datasets or archives relating to people, all questions in Section 3 **must** be answered. If it does not, please tick the 'NOT APPLICABLE' box and go to Section 4.

NOT APPLICABLE

### SECTION 4: RESEARCH INVOLVING ACCESS TO FIELD SITES AND ANIMALS

If your research involves access to field sites and/or animals, all questions in Section 4 **must** be answered. If it does not, please tick the 'NOT APPLICABLE' box and go to Section 5.

NOT APPLICABLE

Please answer each question by ticking the appropriate box.

4.1: Do you have permission to access the site?*	<input checked="" type="radio"/> YES <input type="radio"/> NO
4.2: Does the site have an official protective designation of any kind?*	<input type="radio"/> YES <input checked="" type="radio"/> NO
4.3: Will this research place the site, its associated wildlife and other people using the site at any greater physical risks than are experienced during normal site usage?*	<input type="radio"/> YES <input checked="" type="radio"/> NO
4.4: Will this research involve the collection of any physical materials from the site?*	<input type="radio"/> YES <input checked="" type="radio"/> NO
4.5: Is there any potential for exposing the researcher(s) to any significant risk of physical or emotional harm?*	<input type="radio"/> YES <input checked="" type="radio"/> NO
4.6: Will the research involve vertebrate animals (fish, birds, reptiles, amphibians, mammals) or the common octopus ( <i>Octopus vulgaris</i> ) in any capacity?*	<input checked="" type="radio"/> YES <input type="radio"/> NO

# Research Ethics Checklist for Staff and Research Students

a) If yes, will the research with vertebrates or octopi involve handling or interfering with the animal in any way or involve any activity that may cause pain, suffering, distress or lasting harm to the animal?\*

YES     NO

Explanatory: (Since you typed 'YES' in 4.6.a, please provide an explanation.) \*

Each rat was anesthetized with ketamine (60 mg/kg i.p. for rats; 100 mg/kg i.p. for mice) and then secured on an animal operating table. The fur on the rat's head was shaved and cleansed with iodine before making an incision. The skin and muscle tissue of the head were then cut away to fully expose the skull. The grinding tool was used to grind the skull at the same location for each group.

## SECTION 5: RESEARCH INVOLVING THE PARTICIPATION OF PEOPLE

If your research involves the participation of people all questions in Section 5 **must** be answered.

NOT APPLICABLE

Additional attachment:

Please note that it is your responsibility to follow the University's Code of Research Conduct and Research Ethics and any relevant academic or professional guidelines in the conduct of your study. **This includes providing appropriate information sheets and consent forms, and ensuring confidentiality in the storage and use of data. For guidance and UK regulations on the latter, please refer to** the Data Protection Policy and Guidelines of the University of Nottingham.  
 Policy and guidelines - <https://www.nottingham.ac.uk/governance/records-and-information-management/data-protection/data-protection-policy.aspx>  
 The University of Nottingham Ningbo China Data Management Policy can be found here: [UNNC Data Management Policy \(provisional\).pdf](#)

**Any significant changes in the project, i.e. research question(s), design or conduct over the course of the research should be notified to the Faculty's Research Ethics Officers and may require a new application for ethical approval.**

### Faculty Research Ethics Panel Review Instructions

If the project triggers one or more of the criteria specified in section 4.1 of the *Code of Practice for Research Ethics Review Committees* ([Code of Practice for Research Ethics Committees \(CoPREC\) v3 12 Dec 2023.pdf](#)), it should be reviewed by the UNNC Research Integrity and Ethics Committee\*

- **Approve** (the research can go ahead as planned)
- **Return to Initiator** (further information or amendments are needed to the research protocol)
- **Transfer to Joanna Huang** (refer to UNNC Research Integrity and Ethics Committee)
- **Reject**

### Approval Information

No.	Step Name	Sign	Action	Date	Comments
1	Start	Bixuan Wang	submit	2024-09-18 19:34	
2	Supervisor	Haonan Li	Approve	2024-09-19 02:22	
3	Ethics officers	Byung Gyoo Kang	Return to Initiator	2024-09-24 14:35	The University expects data to be retained for a minimum of 7 years. Please revise Q16 in A. LIST OF POINTS TO CONSIDER WHEN SUBMITTING AN ETHICS REVIEW.
4	Ethics officers	Byung Gyoo Kang(Owner:Sherif Welsen)	Return to Initiator	2024-09-24 14:35	The University expects data to be retained for a minimum of 7 years. Please revise Q16 in A. LIST OF POINTS TO CONSIDER WHEN SUBMITTING AN ETHICS REVIEW.
5	Start	Bixuan Wang	submit	2024-09-24 16:27	
6	Supervisor	Haonan Li	Approve	2024-09-24 20:08	
7	Ethics officers	Byung Gyoo Kang	Approve	2024-09-25 16:04	
8	Ethics officers	Sherif Welsen	Approve	2024-09-26 15:52	
9	End			2024-09-26 15:52	Approved

---

## Publications

### Paper published

[1] **B.X. Wang**, Y.J. Zhao, G.Y. Liu, C.K. Thein, W. Su, S.S. Long, H. Qi, P. Wei, Y.F. He#, H.N. Li#, Preventing Thermal Osteonecrosis through 3D Printed Ceramic Grinding Tool. *Additive Manufacturing*, 2023: p. 103878. (Impact factor: 11, JCR Q1 journal)

[2] **B.X. Wang**, G.Y. Liu, Y.J. Zhao, B. Wang, Q.Z. Bi, R. Pierce, H. Qi, X.W. Fang, H.N. Li#, On the creation of structured abrasive tools via multiple-pass rotary wire EDM: A geometrical model. *The International Journal of Advanced Manufacturing Technology*, 2023. 126: p. 3503-3522. (Impact factor: 3.4, JCR Q1 journal)

[3] **B.X. Wang**, K.Y. Li, G.Y. Liu, L.Y. Xia, W.N. Guan, J.T. Guo, J. Xu, Y. Nie, Y.J. Zhao, Y.F. He#, H.N. Li#, Integrating 3D Printed Grinding Tools and Closed-Loop Temperature Management for Optimal Surgical Outcomes. *Advanced Materials Technologies*. (Impact factor: 6.8, JCR Q1 journal)

[4] **B.X. Wang**, Y.J. Zhao, G.Y. Liu, Y. Chen, M. Jin, L.Y. Xia, C.D. Tang, H. Qi, Y.F. He#, H.N. Li#, 3D printed zirconia ceramic tool for bone repair with multifunction of drug release, drilling and implantation. *Ceramics International*, 2024, ISSN 0272-8842. (Impact factor: 5.2, JCR Q1 journal)

[5] Y.T. Ma, Z.N. Tian, **B.X. Wang**, Y.J. Zhao, Y. Nie, R.D. Wildman, H.N. Li#, Y.F. He#, Enhancing the 3D printing fidelity of vat photopolymerization with

## Publications

---

machine learning-driven boundary prediction. *Materials & Design*, 2024, 241: 112978.

## Patents under review

[1] H.N. Li, **B.W. Wang**, P. Wei, W. Su, H. Qi, C.D. Tang, L.Y. Xia, G.Y. Liu, A hollow grinding wheel with cooling and chip removal functions and its preparation method (invention patent), 2023, CN202311171356.7.

[2] H.N. Li, **B.W. Wang**, Y. Chen, J. Mei, H. Qi, G.Y. Liu, L.Y. Xia, C.D. Tang, A hollow bone drill with medicine delivery function and preparation method (invention patent), 2023, CN202311103198.1.

[3] H.N. Li, **B.W. Wang**, K.Y. Li, L.Y. Xia, J.T. Guo, W.N. Guan, Integrated grinding device, usage method and control system for real-time temperature measurement and cooling (invention patent), 2024, CN202410360939.2

## List of Figures

Figure 1-1: Two special orthopedic diseases: (a) patient, (b) CT and (c) surgery of craniosynostosis [7, 8]; (a) patient, (b) CT and (c) surgery of osteonecrosis of the femoral head [9, 10].	3
Figure 1-2: Problems in craniosynostosis and osteonecrosis of the femoral head surgeries: (a) ineffective cooling due to conventional solid grinding tools; (b) Lack of temperature monitoring and control; (c) a large number of surgical tools and complex surgical procedures.	6
Figure 1-3: Scope of the study.	9
Figure 2-1: Research on cooling strategies in craniosynostosis surgery: (a) irrigation cooling system, (b) spray cooling system and (c) cryogenic flushing system are based coolant supply technologies; (d) spherical metal bonded diamond grinding tool, (e) grinding tool with micro-groove structures, (f) tool with internal cooling channels and (g) grinding tool coated with a hydrophilic film based on new tools.	16
Figure 2-2: Research on Osteonecrosis of Femoral Head surgery steps: (a) single drilling, (b) multiple small-diameter drilling and (c) Innovative steerable drilling are drilling surgery step; (d) porous titanium alloy rods with diamond crystal lattice, (e) degradable magnesium scaffold, (f) porous tantalum scaffold and (g) bio-ceramic rod are implantation step; (h) subchondral injection and (i) porous titanium implant for drug delivery are drug delivery step.	20

**List of Figures**

---

Figure 2-3: Additively-manufactured tools: (a) metal-bonded diamond grinding tool; (b) porous structured diamond grinding tools; (c) resin bonded SiC grinding tool; (d) grinding tool with internal cooling channels and slots; (e) honeycomb-shaped triangular zirconia cutting tool, (f) ABS cutting tool; (g) damond-reinforced cutting tool; (h) Co-Cr-W superalloy cutting tool and (i) four-flute martensitic cutting tool. .... 23

Figure 3-1: the methodology that we followed to design, fabricate and verify our proposed hollow grinding tool: (a) design grinding tool with 3D Voronoi principle, (b) fabrication of designed grinding tool (c) testing & simulation for the coolant flow penetration, and verification of the grinding tool performance (d) in vitro and (e) in vivo. .... 26

Figure 3-2: Conceptual diagram of (a) conventional solid grinding tool and (b) the proposed hollow grinding tool. .... 27

Figure 3-3: A schematic of the proposed hollow grinding tool having: (a) scaffold structure aiming for coolant penetration (auxiliary grinding) and (b) solid structure aiming for effective material removal (effective grinding). .... 29

Figure 3-4: Design and Fabrication flow diagram: (a) 3D Voronoi design theory; (b) slicing process and (c) slice shape of each layer; (d-g) specific process for grinding tool fabrication. .... 31

Figure 3-5: Evaluation of the printed hollow grinding tools: (a) sample picture and (b-c) SEM morphological images of 3D printed hollow grinding tools; (d)

roundness test device and (e) dynamic balancing results; (f) tensile test and (g) obtained stress-strain curve between hollow and conventional grinding tool and (h) stress-strain curve after long-period grinding..... 34

Figure 3-6: Simulated result of the coolant behaviours: (a) the velocity vector of the proposed hollow grinding tool and (b) conventional solid grinding tool from the front view; (c) the average fluid velocity along the path from inlet to outlet along the jet direction by using proposed tool; (d) permeability of the coolant at different jet angles ( $5^\circ$  ,  $30^\circ$  ,  $45^\circ$  ). ..... 39

Figure 3-7: (a) Global and (b) detailed images of the experiment setup for coolant fluid permeability..... 41

Figure 3-8: Permeability of the coolant fluid: (a) Schematic diagram of our setup for assessing coolant fluid flow penetration and (b) cross section view, (c) experimental process and result diagram for hollow grinding tool, and (d) conventional grinding tool..... 42

Figure 3-9: temperature raise assessment; (a) experiment setup, b) front view of the grinded bone and c) temperature raise result for both the solid the hollowed grinding tool..... 44

Figure 3-10: (a) Global and (b) detailed images of the experiment setup for real bone grinding ..... 44

Figure 3-11: Comparison of the surface texture for the bone grinded with conventional solid grinding tool and hollow grinding tool: (a) 2D and (b) 3D

**List of Figures**

---

morphology of the real bone before grinding using the 3d profilometer; (c) 2D, (d) 3D morphology and (e) real picture of the grinded bone using conventional solid grinding tool; (f) 2D, (g) 3D morphology and (h) real picture of the grinded bone using proposed hollow grinding tool; microscopic images of (i) conventional solid grinding tool and (j) hollow grinding tool after grinding the bone. .... 46

Figure 3-12: In vivo experiment designed to compare the efficiency between conventional solid grinding tool and hollow grinding tool: (a) Schematic diagram of in vivo assessment process; Infrared thermogram in (b) control group, (c) conventional grinding tool group, and d) hollow grinding tool group; HE staining figure in (e) control group, (f) conventional grinding tool group, and (g) hollow grinding tool group; TUNEL staining figure in (h) control group, (i) conventional grinding tool group, and (j) hollow grinding tool group. .... 50

Figure 4-1: the methodology that we followed to design, fabricate and verify our proposed closed-loop grinding device: (a) design grinding tool and device, (b) fabrication of designed grinding tool (c) simulation for the coolant flow behavior, (d) testing the temperature control performance, and (e) verification of the grinding tool performance in vitro. .... 52

Figure 4-2: Conceptual diagram of (a) conventional open-loop grinding process and (b) proposed closed-loop temperature control grinding device. .... 54

Figure 4-3: A specific design diagram of grinding tool and device: concept design of (a) proposed grinding tool and (b) proposed closed-loop temperature control surgical device. .... 56

Figure 4-4: Electrical System diagram: blue) power supply module; green) motion module; red) sensor module; purple) display module; yellow) transmission module. .... 59

Figure 4-5: Fabrication diagram: (a) BLT printing process and (b) BLT printing principle. .... 61

Figure 4-6: Evaluation of the printed grinding tools: (a) sample picture and (b-d) SEM morphological images of 3D printed grinding tools; (e) dynamic balancing results; (f) tensile test and obtained load-strain curve..... 63

Figure 4-7: Simulated result of the coolant behaviours: (a) the coolant velocity vector in double cooling runners of proposed grinding tool and the velocity map of two jet ports in (b) cooling runner 1 and (c) cooling runner 2. .... 66

Figure 4-8: Closed loop experiment result for (a) before and (b) at critical temperature 37° C. .... 68

Figure 4-9: temperature control assessment; (a) global and (b) detailed images of the experiment setup, and (c) temperature control results for both grinding tool and grinding area. .... 71

**List of Figures**

---

Figure 4-10: Comparison of the surface texture for the bone and tool before and after grinding: (a)bone sample in grinding test; 2D and 3D morphology of the real bone (b) before grinding and (c) after grinding; real picture, microscopic images and EDS of proposed grinding tool (d) before and (e) after grinding and (f) after cleaning. .... 73

Figure 5-1: the methodology that we followed to design, fabricate and verify our proposed multifunctional ceramic tool: (a) concept and design of proposed multifunctional ceramic tool, (b) fabrication of designed ceramic tool; verification of the multifunctional ceramic tool in (c) drug releasing ability, (d) bone drilling ability, and (e) implantation ability..... 77

Figure 5-2: Conceptual diagram of (a) proposed ceramic tool; schematic diagram of (b) early treatment of femoral head necrosis and (c) drug permeates in bone. .... 78

Figure 5-3: A schematic of the (a) proposed ceramic tool having: (b) solid front cutter face, (c) solid cutting edge and (d) quick-change coupler connection point. .... 80

Figure 5-4: Design and Fabrication flow diagram: (a) Gyroid Triply Periodic Minimal Surface (Gyroid TPMS); (b) slicing process and (c) slice shape of each layer; (d) XJET ceramic 3D printing process and (e) XJET printing principle..... 81

Figure 5-5: Evaluation of the printed ceramic tool: (a) sample picture and (b-c) SEM morphological images of 3D printed tools; (d) cross-section cutting edge

accuracy evaluation, (e) tool model and (f) SEM morphological images of fracture surface; (g) tensile test set up and (h) obtained stress-strain curve via different porosity of tool. .... 83

Figure 5-6: Drug release properties: (a) Diffusion time chart of different excipient content; (b) Diffusion quantification analysis curve; Optical microscope and SEM images of ceramic tool (c) before and (d) after dip coating process. .... 86

Figure 5-7: Real bone drilling assessment: (a) Global and (b) detailed images of the experiment setup for real bone drilling; (c) CT scan image and (d) sample image of the drilled bone; (e) Schematic diagram and (f) 3D morphology of drilled hole. .... 90

Figure 5-8: Tool surface morphology comparison of the zirconia ceramic tool with 80% porosity before and after drilling: (a) SEM image and (b) EDS mapping of zirconia ceramic tool with 80% porosity before drilling; (c) SEM image and (d) EDS mapping of zirconia ceramic tool with 80% porosity after drilling. Tool wear comparison of the zirconia ceramic tool with 80%, 70% and 50% porosity after drilling: Optical microscope image of cutting blade of the drilled zirconia ceramic tool with (e) 80%, (f) 70% and (g) 50% porosity ..... 92

Figure 5-9: Osteoblast experiment designed to prove the efficiency of drug-loaded ceramic tool: (a-d) sample staining figure in POSITIVE CONTROL, G1, G2, and G3 group; (e-h) Microscope figure of calcium ion deposition in POSITIVE

**List of Figures**

---

CONTROL, G1, G2, and G3 group; (i) Microscope figure of ceramic tool without induced; Microscope figure of ceramic tool in G1, G2, and G3 group (j-l) after stained and (m-o) before stained..... 96

---

## Contents

Abstract .....	I
Acknowledgements .....	III
Originality Statement and Helps from Technicians.....	V
Publications .....	IX
List of Figures .....	XI
Contents .....	XIX
Chapter 1 Introduction.....	1
1.1 Background.....	1
1.1.1 Orthopedic disorders .....	1
1.1.2 Tools in orthopedic surgeries .....	3
1.2 Problem definition .....	5
1.3 Scope of the study .....	6
Chapter 2 Literature review & Research gaps.....	11
2.1 Cooling strategies in craniostygnosis surgery .....	11
2.1.1 Based on external coolant supply systems .....	11
2.1.2 Based on new tools.....	14
2.2 Operational programs in femoral head osteonecrosis surgery .....	16
2.2.1 Bone drilling step .....	16
2.2.2 Implantation step.....	17
2.2.3 Medication delivery step.....	19
2.3 Additively-manufactured tools.....	20
2.4 Summary of research gaps.....	23
Chapter 3 Hollow grinding tool .....	25
3.1 Introduction and motivation .....	25
3.2 The hollow grinding tool concept and structural design .....	26

## Contents

---

3.2.1 Concept.....	26
3.2.2 Structural design .....	27
3.3 The Fabrication and the geometrical/mechanical evaluation.....	29
3.3.1 Fabrication route.....	29
3.3.2 Geometrical and mechanical evaluation .....	31
3.4 The coolant flow penetration.....	34
3.4.1 CFD simulation.....	34
3.4.2 Experimental investigations .....	39
3.5 The in vitro assessment .....	42
3.5.1 Grinding temperature .....	42
3.5.2 Grinding trial on real bone .....	44
3.6 The in vivo assessment .....	47
3.6.1 Method.....	47
3.6.2 Results and discussion .....	48
Chapter 4 Closed-loop temperature control grinding device.....	51
4.1 Introduction and motivation .....	51
4.2 The closed-loop grinding device concept and design .....	52
4.2.1 Concept.....	52
4.2.2 Grinding tool design.....	54
4.2.3 Grinding device assembly .....	56
4.2.4 Electrical system design .....	57
4.2.5 Software system design .....	59
4.3 The Fabrication and the geometrical/mechanical evaluation.....	60
4.3.1 Fabrication route.....	60
4.3.2 Geometrical and mechanical evaluation .....	61
4.4 CFD simulation of internal cooling channel.....	64
4.4.1 Method.....	64

---

4.4.2 Results and discussion .....	65
4.5 Closed-loop and temperature control test .....	67
4.5.1 Closed-loop test .....	67
4.5.1 Temperature Fluctuation Assessment .....	68
4.6 Grinding trial on real bone .....	71
Chapter 5 Multifunctional ceramic tool.....	75
5.1 Introduction and motivation .....	75
5.2 Multifunctional ceramic tool concept and design .....	77
5.2.1 Concept.....	77
5.2.2 Structural design .....	78
5.3 The Fabrication and the geometrical/mechanical evaluation.....	80
5.3.1 Fabrication route.....	80
5.3.2 Geometrical and mechanical evaluation .....	81
5.4 Drug releasing ability .....	84
5.4.1 Qualitative drug diffusion experiment .....	84
5.4.2 Quantitative drug diffusion experiment .....	86
5.5 Bone drilling performance ability.....	88
5.6 Implantation ability through osteoblast induction assessment .....	93
5.6.1 Method .....	93
5.6.2 Results and discussion .....	94
Chapter 6 Conclusions.....	97
6.1 Research work summaries .....	97
6.2 Research findings and outcomes .....	98
References.....	101



# Chapter 1 Introduction

## 1.1 Background

### 1.1.1 Orthopedic disorders

In recent years, the number of patients with orthopedic disorder conditions is rapidly on the rise due to the aging of the global population and modern lifestyles characterized by prolonged sitting, lack of exercise, and poor dietary habits. In 2023, orthopedic disorder conditions affect approximately 1.71 billion people worldwide, accounting for 12.8% of total disease burden according to World Health Organization[1, 2]. Common orthopedic conditions include osteonecrosis of the femoral head (ONFH), craniosynostosis, arthritis, fractures, and spinal disorders. These conditions significantly limit patients' mobility and dexterity, and even lead to disability and life threat in severe cases.

Among the various orthopedic diseases, craniosynostosis and ONFH are widely recognized due to their unique pathological characteristics, clinical surgery complexity, and the high intraoperative risk.

#### **(i) Craniosynostosis**

Craniosynostosis is a serious orthopedic disease that mostly occurs in male newborns [3]. Approximately 150,000 to 200,000 infants are diagnosed with craniosynostosis each year in the world. Craniosynostosis is characterized by the premature fusion of one or more cranial sutures, which disrupts the typical

growth and development of an infant's skull and craniofacial structures [4].

Craniosynostosis may cause serious complications such as intracranial hypertension, skull deformity, and intellectual disability (see Figure 1-1 a, b).

The main purpose of craniosynostosis surgery is to correct skull shape through grinding techniques to ensure proper brain development and relieve intracranial hypertension. (Figure 1-1 c). The surgical area is close to critical brain structures, therefore any small mistakes may result in irreversible and even life-threatening brain tissue damage, cognitive impairment, other neurological deficits, or severe bleeding. Considering infants are a vulnerable group compared to adults, it requires high precision and meticulous attention during craniosynostosis surgery.

### **(ii) Osteonecrosis of the femoral head**

Osteonecrosis of the femoral head (ONFH) is one of the most common orthopedic diseases, with the 2-5 million cases worldwide [5]. ONFH refers to the condition where the blood supply to the femoral head is reduced or interrupted, leading to ischemic necrosis of bone tissue. This condition ultimately results in destruction and collapse of the femoral head. Without prompt treatment, the impaired hip joints, pain, stiffness, and limited mobility caused by ONFH can severely affect a patient's life and even lead to disability (Figure 1-1 d, e).

ONFH surgery mainly includes fracture reduction, bone grafting, and joint replacement (Figure 1-1 f). The femoral head is situated deep within the hip joint, therefore surgical area is restricted, posing major operation challenges. Although ONFH may not directly lead to death, this complex and challenging surgery can easily result in a high-risk or fatal complications (infection, and recurrence of non-traumatic osteonecrosis). The mortality rate after ONFH surgery is approximately 0.5% to 1.5% [6]. This rate tends to increase with patient's age and presence of complications.

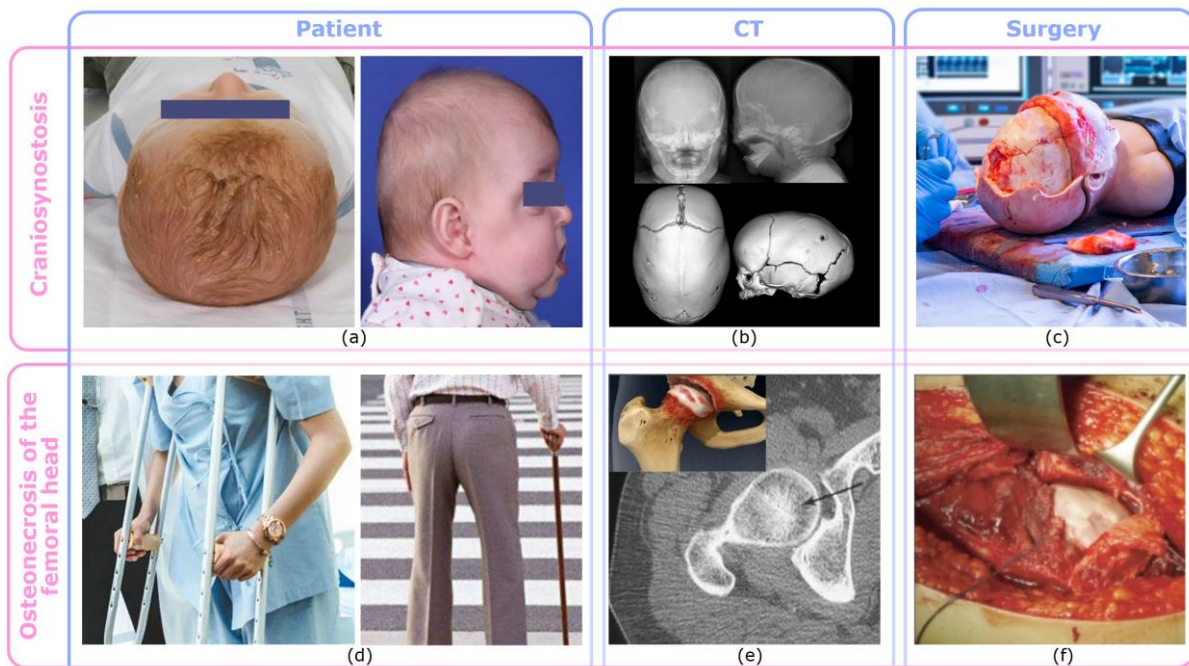


Figure 1-1: Two special orthopedic diseases: (a) patient, (b) CT and (c) surgery of craniosynostosis [7, 8]; (a) patient, (b) CT and (c) surgery of osteonecrosis of the femoral head [9, 10].

### 1.1.2 Tools in orthopedic surgery

The development of tools used for craniosynostosis and ONFH surgery is garnered significant attentions due to the increasing severity and the number

of patients affected by these two conditions. Conventional orthopedic tools (such as bone drills and bone grinding tools) require surgeons to manually control bone surgery details (such as temperature in the bone surgical area) and carefully manage the postoperative site (including removed bone debris), resulting in low surgical efficiency and complicated surgical procedures [11]. If conventional orthopedic tools are not properly operated, excessive temperature in surgical area can lead to bone tissue necrosis, and residual bone debris can increase the risk of postoperative infection. Based on above, conventional orthopedic tools are considered to be low efficiency and low precision, resulting in poor operational stability and high incidence of complications. Therefore, conventional orthopedic tools are no longer meet the current medical field demands.

In recent years, innovative cutting-edge technologies such as additive manufacturing are infiltrating all aspects of orthopedic tooling solutions. Conventional orthopedic tools are gradually being replaced by innovative orthopedic tools that are intelligentized and customized. These innovative orthopedic tools utilize sensors and control system to provide real-time surgical feedback and assist surgeons in decision-making. Additionally, innovative orthopedic tools with specialized porous structures (bone trabecular structures) are manufactured using additive manufacturing technology. These tools can be applied to bone implants to enhance the growth and adhesion of bone cells.

## 1.2 Problem definition

- In craniostyptosis surgery, bone grinding aims to remove excessive bone tissue through mechanical force, thereby correcting skull deformation or reducing bone irregularities [12]. However, the majority of the input power is converted into heat during the grinding process, resulting in unbearable heat accumulation in the grinded bone tissue. Conventional solid grinding tools used in craniostyptosis surgery bounce back a majority amount of coolant, resulting in ineffective cooling of the overheated surgical area (see Figure 1-2 a). Excessive temperature may damage peripheral brain nerve tissue [13] and cause bone cells to die, potentially leading to irreversible risks such as vision loss [14], control loss of facial muscle, or stroke [15] (see details in Chapter 3).
- In craniostyptosis surgery, the slight temperature variations in critical brain area can lead to permanent or irreversible brain damage (see details in Chapter 4). However, surgeons are unable to monitor real-time and in-process temperature changes in surgical area (see Figure 1-2 b), considering the existing cooling strategies for bone grinding are primarily empirical and based on skills or experiences.
- In ONFH surgery, the implantation of artificial bones or other materials into a patient's skeletal system aims to repair damaged bone structure and restore function and stability. Bone implantation operation is typically

performed in the middle and late stages of ONFH. This operation requires a large number of surgical tools (such as guide wires, surgical drills, cannulated reamers, curettes, etc.) and involves complex surgical steps (including incision, guide wire insertion, drilling, curettage, and bone implantation) (see Figure 1-2 c), contributing to a high failure rate ranging from 20% to 40%. (see details in Chapter 5).

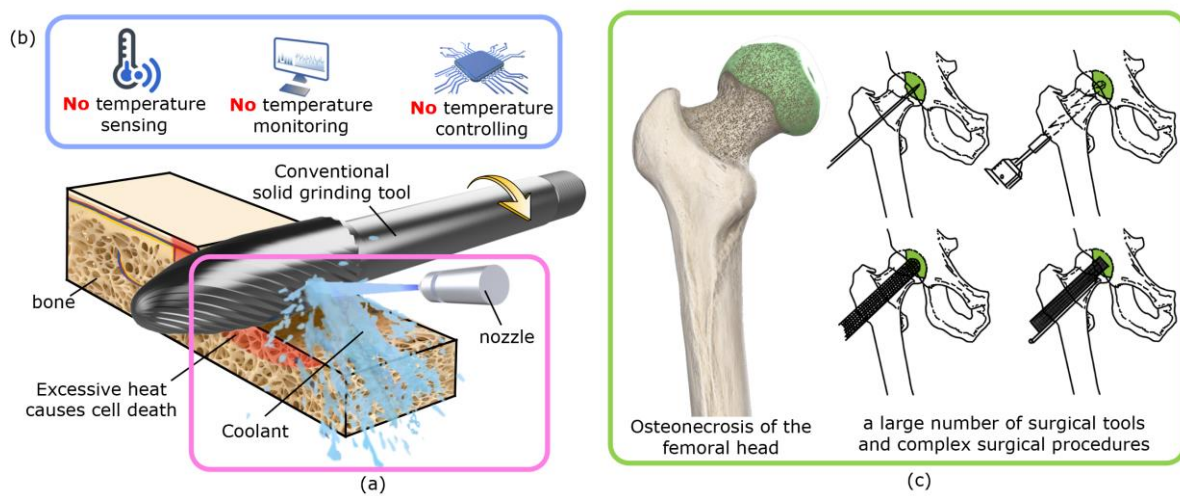


Figure 1-2: Problems in craniostylosis and osteonecrosis of the femoral head surgeries: (a) ineffective cooling due to conventional solid grinding tools; (b) Lack of temperature monitoring and control; (c) a large number of surgical tools and complex surgical procedures.

### 1.3 Scope of the study

To address series of surgical risks caused by conventional tools and surgical strategies, this thesis aims to explore innovative tooling solutions for craniostylosis and ONFH surgery in terms of design, fabrication, preliminary performances, and real in-vitro or in-vivo tests. The context of this thesis is as follows (see Figure 1-3):

Chapter 1 provides a general introduction, covering the background of orthopedic disorders and tools in craniosynostosis and ONFH surgery (Section 1.1). Three main issues in craniosynostosis and ONFH surgery are discussed in Section 1.2. The thesis structure is explained in Section 1.3.

Chapter 2 presents the detailed literature review regarding (i) cooling strategies in craniosynostosis surgery (Section 2.1), (ii) ONFH surgery (Section 2.2), and (iii) additively-manufactured tools (Section 2.3). Research gaps are proposed in Section 2.4.

Chapter 3 proposes the hollow grinding tool to solve the excessive temperature during craniosynostosis grinding surgeries. Section 3.1 provides an introduction and motivation of the proposed hollow tool. The tool is explained from the aspects of design (Section 3.2), fabrication (Section 3.3), coolant permeability test (Section 3.4), in-vitro assessment (Section 3.5), and in-vivo assessment (Section 3.6).

Chapter 4 proposes the conformal cooling grinding tool and a novel closed-loop temperature control bone grinding device. The proposed tool addresses the lack of precise temperature monitoring and regulating in craniosynostosis surgical area when using conventional tools and cooling strategies. Section 4.1 provides an introduction and motivation of the proposed closed-loop temperature control bone grinding device. The research is divided into the following sections: (i) closed-loop temperature control bone grinding device

design (Section 4.2), (ii) conformal cooling grinding tool fabrication (Section 4.3), (iii) internal cooling channels CFD simulation (Section 4.4), (iv) closed-loop and temperature control test (Section 4.5), and (v) in vitro assessment (Section 4.6).

Chapter 5 introduces the novel multifunctional ceramic tool that can simultaneously act as a bone drilling instrument, a bone scaffold, and an ingredient delivery device in ONFH surgery. The proposed multifunctional ceramic tool aims to address complex ONFH surgical procedures (including incision, guide wire insertion, drilling, curettage, and bone implantation) and the excessive employment of tens of surgical tools (such as surgical drill, guide wires, cannulated reamers, curettes, etc.). Section 5.1 provides an introduction and motivation regarding the reasons for proposing the multifunctional ceramic tool. The research is divided into (i) multifunctional ceramic tool design (Section 5.2), (ii) multifunctional ceramic tool fabrication (Section 5.3), (iii) drug releasing test (Section 5.4), (iv) bone drilling test (Section 5.5), and (v) implantation test through osteoblast induction assessment (Section 5.6)

Chapter 6 summaries research work (Section 6.1) and discusses research findings and outcomes (Section 6.2), particularly outlining three additively-manufactured tooling solutions benefits for medical field applications.

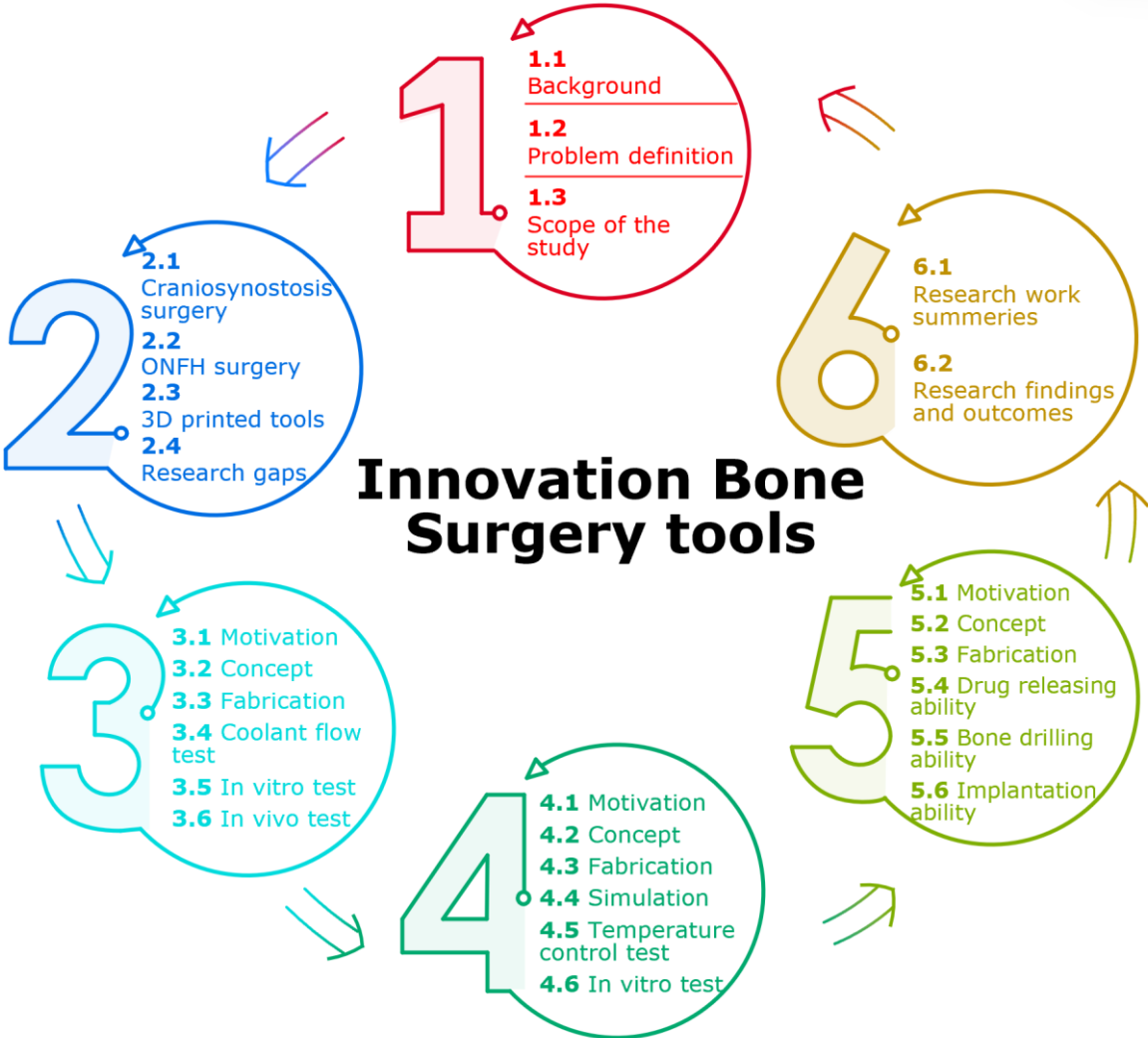


Figure 1-3: Scope of the study.



## **Chapter 2 Literature review & Research gaps**

The literature review is carried out from three aspects regarding (i) cooling strategies in craniostomosis surgery, (ii) operational programs in ONFH surgery, and (iii) additively-manufactured tools. This is because, (i) the bone grinding process in craniostomosis surgery carries the risk of thermal buildup, which can damage the surrounding brain tissue in the surgical area, (ii) ONFH surgery involves complex surgical steps and tens of surgical tools, which may lead to fractures and recurrent bone necrosis, and (iii) the additive manufacturing technology provides new possibilities for tool production.

### **2.1 Cooling strategies in craniostomosis surgery**

Craniostomosis surgery is typically performed during infants' cranial development stage. At this stage, the skull and the surrounding neural tissues are fragile, strictly requiring temperature to be within a safe range during the surgery to prevent irreversible complications, such as blindness and cognitive impairments. Advanced cooling strategies based on coolant supply systems and new tools are crucial for maintaining stable temperatures in the surgical area and improving postoperative outcomes.

#### **2.1.1 Based on external coolant supply systems**

In general, bone grinding procedures with coolant supply systems are more effective in reducing heat accumulation from the surgical area compared to

those without coolant delivery. Numerous studies proposed various forms of coolant supply systems including (i) irrigation, (ii) spraying, and (iii) cryogenic flushing, and explored their effectiveness in dissipating heat from the surgical site.

### **(i) For irrigation:**

Salomó-Coll et al. [16] and Augustin et al. [17] found that external irrigation combined with low grinding speed can effectively keep the bone temperature below 47°C. Gehrke et al. [18] recommended the innovative double irrigation device (internal and external irrigation) to enhance existing cooling systems. This technique demonstrated great efficiency and controlled the bone temperature rise by only  $12.4 \pm 0.75^\circ\text{C}$ , whereas the external irrigation and non-irrigation methods led to the temperature rise by 21.7°C and 14.2°C respectively. However, variations in coolant irrigation volume could still affect bone temperature change [19]. Strbac et al. [20] discovered that the maximum bone temperature increase can be limited to 1.51°C (median) when using the double irrigation cooling system with the saline solution irrigation flow of 50 mL/min. However, the delivery of adequate coolant into the grinding area remains challenging, although irrigation-based coolant supply systems are widely used in actual craniosynostosis surgery.

### **(ii) For spraying:**

Hou et al. [21] compared the effects of saline spray cooling and irrigation cooling in bone grinding experiments. The highest temperature in the bone grinding area was 29.34°C using the saline spray cooling system, while the irrigation cooling system reached 32.45°C under the same rotational speed and cutting depth. Sasaki et al. [22] developed the spraying system that enabled coolant to be delivered onto the grinding area via the high-pressure air jet. The spraying system effectively reduced the temperature not only at the grinding area, but also at the surrounding area (soft tissues around the bone). However, excessive coolant spraying leads to an unclear vision in the surgical area, which may affect the surgeon's operation. Jamil et al. [23] developed the micro-spray cooling system designed to eject the small amount of air-saline mixture under high pressure. This system provided a more lubricated and drier surgical environment compared to traditional irrigation and spray cooling systems. Spray cooling strategies result in large temperature fluctuations and an unstable temperature range, although they can reduce the highest temperature in the bone grinding area to be lower than the bone damage threshold during the surgery.

### **(iii) For cryogenic flushing:**

Barrak et al. [24] chilled a room-temperature coolant to 10°C and then used the coolant to flush the bone grinding area. The cryogenic coolant maintained the average bone temperature variation within 1°C and achieved the maximum temperature increase of 2.1°C during the surgical grinding process. The impact

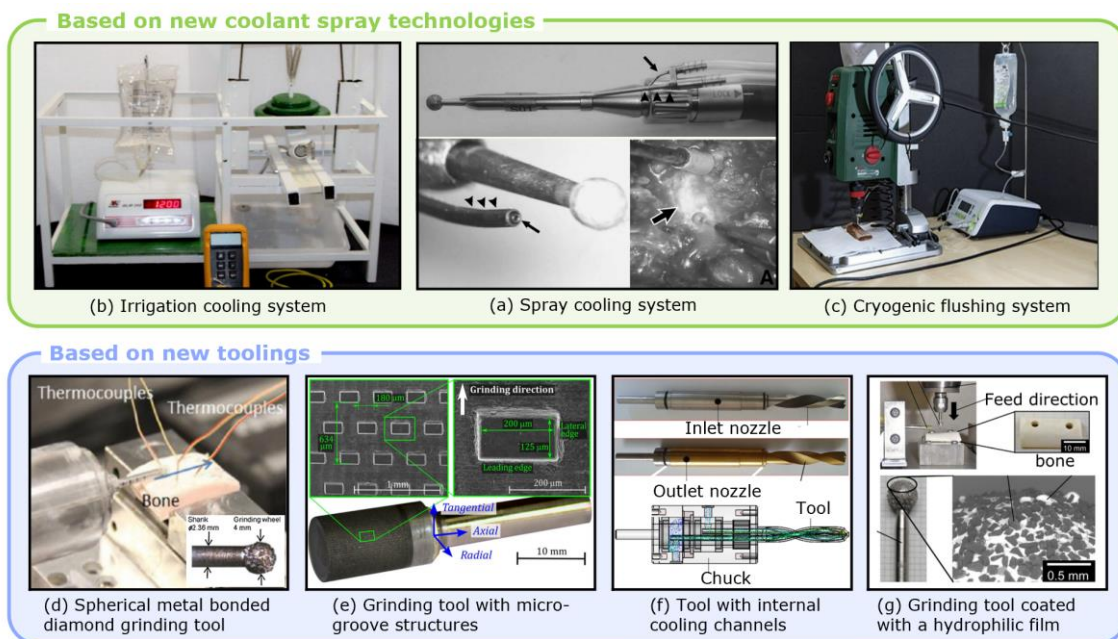
of cryogenic flushing on complications is also explored. Takenaka et al. [25] demonstrated that using cryogenic saline flushing during craniostomy surgery reduced clinical upper limb palsy incidence compared to room-temperature saline. The clinical upper limb palsy incidence was 4.9% for cryogenic saline flushing, while 9.5% for room-temperature one. Similarly, Murphy [26] found that 10°C cryogenic saline was more effective in reducing edema and inflammation compared to 25°C saline.

However, cooling strategies based on different supply systems still have limitations. For instance, an insufficient amount of coolant reaching the bone-tool interface resulted in low heat dissipation efficiency [27]. The cost of coolant supply systems (including nozzles, pumps, and coolants) was high [28]. Therefore, better cooling strategies in craniostomy surgery are still needed.

### **2.1.2 Based on new tools**

Except for coolant supply systems, new tools can reduce bone temperature during surgery. Babbar et al. [29] developed the convex-shaped grinding tool and conducted bone grinding tests. The proposed convex-shaped tool reduced the bone temperature (the highest 46.02°C) more effectively compared to conventional spherical grinding tools in [30]. Similarly, Hou [21] developed the novel diamond bullet grinding tool, which reduced the highest bone temperature to be 38.29°C during bone grinding process. However, these tools increase the risk of postoperative complications (such as infections) due to bone

debris retention in the grinding area. Luna et al. [31] and Zhou et al. [32] proposed that creating micro-grooved structures on diamond grinding tools could not only effectively reduce bone debris retention but also enhance heat dissipation in the grinding area. Augustin et al. [33] and Gok et al. [34] suggested that the integration of cooling channels into grinding tools could directly deliver coolant to the bone-tool interface. The highest bone temperature using such grinding tools with the internal cooling system was 7.8°C lower than that using conventional solid grinding tools. Additionally, Babbar et al. [35] developed the bone grinding tool equipped with the automated control system. This tool not only reduced surgery difficulty but also kept surgical area temperature to be below 43°C. Enomoto et al. [36] introduced the grinding tool coated with the hydrophilic film. The proposed grinding tool with the excellent hydrophilicity allowed the improved contact with coolant, limiting bone temperature increase to be 30°C during one-minute continuous grinding.



(Source: a [18] , b [22], c [37], d [30], e [31], f [34], g [36])

Figure 2-1: Research on cooling strategies in craniostomosis surgery: (a) irrigation cooling system, (b) spray cooling system and (c) cryogenic flushing system are based coolant supply technologies; (d) spherical metal bonded diamond grinding tool, (e) grinding tool with micro-groove structures, (f) tool with internal cooling channels and (g) grinding tool coated with a hydrophilic film based on new tools.

### **2.2 Operational programs in femoral head osteonecrosis surgery**

When ONFH deteriorates and non-surgical procedures (pharmacotherapy and physical therapy) prove ineffective, most patients need a surgical intervention to alleviate pain and maintain mobility [38]. The ONFH surgery involves three main steps: bone drilling, bone implantation, and drug delivery.

#### **2.2.1 Bone drilling step**

Bone drilling is an indispensable step in the surgical treatment of ONFH. Yuan et al. [39] analyzed the impact of different drilling positions (above, parallel, and below) on the mechanical properties of femurs utilizing finite element method. The femoral stiffness was the highest in the above group, while the lowest in the below group. However, large drilling diameters could damage surrounding healthy bone tissues, disrupting inherent mechanical structure of the bone [40]. Mohanty et al. [41] recommended multiple small-diameter drilling procedures instead of a single drilling procedure during ONFH surgery. Omran [42] found that multiple small-diameter drilling procedures were considered safer and less invasive compared with a single drilling procedure. The multiple drilling method had a low risk of fracture and bleeding in the early stage (52.8% of patients had

significant relief of hip pain) [42]. In addition, multiple drilling procedures significantly extended bone collapse time (multiple drilling: 42.3 months; single drilling: 22.6 months) and reduced bone collapse incidence (multiple drilling: 55.0%; single drilling: 85.7%) over a three-year period after surgery [43]. However, due to high rigidity of currently used drilling tools, they are unable to effectively reach the entire area of femoral head, resulting in limited drilling coverage. Alambeigi et al. [44] developed the innovative steerable drill capable of following the planned curved-drilling trajectory, thereby facilitating a multi-branch drilling procedure.

### **2.2.2 Implantation step**

In ONFH surgery, implantation is a critical step in order to repair damaged bone structure and restore function and stability. Bone implantation involves inserting artificial bone or other materials into a patient's skeletal system. The material properties of bone implants are crucial for their successful implantation. The commonly-used implant materials included (i) metals and (ii) ceramics.

#### **(i) Metals**

Metals are widely used materials in bone implantation procedures due to their excellent mechanical properties and corrosion resistance. 316 stainless steel is one of the earliest metallic materials used for bone repair in ONFH surgery. However, elastic modulus of stainless steel was significantly different from that

of natural bone, which led to potential stress shielding and bone load imbalance [45, 46]. The introduction of titanium alloys with low elastic modulus not only enhances bone implants performance but also improves the interaction with the surrounding bone tissue. Wang et al [47] and Wang et al [48] fabricated porous titanium alloy rods for early-stage ONFH treatment. The CT and histological images showed that the new bone had grown along the metal trabeculae toward rod center with satisfactory implant-bone integration in 3 months.

In recent years, porous magnesium alloy scaffolds showed promising prospects in biomedical applications due to their degradation characteristics [49, 50]. Zhang et al. [51] demonstrated that the magnesium alloy scaffold had completely degraded in 24 weeks after implantation through in vivo experiments. Compared to other metallic materials, porous tantalum rods exhibit superior biological stabilities, promoting bone healing. Numerous studies demonstrated that porous tantalum rods for ONFH treatments achieved favorable clinical outcomes and a high survival rate (74.1% at 62 months) [52-55]. Some researchers suggested combining tantalum with other materials to reduce high implant cost [56, 57]. Tantalum coatings were successfully applied on stainless steel and titanium alloy surfaces through surface modification techniques (electroplating, carbonised, etc.) [58, 59]. The incorporation of tantalum improved the corrosion resistance and antibacterial properties of

stainless steel and titanium alloys, thereby enhancing the long-term stability of implants [60].

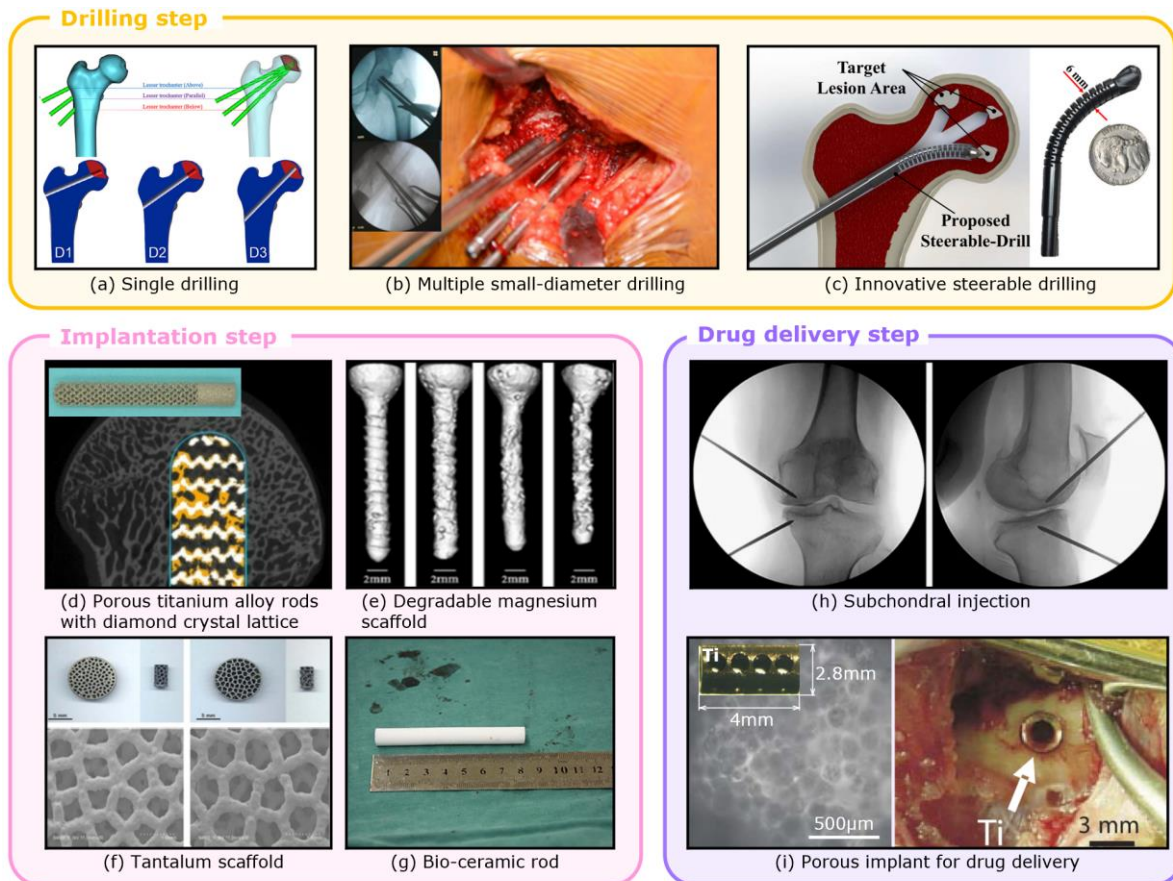
### **(ii) Ceramics**

Ceramic materials have excellent biocompatibility, bioactivity, and mechanical properties. They become an alternative to metal implants in ONFH surgery, due to the high metallic cost. Extensive clinical data indicated that bioceramic rods formed a good combination with bone tissues after surgery and demonstrated the high success rate of 70-90% in clinical cases of ONFH [61, 62]. However, ceramic implants are prone to fracture and fragment during implantation procedures due to their high brittleness. Shtansky et al. [63] and Donkov et al. [64] deposited ceramic coatings on the surface of metal-based implants to improve the mechanical properties of pure ceramic implants. After the heat treatment at 500°C, the ceramic coating exhibited high adhesive strength (1907 mN), and the coated implants demonstrated significant surface hardness (535.5 HV) [65].

### **2.2.3 Medication delivery step**

Drug delivery aims to promote bone repair and alleviate inflammation in ONFH surgery. Neustadt [66] suggested the direct intra-articular injection of corticosteroids or hyaluronan, which significantly relieved knee pain in 61% of patients. Kon et al. [67] found that subchondral injection of bone marrow concentrates effectively improved bone marrow edema. However, traditional

injection techniques fail to achieve comprehensive drug coverage in bone necrosis sites. Several studies indicated that porous implants could serve as carriers for drug delivery [68]. The porous structures not only provided a large surface area for cell attachment but also facilitated sustained therapeutic effects and comprehensive drug penetration in the bone necrosis area [68].



(Source: a [39], b [41], c [44], d [47], e [50], f [52], g [62], h [67], i [68])

Figure 2-2: Research on Osteonecrosis of Femoral Head surgery steps: (a) single drilling, (b) multiple small-diameter drilling and (c) Innovative steerable drilling are drilling surgery step; (d) porous titanium alloy rods with diamond crystal lattice, (e) degradable magnesium scaffold, (f) porous tantalum scaffold and (g) bio-ceramic rod are implantation step; (h) subchondral injection and (i) porous titanium implant for drug delivery are drug delivery step.

### 2.3 Additively-manufactured tools

In tool design and fabrication, additive manufacturing brings various benefits, including flexible design, cost savings, and customized production. Additive manufacturing is widely used to produce (i) grinding tools and (ii) cutting tools.

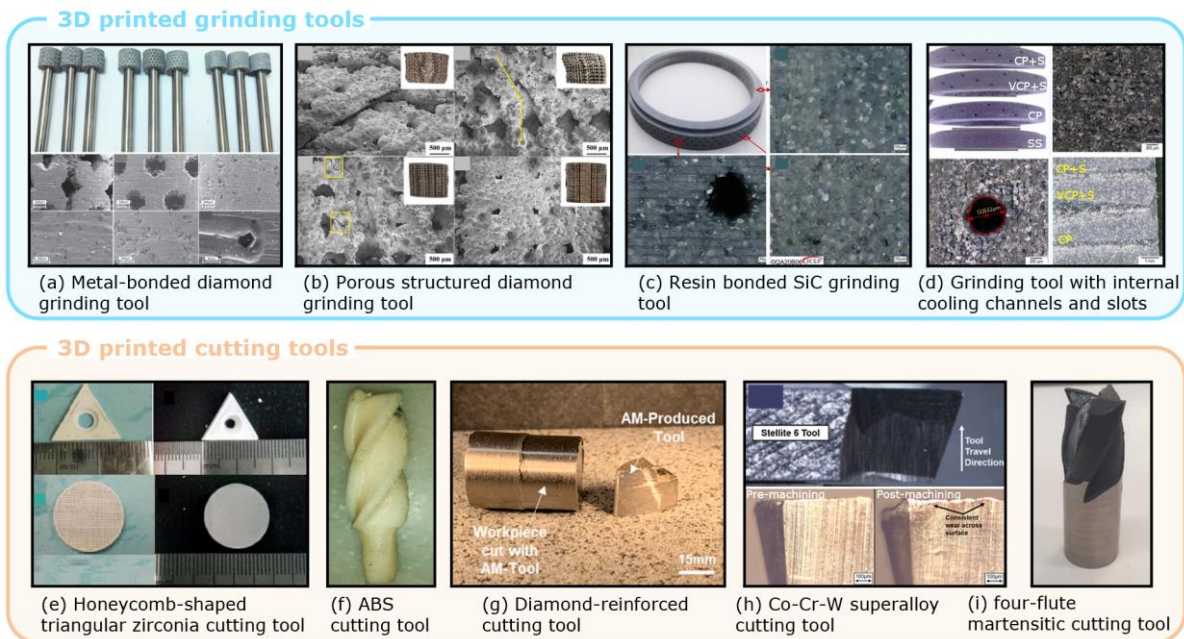
### **(i) Grinding tools**

Tian et al. [69] developed three types of metal-bonded diamond grinding tools with different structures (solid, honeycomb and octahedral structure) using Selective Laser Melting (SLM) techniques. These tools exhibited excellent dressing and self-sharpening capabilities in grinding experiments. However, the abrasive layer of metal-bonded grinding tools has a limited porosity. To address this, Peng et al. [70] developed the porous diamond grinding tool with high porosity (53%) via SLM. Tian et al. [71] fabricated grinding tools based on triply periodic minimal surfaces utilizing SLM and optimized the tool porosity to 60%. Denkena et al. [72] produced the Ni-Ti bond diamond grinding tool utilizing Laser Powder Bed Fusion (LPBF) technology. The deepest scratch of the Ni-Ti bond diamond grinding tool was only 8.27  $\mu\text{m}$ , which verified the high mechanical properties in the scratch test. However, LPBF may affect the integrity and durability of grinding tools due to impure powder and high inter-particle gaps. Digital Light Processing (DLP) is introduced for grinding tool manufacturing due to its high precision and surface quality. Most studies focused on mixing abrasive grains with resin to fabricate grinding tools via DLP, including resin bonded diamond grinding tools [70, 73, 74] and resin bonded SiC grinding tools [75]. The resin bonded diamond grinding tools achieved the

bending strength of 80 MPa [73]. Additionally, Barmouz et al. [76] manufactured grinding tools with internal cooling channels and slots, demonstrating the design flexibility and customization capabilities of additive manufacturing.

### **(ii) Cutting tools**

He et al. [77] successfully manufactured the honeycomb-shaped triangular zirconia cutting tool with high hardness (13.0597 GPa) via SLA. Sandhu et al. [78] manufactured the acrylonitrile-butadiene-styrene (ABS) cutting tool utilizing Fused Deposition Modeling (FDM). FDM controlled the tool dimension and surface smoothness error within 2 mm [78]. Traxel et al. [79] developed the diamond-reinforced cutting tool utilizing Directed Energy Deposition (DED). The tool exhibited high anti-adhesion properties, which produced 35% less chip accumulation than conventional cutting tools. Similarly, Traxel et al. [80] fabricated the Co-Cr-W superalloy cutting tool via DED with the total tool wear less than 150  $\mu\text{m}$ . The four-flute martensitic cutting tool fabricated by Direct Metal Laser Melting (DMLM) exhibited higher wear resistance (total wear less than 119.5  $\mu\text{m}$ ), compared to tools manufactured by DED [81]. Additionally, LPBF was used to manufacture metal cutting tools with complex structures, such as WC-Co tools with porosity [82] and multi-tooth cutting tools with internal cooling channels [83].



(Source: a [69], b [70], c [75], d [76], e [77], f [78], g [79], h [80], i [81])

Figure 2-3: Additively-manufactured tools: (a) metal-bonded diamond grinding tool; (b) porous structured diamond grinding tools; (c) resin bonded SiC grinding tool; (d) grinding tool with internal cooling channels and slots; (e) honeycomb-shaped triangular zirconia cutting tool, (f) ABS cutting tool; (g) diamond-reinforced cutting tool; (h) Co-Cr-W superalloy cutting tool and (i) four-flute martensitic cutting tool.

## 2.4 Summary of research gaps

### (i) Lack of effective cooling and temperature control for craniostyosis surgery

Cooling strategies based on either external cooling systems or new tools still face substantial challenges. **For external coolant supply systems:** Insufficient amounts of coolant reaching the tool-bone interface leads to low heat dissipation efficiency and unstable bone temperatures. The high cost of coolant supply devices (such as nozzles, pumps, and coolants) limits the widespread application of external cooling strategies. **For new tools:** The new tool with

hydrophilic coatings exhibits low cooling performance and efficiency due to inadequate bone chip evacuation capabilities. Moreover, most studies focus on enhancing cooling strategies. There is a lack of research on temperature monitoring and precise temperature control in the surgical area.

### **(ii) Lack of multifunctional tools and an early intervention strategy for ONFH surgery**

Currently, most research aims to improve specific surgical steps (such as bone drilling, implantation, and drug delivery) that were typically performed in the mid to late stages of ONFH. However, few studies integrate the tools involved in surgery into a multifunctional tool to simplify numerous surgical steps. Additionally, an early intervention strategy for ONFH is essential, which is also absent in literature.

### **(iii) Lack of additively-manufactured tools in orthopedic surgery.**

Additive manufacturing technologies are predominantly utilized in mechanical component production, such as grinding and cutting tools. Additive manufacturing in the medical field can enable the customization of surgical tools, thereby enhancing the treatment outcomes. However, this application remains relatively underdeveloped.

## Chapter 3 Hollow grinding tool

### 3.1 Introduction and motivation

Grinding is a widely used technique in craniostylosis surgery for either bone removing or reshaping [12]. However, traditional high-speed rotating grinding tools generate unacceptably excessive heat between the tool-bone interface. Excessive heat leads to localized thermal osteonecrosis, surrounding tissue damage, and further severe consequences (such as vision loss [14, 15] and nerve damage [13]). Controlling heat is therefore especially crucial [84]. The aims and objectives in this chapter is looking for an effective and cost-efficient strategy to compress surgery heat.

In this chapter, we propose the redesigned hollow grinding tool that facilitates much more coolant flow onto the tool-bone interface, thereby accelerating heat dissipation and controlling local temperature increase. In this chapter, the zirconia grinding tool with the 3D Voronoi geometry is designed (Section 3.2, Figure 3-2b) and successfully fabricated by using Nano Particle Jetting (NPJ) technology (Section 3.3, Figure 3-3 b-g). The coolant flow penetration performance is proved in Section 3.4 (Figure 3-8). The grinding ability is tested both in vitro (Section 3.5, Figure 3-10) and in vivo (Section 3.6, Figure 3-11), demonstrating promising performances. This design not only preserves tissue viability at and around the grinding site but also minimizes the risk of infection and hyperostosis caused by debris residue.

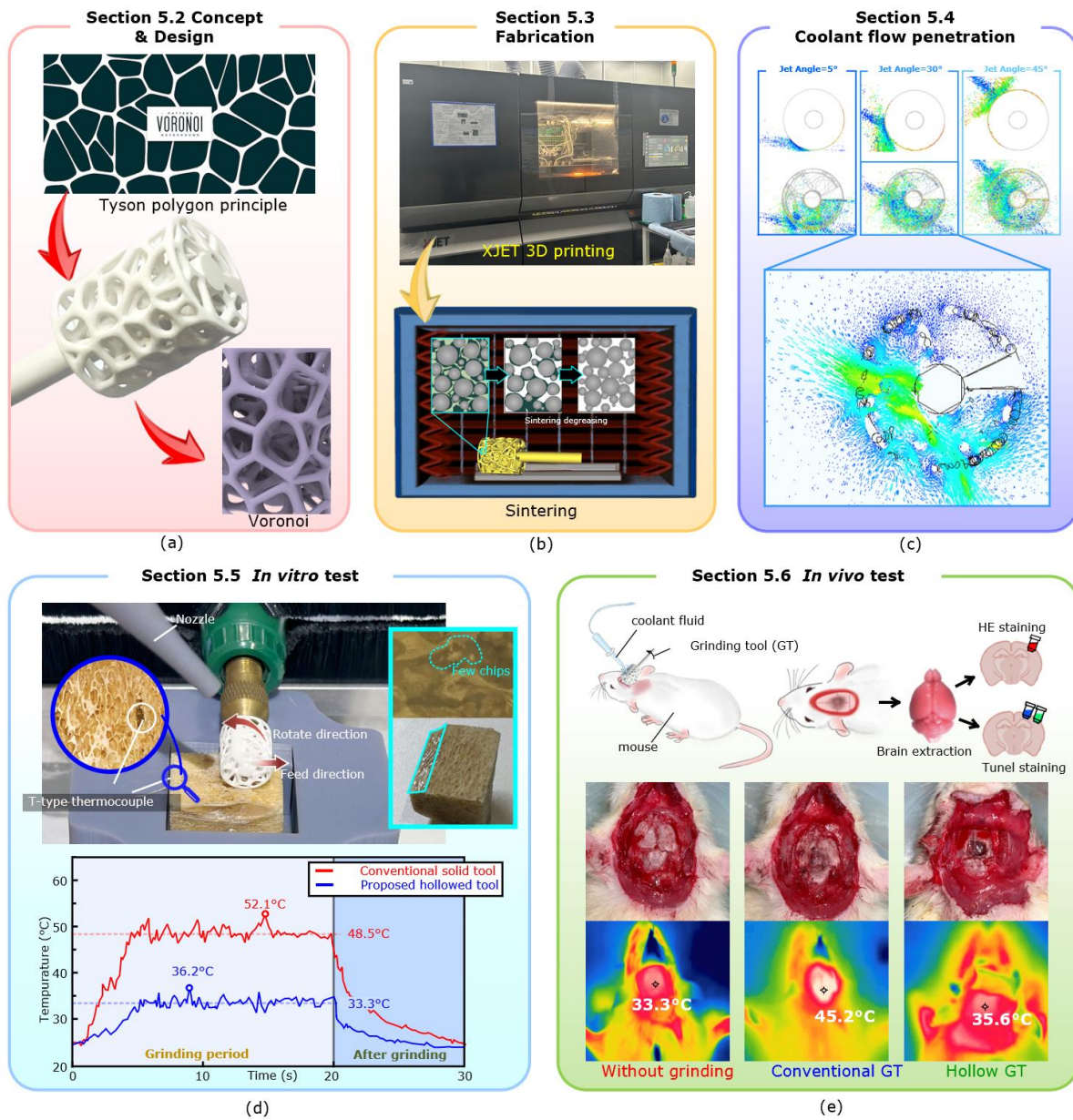


Figure 3-1: the methodology that we followed to design, fabricate and verify our proposed hollow grinding tool: (a) design grinding tool with 3D Voronoi principle, (b) fabrication of designed grinding tool (c) testing & simulation for the coolant flow penetration, and verification of the grinding tool performance (d) in vitro and (e) in vivo.

### 3.2 The hollow grinding tool concept and structural design

#### 3.2.1 Concept

Unlike conventional solid grinding tools that bounce back the majority of coolant in the surgery and therefore have low cooling efficiency (Figure 3-2a), the hollow structure permits coolant to penetrate through the tool and flush the tool-bone interface (Figure 3-2b), thereby reducing heat accumulation and aiding in the removal of bone debris generated during surgery.

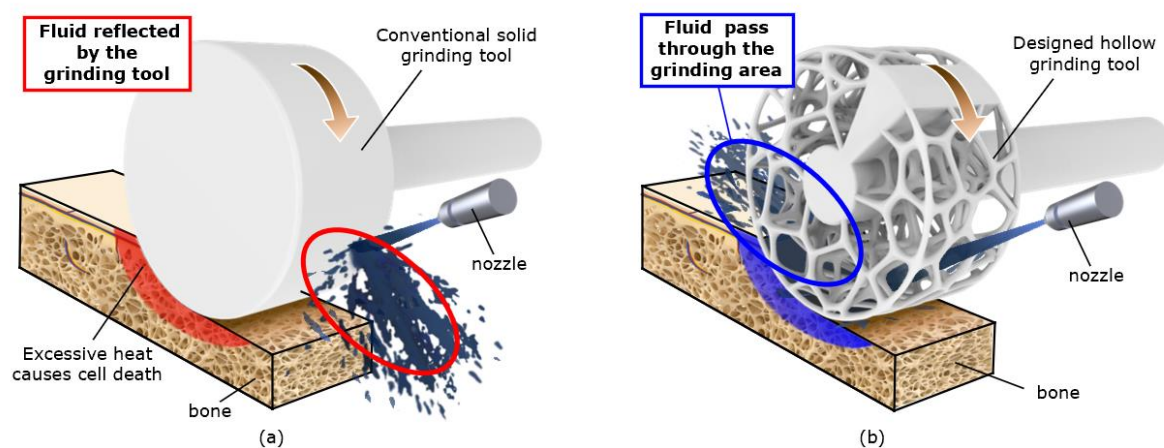


Figure 3-2: Conceptual diagram of (a) conventional solid grinding tool and (b) the proposed hollow grinding tool.

### 3.2.2 Structural design

The basic structure of the proposed grinding tool is designed using 3D Voronoi, which is known for achieving a favorable balance between high structural strength [85] (to serve as a surgical tool) and adequate porosity (to allow coolant to permeate). The geometry of the grinding tool includes a head with the diameter of 10 mm, the length of 12 mm, and the rod with the diameter of 3 mm. More detailed parameters of the proposed hollow grinding tool are presented in table 3-1. The model of the hollow grinding tool is created using

Rhino software and the Grasshopper plug-in (version 7.20.22193) and is then exported as the STL file.

**Table 3-1**

*The specific parameters of the designed hollow grinding tool*

Grinding Tool size			Grid Unit factor			
Grinding head diameter [mm]	Grinding head length [mm]	Rod diameter [mm]	NodeSize	Endoffset	StrutSize	Segment
10	12	3	0.13	2.80	0.93	0.77

The developed grinding tool features two distinct grinding regions: (i) the scaffold region (illustrated in Figure 3-3, blue area) and (ii) the solid region (shown in Figure 3-3, yellow area). The majority of the grinding tool consists of a reticular scaffold structure, which allows coolant fluid pass through the tool body and reach the grinding zone (see Figure 3-3, light blue line), effectively dissipating grinding-induced heat. Although more debris (small chips) might be generated during grinding, the effective penetration of the coolant fluid facilities the continuous flushing on these chips, ensuring that performance is not adversely affected.

To further improve grinding efficiency, we incorporate a circular solid sector into the design. This solid region is specifically intended to enhance material removal ability during surgical procedures. While the reticular scaffold

predominantly serves to assist in the grinding task, contributing to micro-material removal and the enhancement of surface flatness.

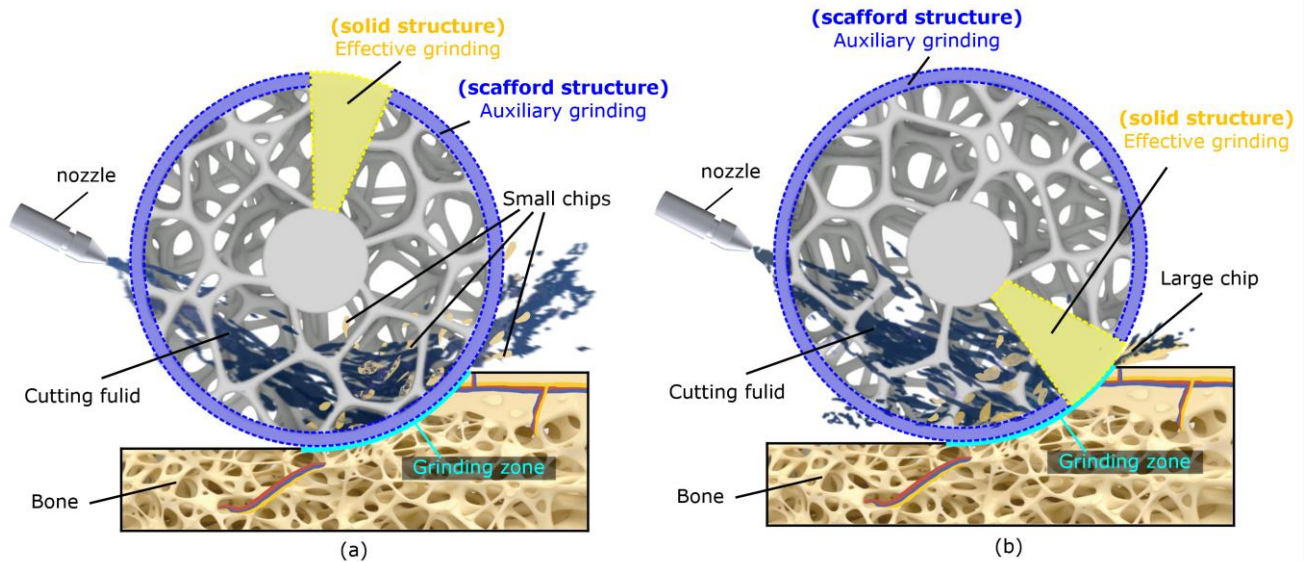


Figure 3-3: A schematic of the proposed hollow grinding tool having: (a) scaffold structure aiming for coolant penetration (auxiliary grinding) and (b) solid structure aiming for effective material removal (effective grinding).

### 3.3 The Fabrication and the geometrical/mechanical evaluation

#### 3.3.1 Fabrication route

The STL model was sliced for fabrication (see Figure 3-4 b and c). The NPJ 3D Printer (XJET, Carmel 1400C, Israel, shown in Figure 3-1b and Figure 3-4e) was used for printing all the grinding tools. This system allowed the super-thin layer thickness of 10.5  $\mu\text{m}$  and the jetting resolution of 1200 DPI (20  $\mu\text{m}$ ). Nanoparticle based structural and support inks were co-printed to form 3D structures and both inks were provided by XJET. The inks were printed onto a heated substrate (180°C) and then scanned by using a halogen bulbs-based

heating lamp to facilitate the volatilization of organic solvents in inks. The schematic of the printing process was revealed in Figure 3-4 d-g. In order to compensate the shrinkage that happened during the sintering, the shrinkage factor of 17.8% was applied on the designed structure [86]. After printing, the printed structure was then removed from the printing stage. The co-printed water-soluble support was removed, and the part was then sintered in a programmable sintering furnace (FMJ-19/17, FaceRom, China). After reaching the sintering temperature of 1450°C, it was held for 180 mins and then cooled to room temperature. The hollow and solid grinding tools were 3D printed by using zirconia ceramic (ZrO<sub>2</sub>), whose wear resistance is 15 times better than that of alumina ceramics, at the meantime the friction coefficient is only half of alumina ceramics.

**Table 3-2**

The specific material ink

---

commercial ZrO <sub>2</sub> ink (C800 zirconia model dispersion grade 7250001, XJET)			support ink (SC300, XJET)		
45wt% ZrO <sub>2</sub> powder	glycol ethers	dispersing agent	31wt% Na <sub>2</sub> CO <sub>3</sub>	glycol ether	dispersing agent

---

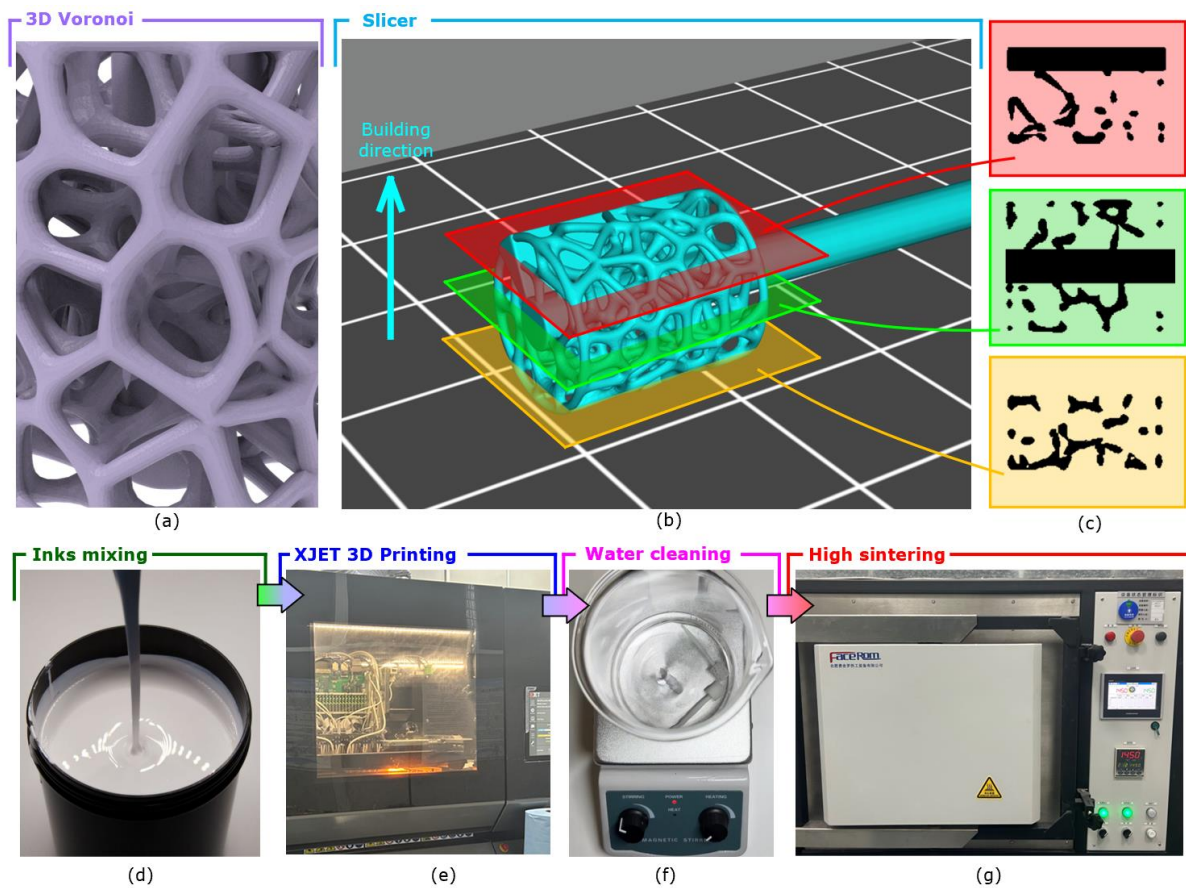


Figure 3-4: Design and Fabrication flow diagram: (a) 3D Voronoi design theory; (b) slicing process and (c) slice shape of each layer; (d-g) specific process for grinding tool fabrication.

### 3.3.2 Geometrical and mechanical evaluation

The printed tool edge surfaces showed stepped or streamlined microstructures (Figure 3-5 b and c), which enhanced material removal ability and grinding efficiency in surgery. Particle agglomeration was rarely observed after the sintering process suggesting completed sintering, although the structures were printed with ceramic nano-particle ink. The printed structure showed good geometrical consistency with our design as well, although shrinkage happened during sintering.

The circular runout was a crucial index for a rotating tool [87], and the roundness of the printed tool was tested as shown in Figure 3-5d. The circumferential runout ranged from +12  $\mu\text{m}$  to -9  $\mu\text{m}$ , only accounting for 0.21% in comparison with the tool head diameter. Except for static tool geometry accuracy, dynamic imbalance was also evaluated by observing the beating range of the dial indicator pointer, especially considering the solid portion might result in structure asymmetry (Figure 3-5e). Based on our experiments, the swing range of the grinding tool during rotation was 2.1  $\mu\text{m}$ . This narrow range could be negligible when considering external factors, such as hand and motor vibration in real surgery [88, 89]. As an important indicator, the mechanical performance of the printed tool was also encouraging, where the hollowed grinding tool had the ultimate strength of 654 MPa which was separately 3 times higher than that of the cortical bone (the hardest bone tissue) [90], and 31 times higher than that of the trabecular bone [91] (see Figure 3-5g).

With the continuous grinding operation, the proposed tool strength might be reduced. To investigate the fatigue performance, we performed three runs of long-period grinding experiments with separately 1, 5 and 10 mins on the bone tissue. Please note the normal period for one trial of continuous grinding operation could be no more than 1 mins [35, 92]. Based on SEM images, the tool did not have obvious broken and fractured failure. Based on the tensile test, the tools after a long period of grinding process had the same trend and the similar ultimate strength as that of the tool without grinding (see Figure 3-5h).

In comparison with an unused tool, the tool strength was only reduced by 5% even for the 10-minute trial, and the reduced tool strength was still larger than bone strength.

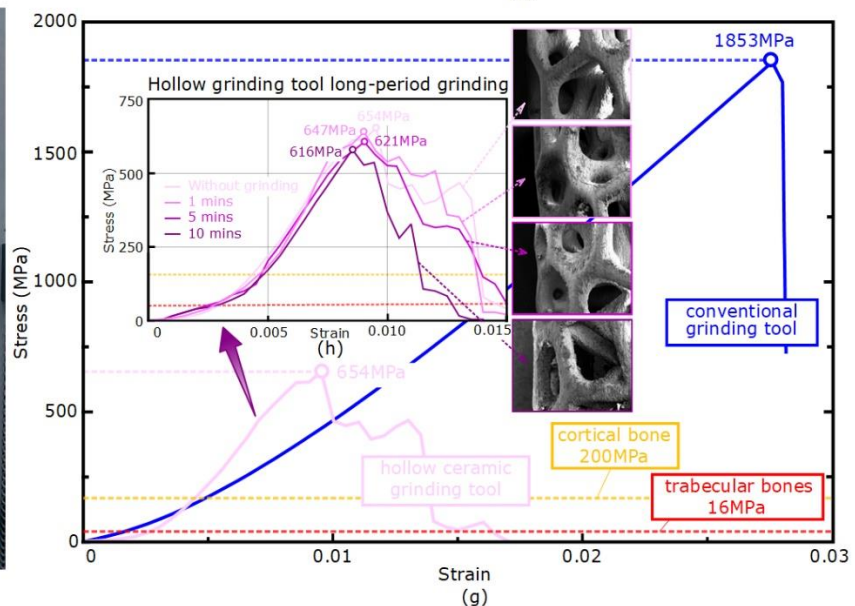
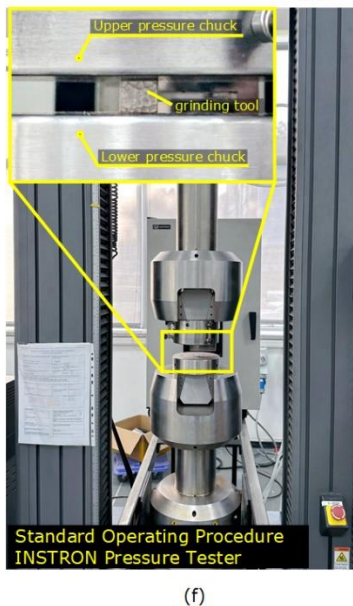
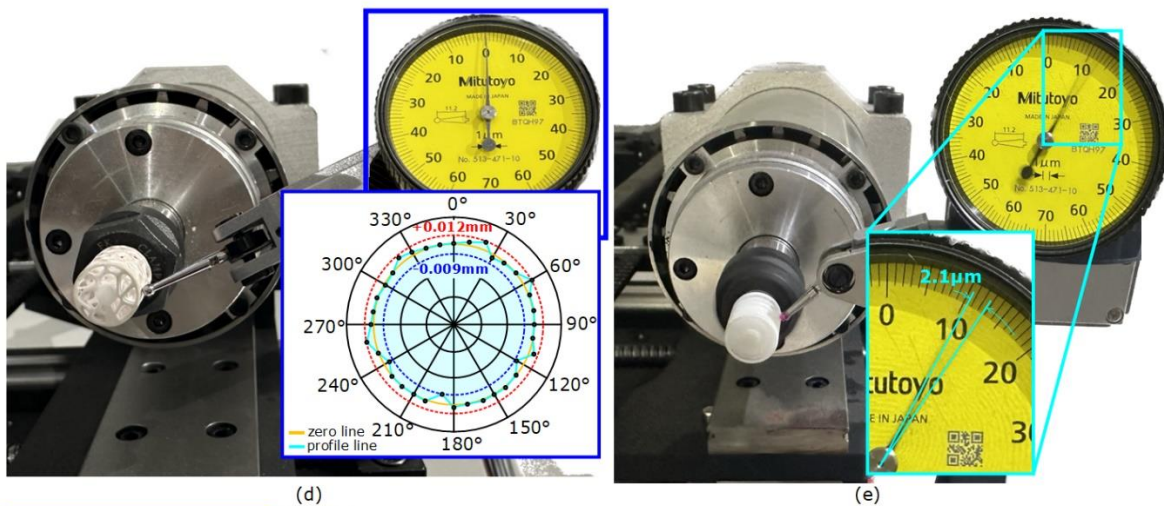
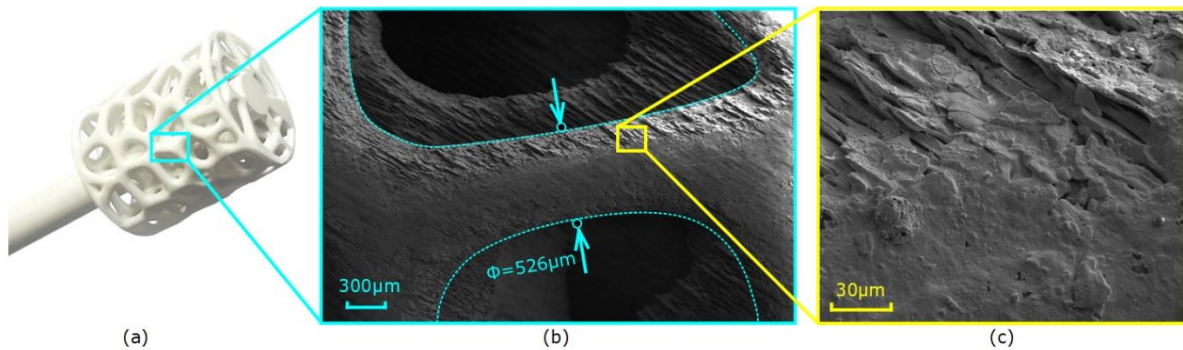


Figure 3-5: Evaluation of the printed hollow grinding tools: (a) sample picture and (b-c) SEM morphological images of 3D printed hollow grinding tools; (d) roundness test device and (e) dynamic balancing results; (f) tensile test and (g) obtained stress-strain curve between hollow and conventional grinding tool and (h) stress-strain curve after long-period grinding.

### 3.4 The coolant flow penetration

#### 3.4.1 CFD simulation

To verify the enhanced coolant permeability of our design, the Computational Fluid Dynamics (CFD) simulation is performed to model the coolant trajectory during the grinding process.

##### (i) Method

The CFD analysis is used to simulate, analyze, and predict the airflow behaviors and coolant distribution within the air-coolant two-phase system. The 3D transient interactions between the spray droplets and the surrounding air are modeled using the Euler/Lagrange approach. Given the specific application requirements for droplet size and concentration, the Discrete Phase Model (DPM), the most widely used turbulence model in engineering applications is selected [93, 94]. The nozzle produces droplets with an average size of 50  $\mu\text{m}$  [95], enabling detailed process capture. The timestep is set to 1e-5s to maintain a Courant number below 1, and the rotation speed is set to 523 rad/s, consistent with the experimental condition of 6000 rpm. The CFD simulation was conducted using ANSYS Fluent 2021R.

The simulation process followed the standard CFD algorithm, with important aspects such as: (i) simplifying droplet computations by grouping them together, (ii) determining coefficients for shape variation and analyzing dynamic interactions between phases, and (iii) carefully selecting and configuring the necessary parameters.

For (i), modeling each droplet individually is computationally infeasible, so this study employs simplifications. The DPM model groups droplets with similar characteristics into parcels. The model allows the simulation to represent a spray with fewer than a million parcels instead of billions of droplets, which greatly reduces computational demands. In this model, discrete phase particles are introduced into the airflow field, and their transport is computed by balancing forces on each particle within the Lagrangian framework.

In part (ii), the Dynamic Drag Model is utilized to dynamically compute the coefficient associated with the shape alterations of the droplets. Among the various forces at play, only the turbulent dispersion force is considered significant, while the added mass and lift forces are deemed to have negligible effects. To incorporate the effects of turbulent dispersion, the Standard Discrete Random Walk Model is used, and the Wave Breakup Model is integrated to represent the dynamic interactions between the phases effectively.

In section (iii), the SIMPLEC scheme is used for coupling pressure and velocity. A summary of the detailed equations can be found in Table 3-1. The time step between simulation frames (the conventional solid grinding tool and the proposed hollow grinding tool) is set to 1e-5 seconds to maintain a Courant number below 1. The rotating speed is established at 523 rad/s, which corresponds to an experimental condition of 6000 rpm. A pressure outlet with  $P_{rel}=0$  is designated at the nozzle exit. The computational domain features non-slip wall conditions, and the wall-film boundary conditions are defined for DPM scenarios. For the droplet particles, water with a density of  $\rho=998.2 \text{ kg/m}^3$  is utilized in the discrete phase, while the volume flow rate is maintained at 10 L/min, aligning with the experimental setup.

**Table 3-2**

Equations in the Euler/Lagrange approach

---

Euler/Lagrange Model

---

$$\frac{\partial \rho}{\partial t} + \nabla \cdot (\rho \mathbf{u}) = 0$$

$$\frac{\partial}{\partial t} (\rho \mathbf{u}) + \nabla \cdot (\rho \mathbf{u} \mathbf{u}) = -\nabla P + \nabla \cdot (\boldsymbol{\tau}) + \rho \mathbf{g}$$

Standard k- $\epsilon$  turbulence model

$$\frac{\partial}{\partial t} (\rho k) + \nabla \cdot (\rho \mathbf{u} k) = \nabla \cdot \left( \left( \mu + \frac{\mu_t}{\sigma_k} \right) \nabla k \right) + G_k - \rho \epsilon$$

$$\frac{\partial}{\partial t}(\rho \varepsilon) + \nabla \cdot (\rho \mathbf{u} \varepsilon) = \nabla \cdot \left( \left( \mu + \frac{\mu_t}{\sigma_\varepsilon} \right) \nabla \varepsilon \right) + C_{1\varepsilon} \frac{G_k \varepsilon}{k} - C_{2\varepsilon} \rho \frac{\varepsilon^2}{k}$$

$$\mu_t = \rho C_\mu \frac{k^2}{\varepsilon}, C_{1\varepsilon} = 1.44, C_{2\varepsilon} = 1.92, C_\mu = 0.09, \sigma_k = 1 \text{ and } \sigma_\varepsilon = 1.3$$

DPM Model

$$\frac{d\mathbf{u}_p}{dt} = F_D(\mathbf{u} - \mathbf{u}_p) + \frac{\mathbf{g}(\rho_p - \rho)}{\rho_p} + \mathbf{F}$$

Dynamic Drag Model

$$F_D = \frac{18\mu}{C_c \rho_p d_p^2} \frac{C_D \text{Re}}{24}$$

$$C_{D,\text{dynamic}} = (1 + 1.2632y)C_{D,\text{sphere}},$$

$$C_{D,\text{sphere}} \begin{cases} 0.424, \text{Re} > 1000 \\ \frac{24}{\text{Re}} \left( 1 + \frac{1}{6} \text{Re}^{\frac{2}{3}} \right), \text{Re} \leq 1000' \end{cases}$$

## (ii) Results and discussions

The comparison of coolant velocity vectors from the front view revealed several interesting and unique phenomena:

(i) In our design (Figure 3-6a), most of the coolant successfully passed through the grinding tool body, with 48% of the coolant reaching the grinding zone. In contrast, for the conventional solid grinding tool (Figure 3-6b), most of the coolant bounced back, suggesting that our proposed tool had significant potential to reduce surgery temperature.

(ii) The conventional solid grinding tool generated more fluid spatter compared to the proposed hollow grinding tool, as indicated by the arrows showing moderate velocity in Figure 3-6a and 3-6b. This suggested that the hollow grinding tool offered surgeons a clearer view during surgery than the conventional solid tool.

(iii) The flow rate of the coolant increased significantly after entering the hollow grinding tool, which might be attributed to the interaction between the coolant and the small pillars inside the hollow grinding tool.

(iv) Upon exiting the hollow grinding tool, the coolant velocity was reduced by only 35% compared to its velocity at the inlet (Figure 3-6c). This indicated that the proposed hollow tool provided better heat control and more effective bone debris removal.

To evaluate coolant permeability at different jet angles, simulations were conducted for three angles: 5°, 30°, and 45° (see Figure 3-6d). For comparison, models of solid grinding tool with identical outer parameters were also created. As shown in Figure 3-6d, the coolant in the hollow tool consistently reached the grinding zone regardless of the jetting angle. In contrast, the conventional solid tool only demonstrated limited fluid permeability at the 5° jetting angle. These simulations confirm that the porous mesh-optimized hollow grinding tool offers superior coolant permeability compared to the conventional solid tool. Additionally, it provides great operational flexibility for surgeons, enabling the

use of a wide range of jetting angles. This flexibility is particularly valuable in situations where surgeons need to access challenging locations or directions.

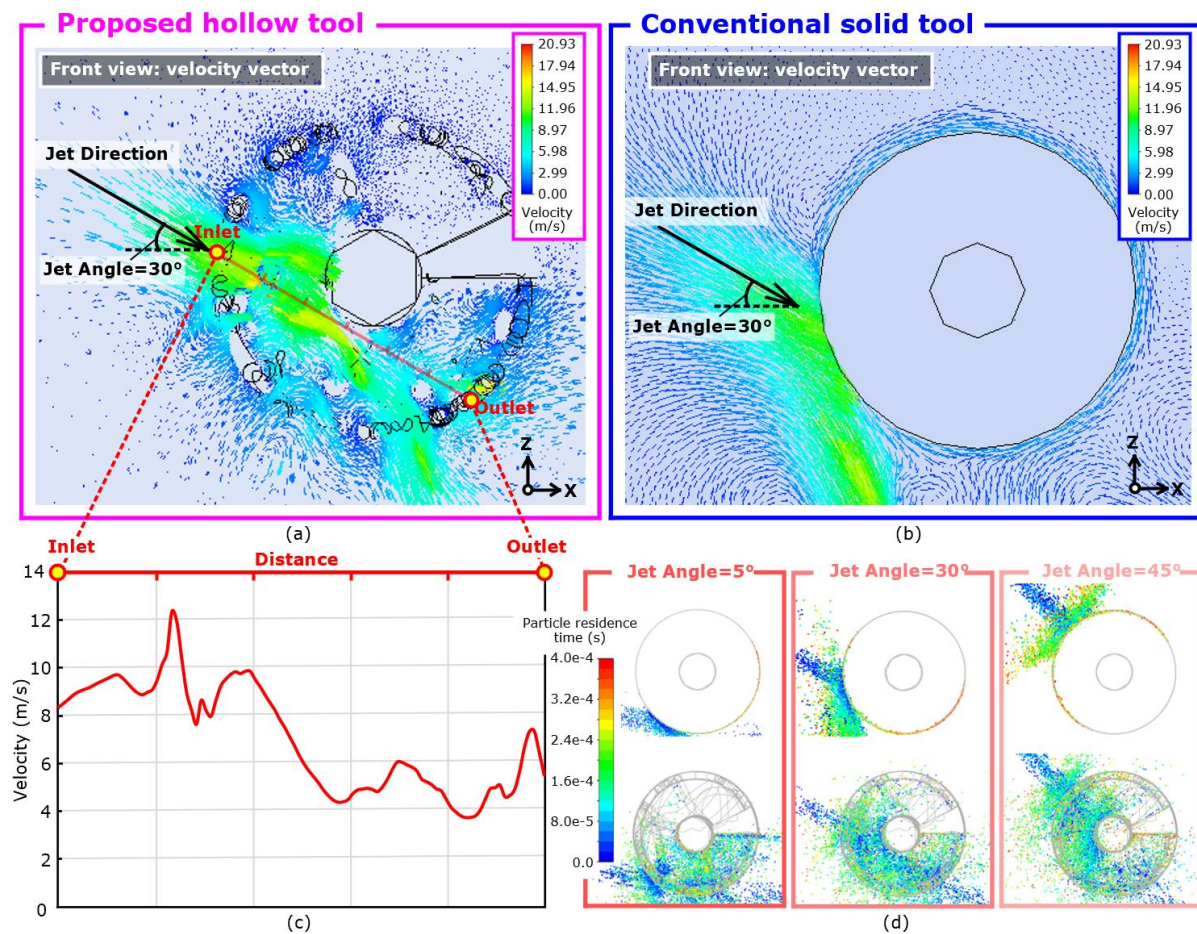


Figure 3-6: Simulated result of the coolant behaviours: (a) the velocity vector of the proposed hollow grinding tool and (b) conventional solid grinding tool from the front view; (c) the average fluid velocity along the path from inlet to outlet along the jet direction by using proposed tool; (d) permeability of the coolant at different jet angles (5°, 30°, 45°).

### 3.4.2 Experimental investigations

#### (i) Experiment setup

To determine whether our proposed hollow tool exhibits superior coolant permeability compared to conventional solid tools, the coolant flow penetration validation experiment is conducted. The experimental setup, as

illustrated in Figure 3-7, closely resembles a standard mechanical grinding system, incorporating XYZ motion elements, a spindle, a tool, coolant supply, and a protection system. The specialized testing stage is designed with a 2 mm hole on the top surface, connected to a chamber within the stage. A pH paper (San S) is placed inside the chamber directly beneath the exit of the 2 mm hole (Figure 3-7b). To prevent coolant from entering the hole from the sides, no clearance is allowed between the tool and the hole entrance. The designed hole is small in diameter to set a strict requirement when evaluating coolant permeability for tools. Based on this test platform, the pH color will not be changed if the grinding tool has poor ability to transport coolant to reach the tool-hole interface. Conversely, for our proposed tool, the coolant is expected to penetrate the grinding interface, enter the hole, wet the pH paper, and trigger color change.

As the experiment aims to observe coolant behavior without any physical contact, the grinding tools are 3D printed using transparent resin materials, providing a clear view of the flow behaviors and trajectories. The coolant (soda water mixed with red paint for better visualization) is directed towards the rotating tool. The grinding tool is operated at 6,000 rpm, and the coolant (a mixture of water, baking soda, and red paint in a 100:4:1 ratio) is ejected from the nozzle at a flow rate of 10 L/min.

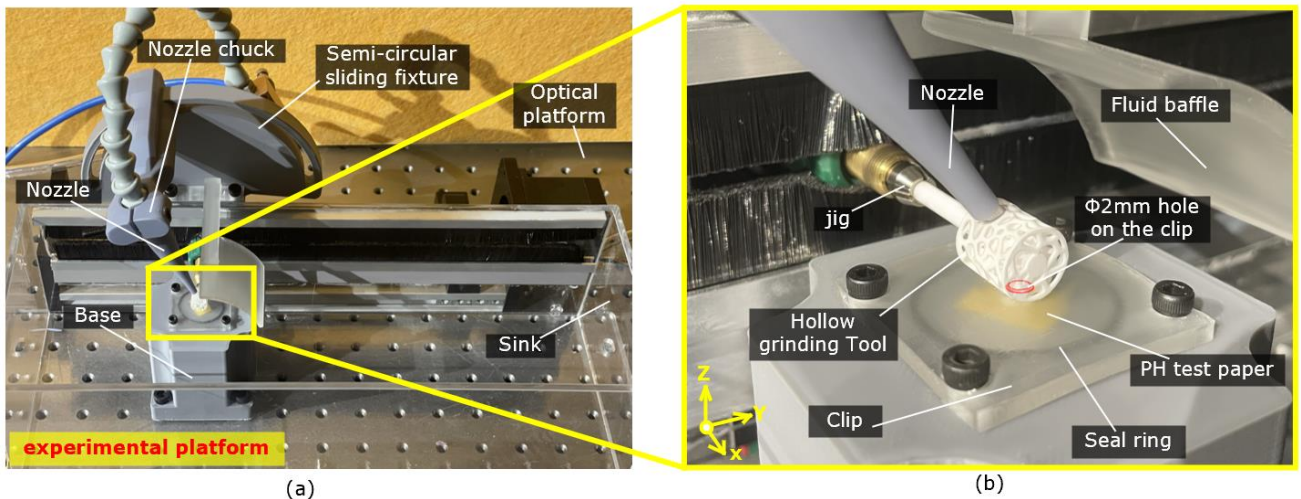


Figure 3-7: (a) Global and (b) detailed images of the experiment setup for coolant fluid permeability.

### (ii) Results and discussion

Figure 3-8a presents the evaluation results of the coolant flow penetration experiment. For the conventional tool, the color of the pH paper remained unchanged even after 20 seconds, indicating that no coolant reached the grinding zone (see Figure 3-8d). This observation was consistent with previous findings from CFD simulations. In contrast, for the proposed tool, the pH paper was immediately saturated with coolant and turned dark green when the coolant was sprayed toward the rotating tool (Figure 3-8c). This result clearly demonstrates that a significant volume of coolant reaches the hole entrance with sufficient speed and dynamic energy. These findings strongly support the conclusion that the hollow grinding tool exhibits significantly better permeability compared to the solid tool.

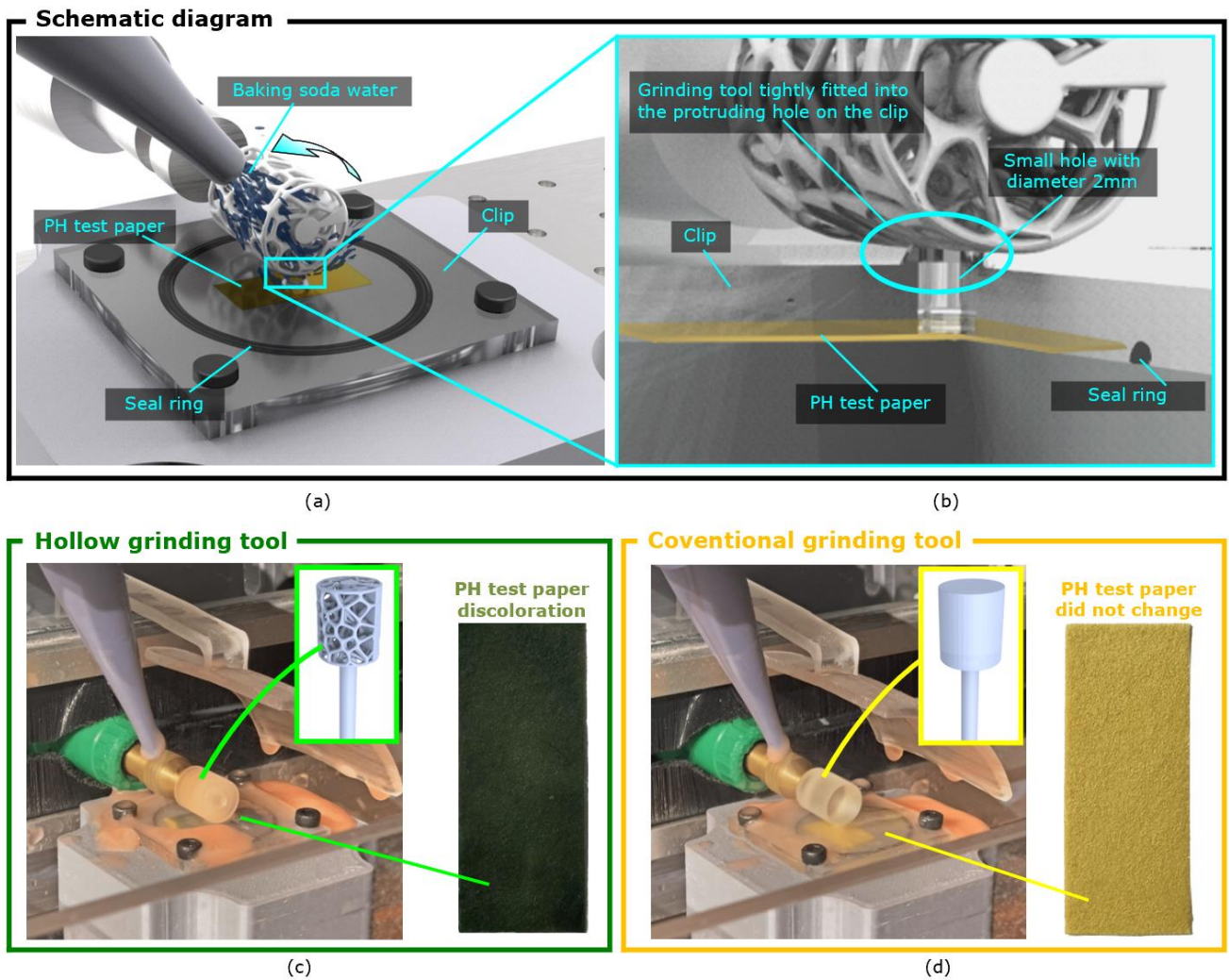


Figure 3-8: Permeability of the coolant fluid: (a) Schematic diagram of our setup for assessing coolant fluid flow penetration and (b) cross section view, (c) experimental process and result diagram for hollow grinding tool, and (d) conventional grinding tool.

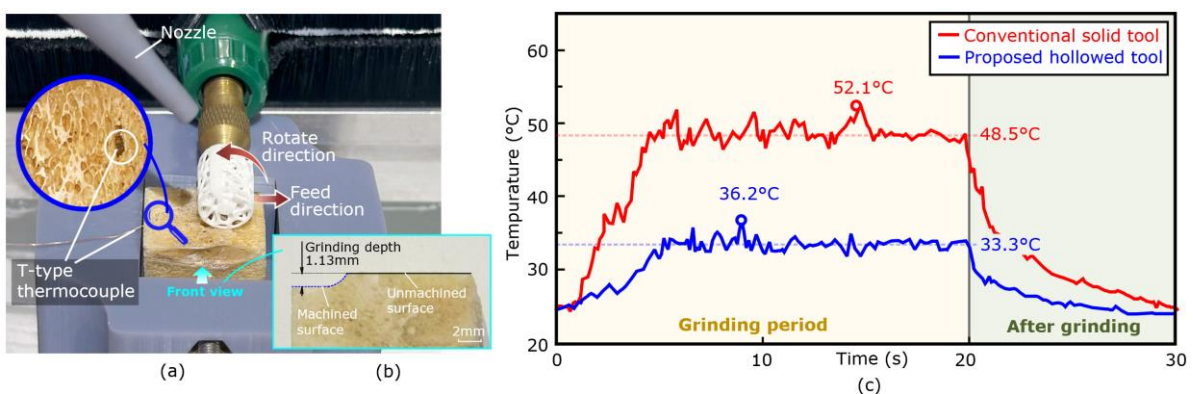
### 3.5 The in vitro assessment

#### 3.5.1 Grinding temperature

An additional experiment was conducted to analyze and compare the temperature increase between the conventional solid grinding tool and the newly proposed hollow grinding tool. The customized setup was similar to the one shown in Figure 3-7 but featuring a specially designed clamping stage. A

real pork rib bone was clamped and securely fastened using screws and plywood. A T-type thermocouple (KPS-T-0.08-2000-CZ, KAIPUSEN) was inserted into a through-hole in the bone sample. The measurement junction of the thermocouple was positioned at the top surface of the bone sample, while the other junction was connected to the data acquisition system (KPS04A0R, KAIPUSEN) (see Figure 3-9a). Both the solid and hollow tools were employed to grind the bone under identical conditions, maintaining the same rotation speed (6000 rpm) and grinding depth (1.13 mm).

As shown in Figure 3-9b, the grinding temperature using the conventional solid tool stabilized at approximately 48.5°C, whereas the proposed hollow grinding tool exhibited a significantly low temperature of 33.3°C. The temperature with the hollow tool was 31.3% lower than that of the conventional tool, with the highest temperature of only 36.2°C. In contrast, the conventional tool reached the highest temperature of 52.1°C, which could cause serious and irreversible damage to bone cells (According to the literature, irreversible damage can occur when the temperature at the grinding zone reaches [96, 97]).



### Chapter 3 Hollow grinding tool

Figure 3-9: temperature raise assessment; (a) experiment setup, b) front view of the grinded bone and c) temperature raise result for both the solid the hollowed grinding tool.

#### 3.5.2 Grinding trial on real bone

The experimental setup of grinding trials on real bone was shown in Figure 3-10. A real pork rib bone was clamped and secured by screws and plywood. The grinding tool and grinder were mounted on a linear module. The grinding tool was fed along the Y axis at the speed of 2 mm/min and turned counterclockwise at the speed of 6,000 rpm until the tool passed the full length of the bone. Hollow grinding tool and conventional solid grinding tool are both 3D printed ceramics.

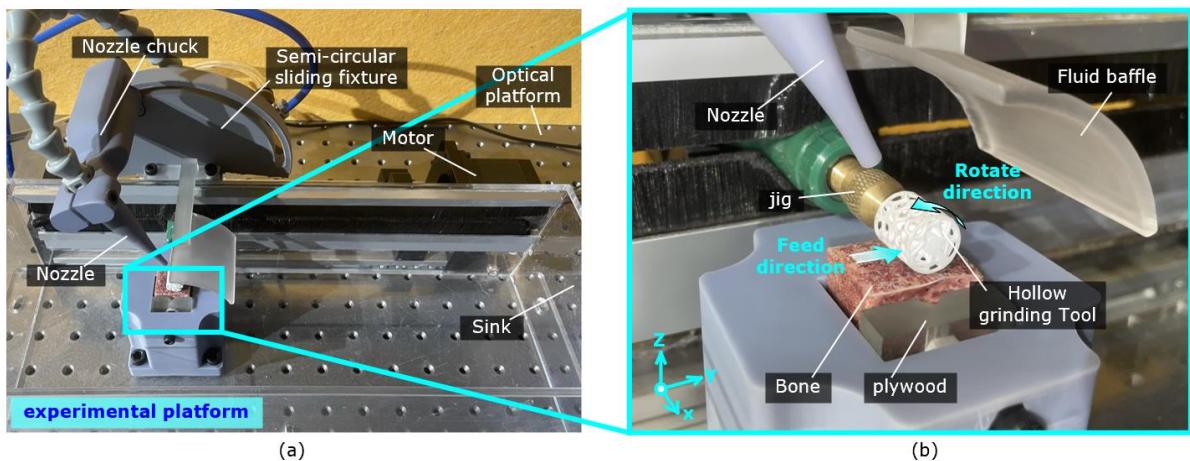


Figure 3-10: (a) Global and (b) detailed images of the experiment setup for real bone grinding

In Figure 3-11a and 3-11b, the bone before grinding contained trabecular structures. When grinding with conventional tools, a pungent odor was noticeable, and the surface of the ground bones darkened (Figure 3-11e). This might be due to the high temperatures during grinding, which denatured the proteins, producing unpleasant smells. The high temperature also generated a

mixture of bone protein, blood, and bone dust, which exhibited a burnt smell and blurred morphologies [98]. Additionally, it was observed that most of pores within the trabecular structures were filled with bone debris (Figure 3-11c, d), and no bone debris was detected on the tool surface after grinding (Figure 3-11i). This suggested that the debris generated during grinding were likely forced into the trabecular pores, potentially leading to infections and osteosis in later stages [98]. In contrast, the bone grinded with the proposed tool retained clear trabecular structures (Figure 3-11h). Only few chips were observed in the pores (Figure 3-11g), indicating that the debris were effectively removed by both the cutting fluid and the hollow tool. A small number of debris was found on the struts of the proposed tool after grinding (Figure 3-11j), proving our statement. However, these debris could be easily removed through simple ultrasonic cleaning, allowing the proposed tool to be reused multiple times with minimal tool wear.

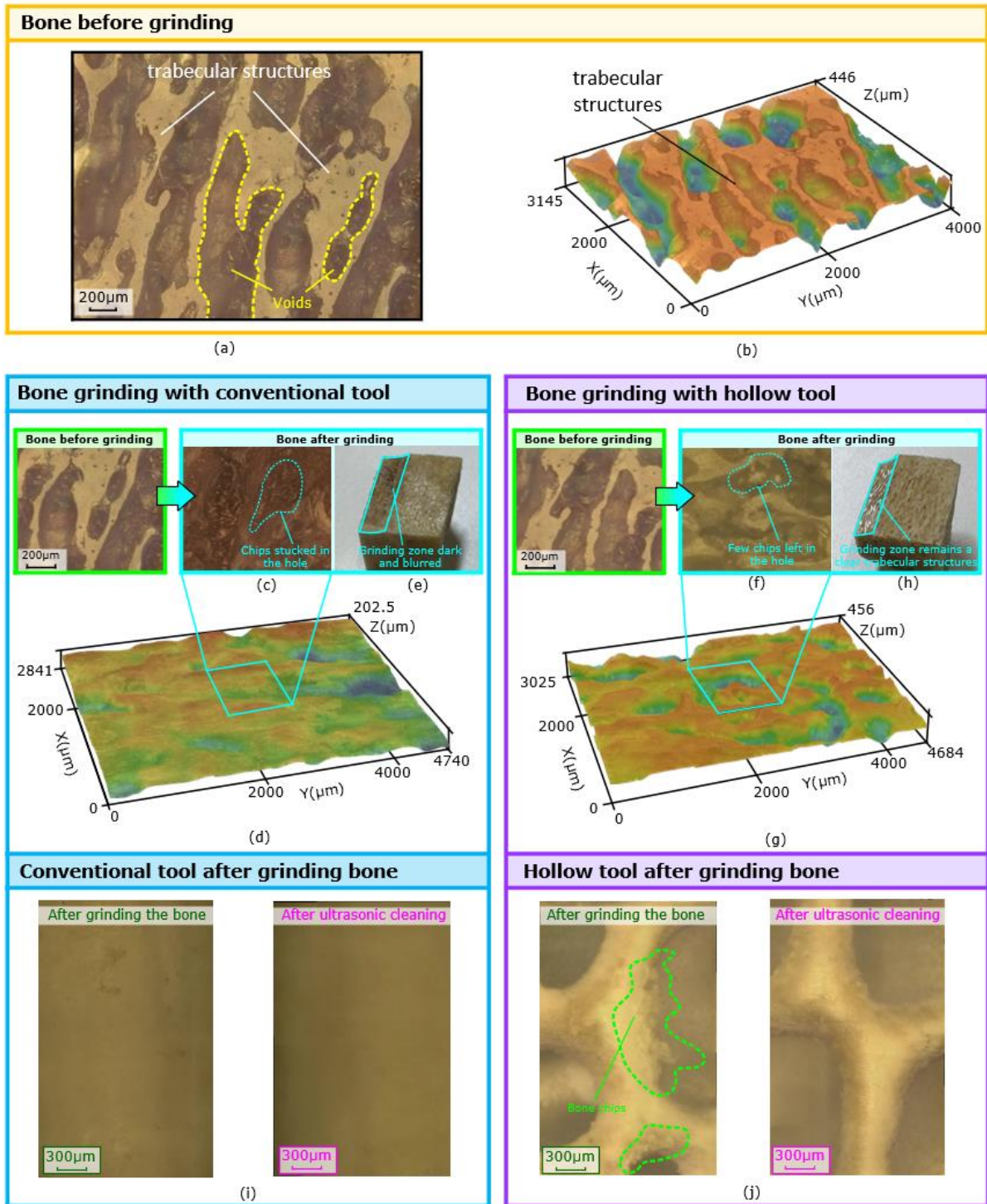


Figure 3-11: Comparison of the surface texture for the bone grinded with conventional solid grinding tool and hollow grinding tool: (a) 2D and (b) 3D morphology of the real bone before grinding using the 3d profilometer; (c) 2D, (d) 3D morphology and (e) real picture of the grinded bone using conventional solid grinding tool; (f) 2D, (g) 3D morphology and (h) real

picture of the grinded bone using proposed hollow grinding tool; microscopic images of (i) conventional solid grinding tool and (j) hollow grinding tool after grinding the bone.

### **3.6 The in vivo assessment**

#### **3.6.1 Method**

After confirmation of our tool ability in vitro assessment, we proceeded to conduct an in vivo assessment to further evaluate its performance under real surgical conditions. This experiment was approved by the Ethics Committee of Ningbo University. Sprague Dawley rats aged 6 to 8 weeks, were selected for the study and divided into three groups: the control group, the conventional solid tool group, and the proposed hollow tool group (n=6). The procedure was as follows: each rat was anesthetized with ketamine (60 mg/kg i.p. for rats; 100 mg/kg i.p. for mice) and then secured on an animal operating table. The fur on the rat's head was shaved off and cleaned with iodine before making an incision. The skin and muscle tissue of the head were then cut away to fully expose the skull. The grinding tool was used to grind the rat skull at the same location for each group. The skull temperature was recorded every second using an infrared camera (FLIR One Pro), and the highest temperature was taken until the tests were finished. Following the procedure, the rats were euthanized, and 4  $\mu$ m tissue slices were prepared according to standard protocols for subsequent analysis.

After dewaxing and rehydrating the tissue sections from each group, the sections were stained with hematoxylin solution (Solebao Bio, China) for 10 minutes, differentiated with weak acid, and then washed with distilled water. Sections were then stained with eosin solution (Solebao Bio, China) for 3 mins, then dehydrated with gradient alcohol and cleared in xylene. The optical microscope (Lecia Microsystems GmbH, Germany) was then used to observe the slices.

To assess apoptosis in brain tissue cells at the grinding site, the Apoptosis Detection Kit (Elabscience Biotechnology, Inc., China) was employed. As directed by the manufacturer, tissue sections were routinely processed and incubated with TUNEL reagent (apoptotic cells showed green fluorescence), sections were counterstained with DAPI (blue fluorescence) and images were acquired using confocal microscope (Leica TCS SP5TCSSP5, Germany).

#### **3.6.2 Results and discussion**

For the conventional tool, the temperature at the grinding region was 33.3°C before grinding (Figure 3-12b), while after grinding the maximum temperature reached 45.2°C (Figure 3-12c). For the proposed tool, as the coolant can easily reach the tool-bone interface, the temperature only reached 35.6°C (Figure 3-12d). This value was well below the critical threshold for irreversible thermal osteonecrosis. The above statement was further confirmed by checking the brain tissue under the grinding region. Figure 3-12e shows healthy brain tissue

from the control group with no grinding intervention. Figure 3-12f depicts the cross-sectioned brain beneath the conventional tool's grinding site. A noticeable eosinophilic change (dark blue region) was observed in the cerebral cortex accompanied by inflammatory cell infiltration. Moreover, a few edema areas were obviously visible in the deep part. In contrast, the cross-sectioned brain from the proposed tool group did not show significant changes compared to the control group. To further explore thermal damage to the neuro cells under the skull caused by different tools, Terminal deoxynucleotidyl transferase dUTP Nick End Labeling (TUNEL) staining was used to assess apoptosis of brain tissue cells. It can be found that, for the conventional tool group, the number of cerebral cortical apoptotic cells (green fluorescent) in the rat's brain significantly increased due to grinding heat induced injury (Figure 3-12i). However, for the hollow tool group, the number of apoptotic cells (Figure 3-12j) in the rat brain did not show noticeable increase and the status of the cells were similar to the control group (Figure 3-12h). All the above results indicates that, when grinding the skull, the use of proposed tool can effectively reduce the temperature of the skull at the grinding site and effectively avoid the damage of the underlying soft tissues.

### Chapter 3 Hollow grinding tool

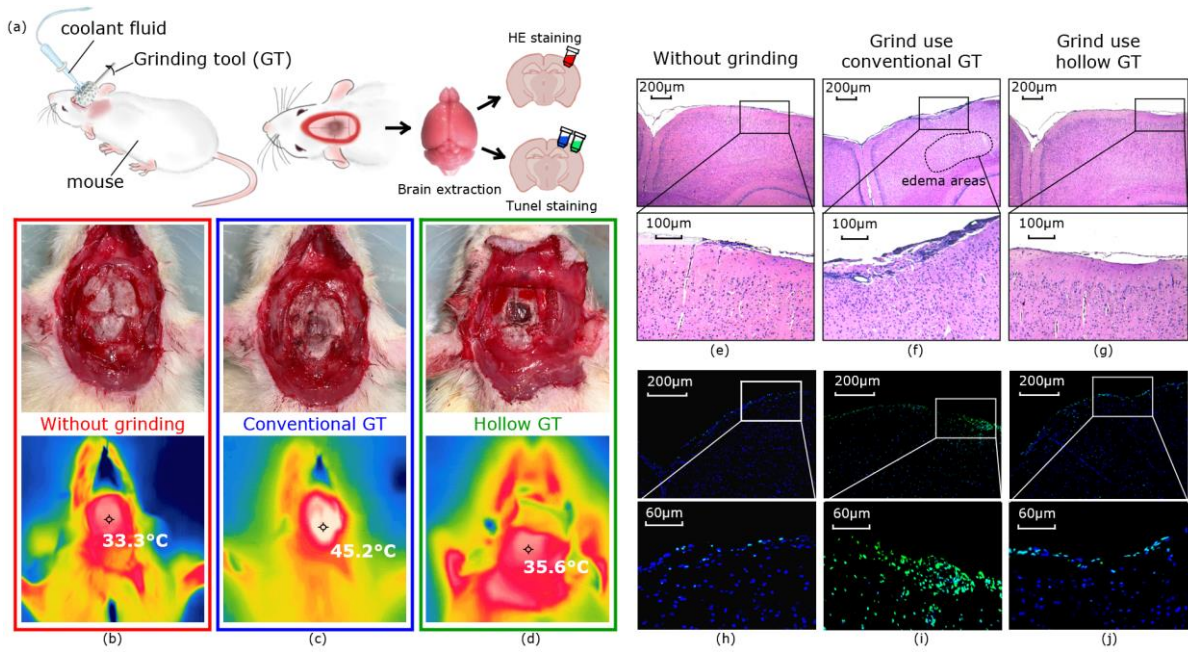


Figure 3-12: In vivo experiment designed to compare the efficiency between conventional solid grinding tool and hollow grinding tool: (a) Schematic diagram of in vivo assessment process; Infrared thermogram in (b) control group, (c) conventional grinding tool group, and (d) hollow grinding tool group; HE staining figure in (e) control group, (f) conventional grinding tool group, and (g) hollow grinding tool group; TUNEL staining figure in (h) control group, (i) conventional grinding tool group, and (j) hollow grinding tool group.

## Chapter 4 Closed-loop temperature control grinding device

### 4.1 Introduction and motivation

As mentioned before, excessive heat generated during the bone grinding process can lead to severe consequences in craniostylosis surgery [99]. The current solution is to continuously supply coolants to mitigate temperature spikes. However, this approach is empirical, i.e. surgeons are not only unable to determine the spraying location and injection rate, but also can not monitor and precisely control the temperature in the surgical area.

In this chapter, we propose the grinding tool (see Section 4.2) with not only the conformal cooling channels but also the closed-loop temperature control system. This concept allows not only precisely monitor but also regulate temperature in craniostylosis surgery. The tool is fabricated by using Selective Laser Melting (SLM) (Section 4.3, Figure 4-1b). The CFD model is performed to simulate coolant flow behavior in the cooling channels (Figure 4-1c). The temperature controlling performance is tested in Section 4.5 and the temperature fluctuation results are obtained (Figure 4-1d). In section 4.6, the grinding trials are performed on real bones (Figure 4-1e).

## Chapter 4 Closed-loop temperature control grinding device

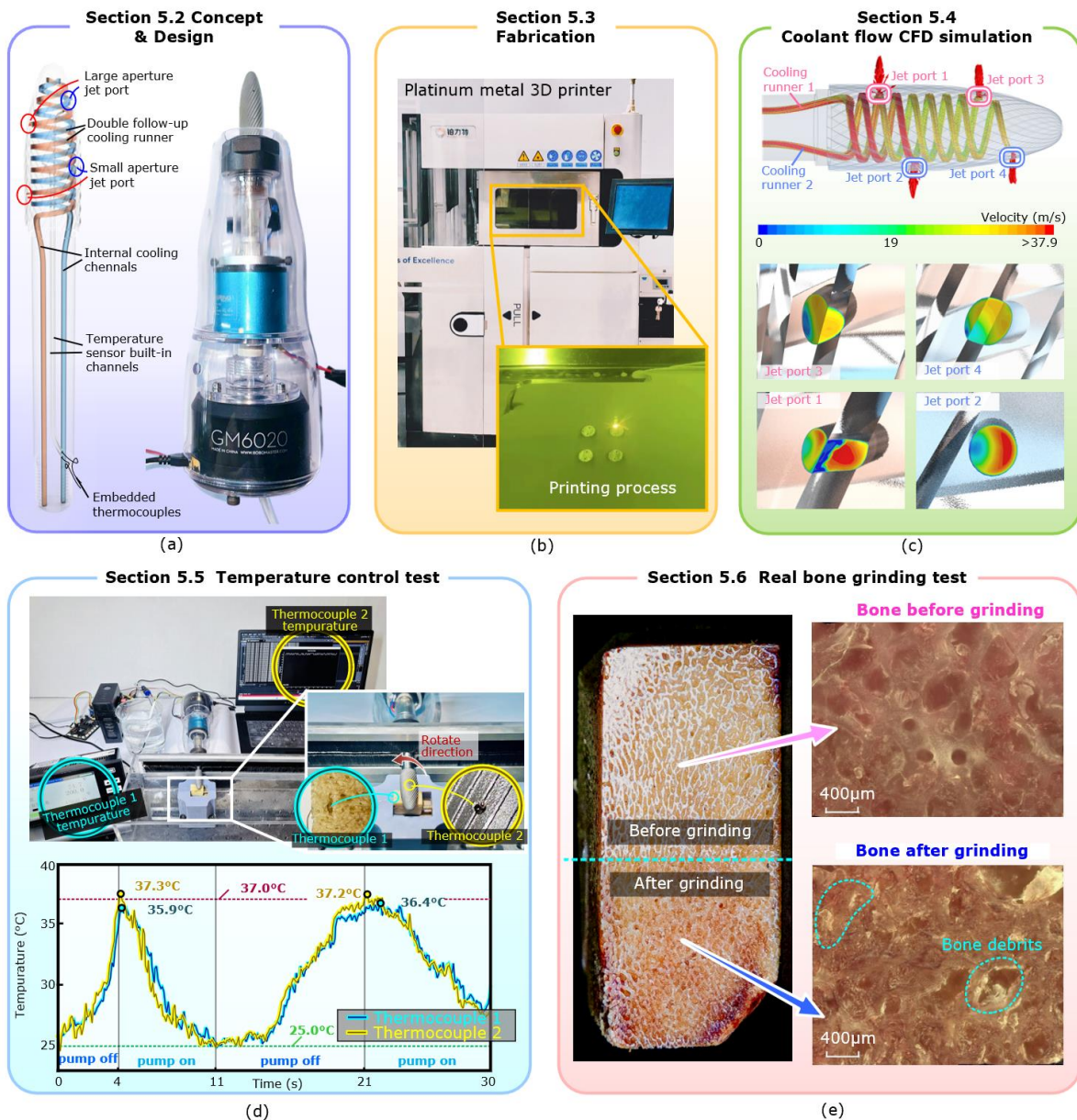


Figure 4-1: the methodology that we followed to design, fabricate and verify our proposed closed-loop grinding device: (a) design grinding tool and device, (b) fabrication of designed grinding tool (c) simulation for the coolant flow behavior, (d) testing the temperature control performance, and (e) verification of the grinding tool performance in vitro.

## 4.2 The closed-loop grinding device concept and design

### 4.2.1 Concept

In contrast to a single grinding tool with an open-loop coolant supply system (Figure 4-2a), we design a closed-loop temperature control grinding device (Figure 4-2b). The specialized conformal cooling grinding tool with integrated temperature sensors is developed utilizing additive manufacturing technology. These sensors enable continuous monitoring of the grinding surface temperature, providing real-time feedback to the surgeon. The grinding tool also incorporates internal cooling channels to facilitate coolant delivery. When the temperature measured by the sensors exceeds the predefined threshold, the system automatically activates the water pump to initiate coolant irrigation. Conversely, when the temperature drops below the specified limit, the pump is deactivated, ensuring the maintenance of an optimal temperature range. Traditional open-loop grinding strategies in craniostomy surgery lack precise temperature control and coolant dispensation, placing additional burdens on the surgeon (concerning about potential tissue damage due to heat accumulation). The proposed close-loop temperature control grinding device enhances surgical precision by allowing the surgeon to focus solely on the procedure, thereby reducing the risk of complications, expediting patient recovery, and improving overall patient outcomes.

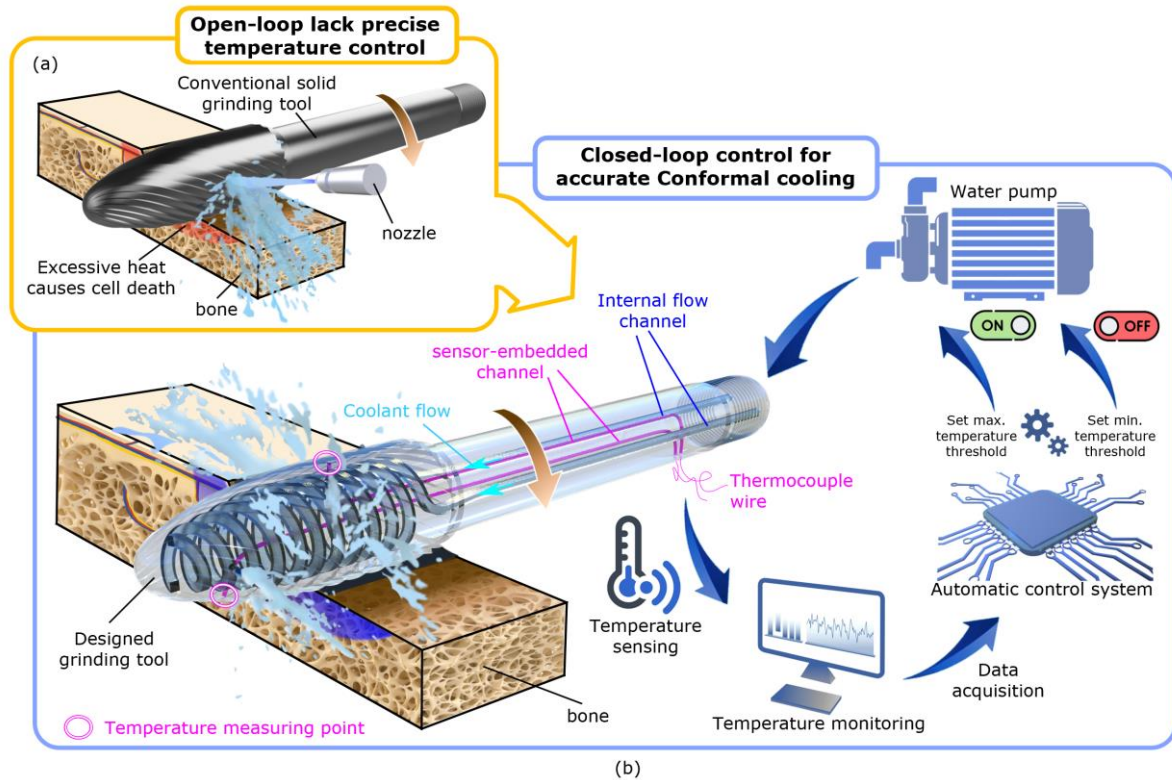


Figure 4-2: Conceptual diagram of (a) conventional open-loop grinding process and (b) proposed closed-loop temperature control grinding device.

#### 4.2.2 Grinding tool design

Our grinding tool is designed and fabricated by additive manufacturing techniques [100-102]. The tool integrates several unique features to enhance its performance: (i) a cutting portion, (ii) embedded temperature sensors, and (iii) internal cooling channels with the conformal shape.

**(i) Cutting portion.** The cutting portion has evenly-distributed, spiral, serrated, and grooved cutting edges for powerful bone removal [103, 104]. To accomplish double-function removal, this portion is designed to incorporate both a cylindrical part intended for large-area and high-efficiency bone removal, and a curved part aimed at small-area and fine bone finishing and polishing.

**(ii) Embedded thermocouples.** To enable closed-loop cooling, two thermocouples are integrated and embedded within the grinding tool. The measurement junctions of these thermocouples are positioned separately in counterbores located at the cylindrical and curved cutting portions, while the thermocouple cables are routed through a pre-designed channel.

**(iii) Internal cooling channels.** Double spiral internal channels are designed for coolant flow (Figure 4-3a, green label). These channels are designed to conform closely to the tool's shape profile, optimizing the heat transfer efficiency from the tool surface. Each channel features two exits: one at the cylindrical part and another at the curved part. The exit at the cylindrical part is designed with a smaller diameter compared to the curved part, ensuring a consistent flow rate of the coolant, in accordance with Bernoulli's principle.

**Dimensions.** The double-function portion of the grinding tool features a diameter of 13 mm and a length of 35 mm. The overall length of the tool is designed to be 107 mm, with a rod diameter of 10 mm to ensure compatibility with standard surgical bone drills [105].

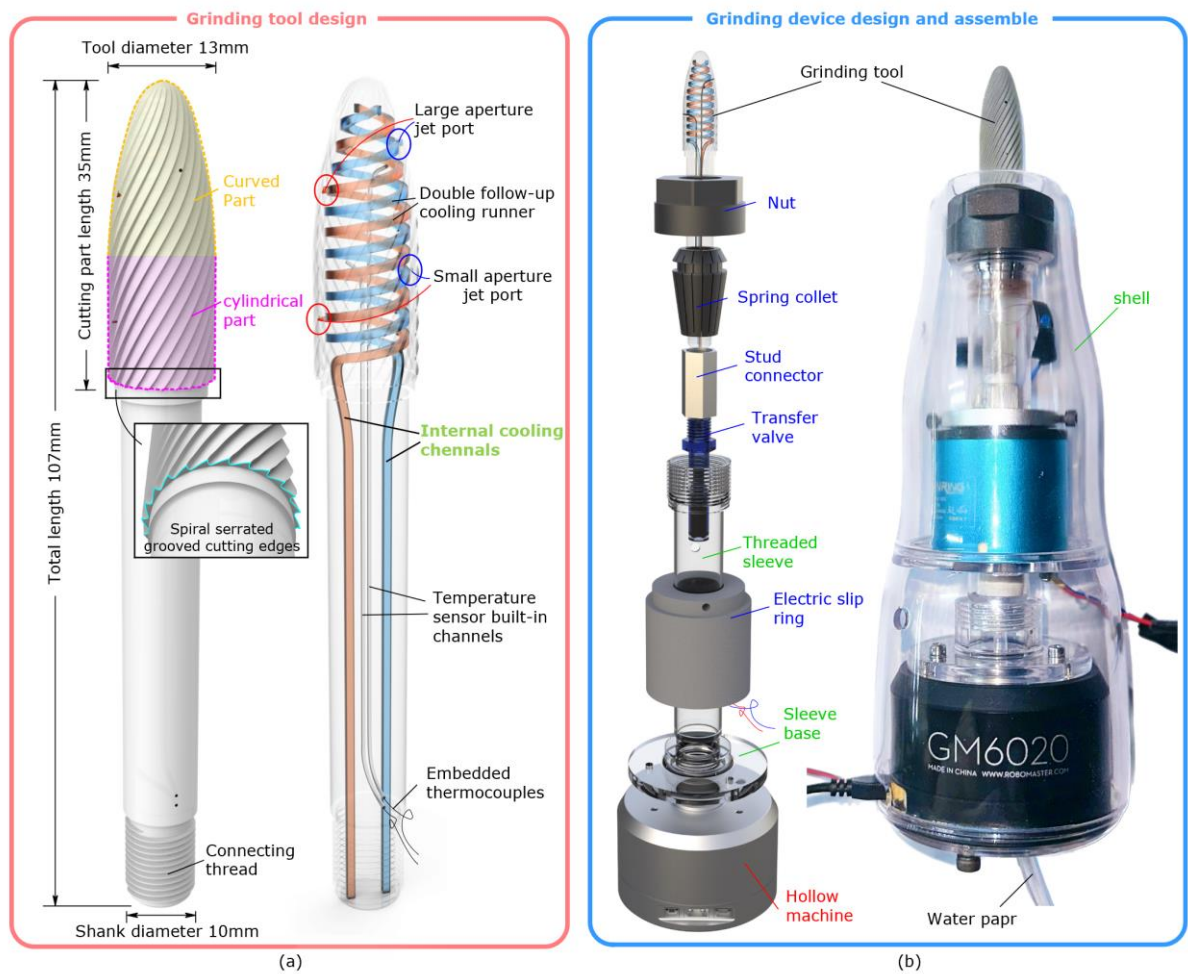


Figure 4-3: A specific design diagram of grinding tool and device: concept design of (a) proposed grinding tool and (b) proposed closed-loop temperature control surgical device.

### 4.2.3 Grinding device assembly

Figure 4-3b presents the design and assembly diagram of the closed-loop grinding device, which is divided into two main components: (i) the connection system (Figure 4-3b blue label) and (ii) the non-standard parts (Figure 4-3b green label).

**(i) Connection system (Figure 4-3b blue label):** An electric slip ring is used to connect the wires, allowing the thermocouple sensors and grinding tool to rotate simultaneously. To achieve the desired closed-loop cooling functionality,

a water pipe was connected to the grinding tool via the transfer valve and stud connector. Additionally, a spring collet and nut were utilized to secure the grinding tool to the entire device.

**(ii) Non-standard parts (Figure 4-3b green label):** The threaded sleeve and sleeve base provides structural support to the entire grinding device, with these components being customized to ensure stability. Furthermore, a fully transparent shell is designed and fabricated using 3D printing to enhance handling and improve aesthetics.

#### **4.2.4 Electrical system design**

The electrical system is divided into five modules: the motion module (Figure 4-4, green), the power supply module (Figure 4-4, blue), the display module (Figure 4-4, purple), the sensor module (Figure 4-4, red), and the transmission module (Figure 4-4, yellow). (i) The motion module comprises a hollow motor (ROBOMASTER GM6020, DIJ, China) and a water pump (DC4.5V, Vickers, China); (ii) The power supply module includes a smart battery (M600, DIJ, China) and an ESC center board; (iii) The display module is equipped with an OLED display module (0.69-inch 4-pin, Telesky, China); (iv) The sensor module features a thermocouple digital converter (MAX6675, Telesky, China), an electric slip ring (10A, Mofulon, China), and a thermocouple (K-type, Kepson, China); (v) The transmission module consists of a Bluetooth module (HC-05, ZAVE, China).

In this study, the development board (ROBOMASTER STM32F427IIH6, DIJ, China) is used as the control core of the above five modules. These modules handle various functions, including the closed-loop control of the motor's start and stop speed, the activation and deactivation of the water pump, temperature reading, and information transmission. Each module is connected to the development board through its specific communication protocol, ensuring that different control requirements are met efficiently.

The battery supplies 24V to the ESC center board, which in turn powers both the development board and the motor. The motor realizes start, stop, and speed control through CAN communication with the development board. The water pump driver is powered by the development board and controls the switch through TTL signals. The OLED display receives power from the development board, with data being transmitted through IIC communication to display relevant information. The thermocouple is connected to an electric slip ring to avoid wire entanglement and is linked to a thermocouple-to-digital converter. This converter is powered by the development board and transmits data via SPI communication. The Bluetooth module is responsible for transmitting temperature data to the host computer, which stores the data and generates a real-time curve.

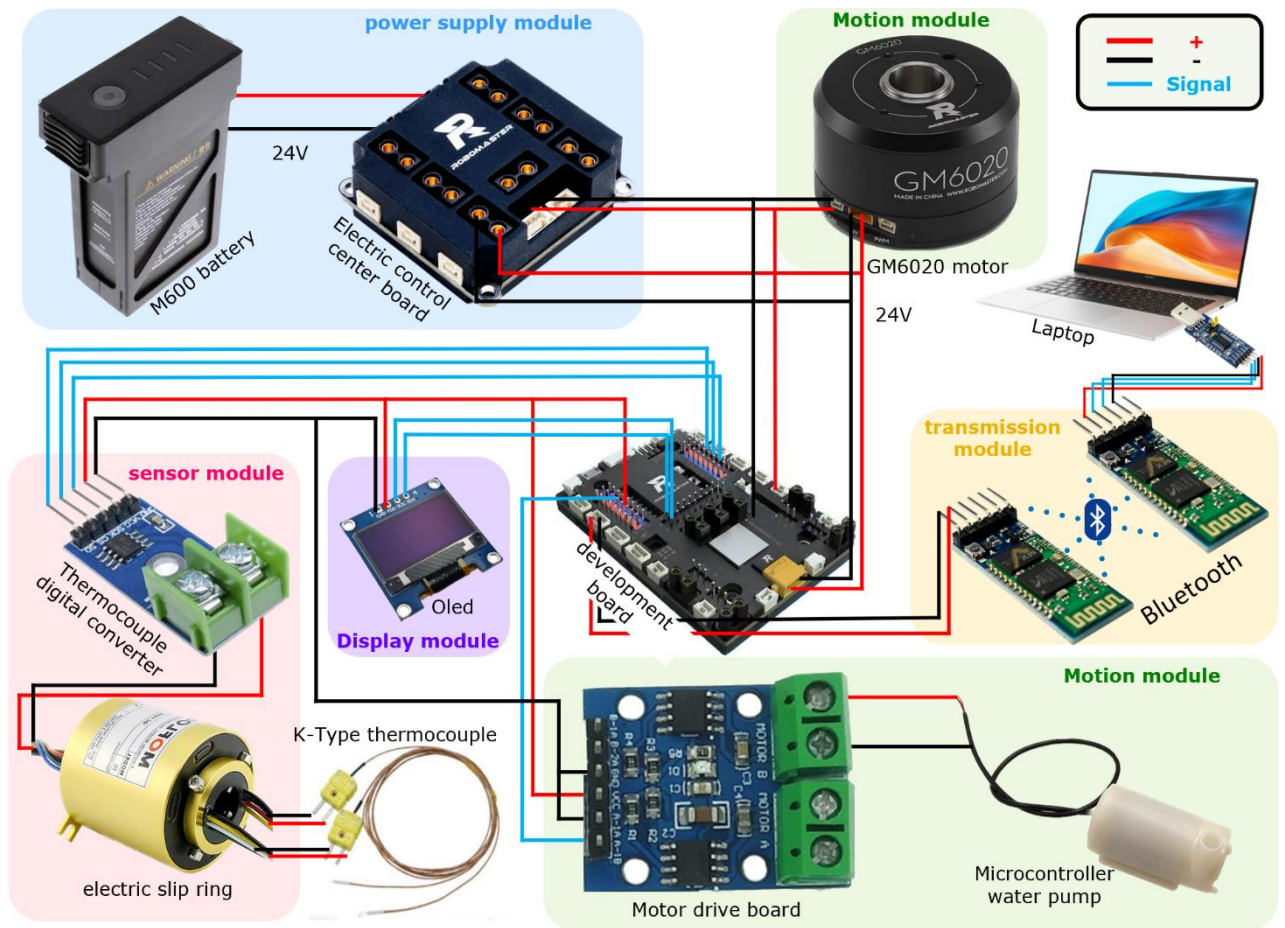


Figure 4-4: Electrical System diagram: blue) power supply module; green) motion module; red) sensor module; purple) display module; yellow) transmission module.

#### 4.2.5 Software system design

The board program is developed using Keil5 software with C language. Subsequently, various peripherals are initialized, including General-Purpose Input/Output (GPIO), Controller Area Network (CAN) communication, timers, and Universal Asynchronous Receiver-Transmitter (UART) serial communication. Specific initializations are also carried out for components such as LEDs, OLED displays, motors, temperature sensors, and water pumps. The system is designed to follow the temperature data from the sensors, triggering the

corresponding control logic: if the temperature surpasses the pre-set threshold, the water pump is activated; otherwise, it remains off. This setup enables real-time temperature monitoring (sampling frequency: 3.125 MHz) and controls the operation of the water pump and motor based on the sensor data.

The host computer program is developed using Microsoft Visual Studio 2022 with Python. Temperature data from the sensor is logged and stored in Excel. The real-time temperature curve is visualized using PyQt6 and PyQtGraph, with the current temperature displayed on the interface. A timer regularly triggers data updates, ensuring real-time data refresh at high frequency, which enables the detailed observation and recording of subtle temperature changes.

### **4.3 The Fabrication and the geometrical/mechanical evaluation**

#### **4.3.1 Fabrication route**

The STL model was processed using Magics software (version 24.0) for slicing, and the grinding tools were fabricated with an SLM 3D printer (BLT S200, China), as illustrated in Figure 4-5. The printing parameters included a layer thickness of 0.03mm, a scan speed of 1200mm/s, a hatch distance of 0.1mm, and a laser power of 165W. TC4 powder (BLT) with the particle size of 15-53 $\mu$ m was utilized. Under the action of high laser energy density with a laser beam diameter of 0.1mm, the metal powder melted and formed a solid metal after cooling by heat dissipation. To prevent reactions between the metal and other gases at elevated temperatures, the printing chamber was sealed and filled with argon gas. A

schematic representation of the printing process is provided in Figure 4-5b. The printed grinding tool was clamped onto the grinding machine and was firmly fixed. The sand wheels were sequentially used from low sand number (#120) to high one (#600) at the speed of 6000 rpm for grinding. The grinding effect of the printed tool was checked every 5 minutes to ensure that the rod surface was smooth. After grinding, the surface was wiped with a clean cloth to ensure no dust or debris residue. Finally, the ground rod was polished with #2000 grit diamond sand powder.

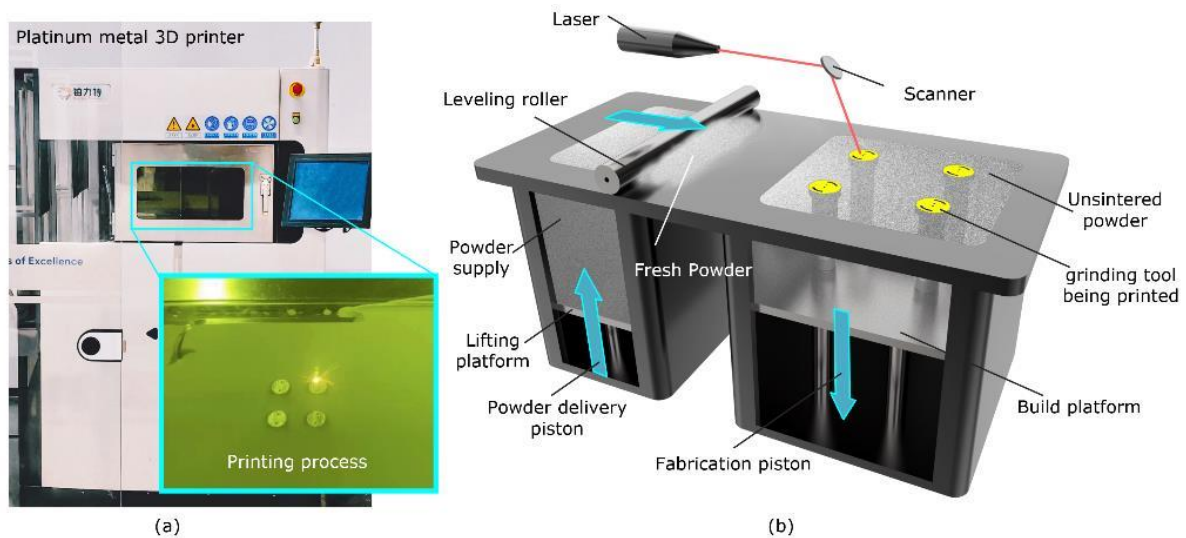


Figure 4-5: Fabrication diagram: (a) BLT printing process and (b) BLT printing principle.

### 4.3.2 Geometrical and mechanical evaluation

Figure 4-6a displays the grinding tool produced by SLM. The rod of the grinding tool was polished to ensure it has good contact with other components during assembly. However, the head of the grinding tool was left rough, as this roughness can enhance the tool's grinding performance during use. Figure 4-6b provides an enlarged view of the large aperture jet port in the curved section of

the grinding tool, revealing that the hole shape and size was accurately printed, with a diameter of 800  $\mu\text{m}$ . Figure 4-6c and d illustrate that the edge surfaces of the printed tool exhibit roughness, with numerous metal particles and droplets adhered. This roughness is anticipated to enhance grinding and removal efficiency during surgery, despite being the byproduct of the fabrication process [106].

Figure 4-6e presents a transverse cross-section of the additively manufactured grinding tool. The dimension of the actual printed cooling channel—length 1002  $\mu\text{m}$  and width 909  $\mu\text{m}$ —aligned closely with the design of length  $969.8 \pm 7.8 \mu\text{m}$  and width  $887.4 \pm 9.2 \mu\text{m}$ , exhibiting a deviation of approximately 3-4%. Additionally, the grinding head was cross sectioned longitudinally to assess the presence of voids and to measure the inner surface roughness of the printed channel (as shown in Figure 5f). No inner voids were detected in the cross-section of the printed grinding tool. On the surface of the inner cooling channel, partially melted particles were noted. To quantify the surface quality, a 3D surface morphology test was conducted using an ultra-depth three-dimensional microscope (shown in Figure 5g). The Rz value of the inner surface measured  $25.51 \pm 6.9 \mu\text{m}$ , which is approximately the average size of the powder used. This roughness, however, represents only 2.5% of the designed dimensions and could be further reduced through abrasive flow machining

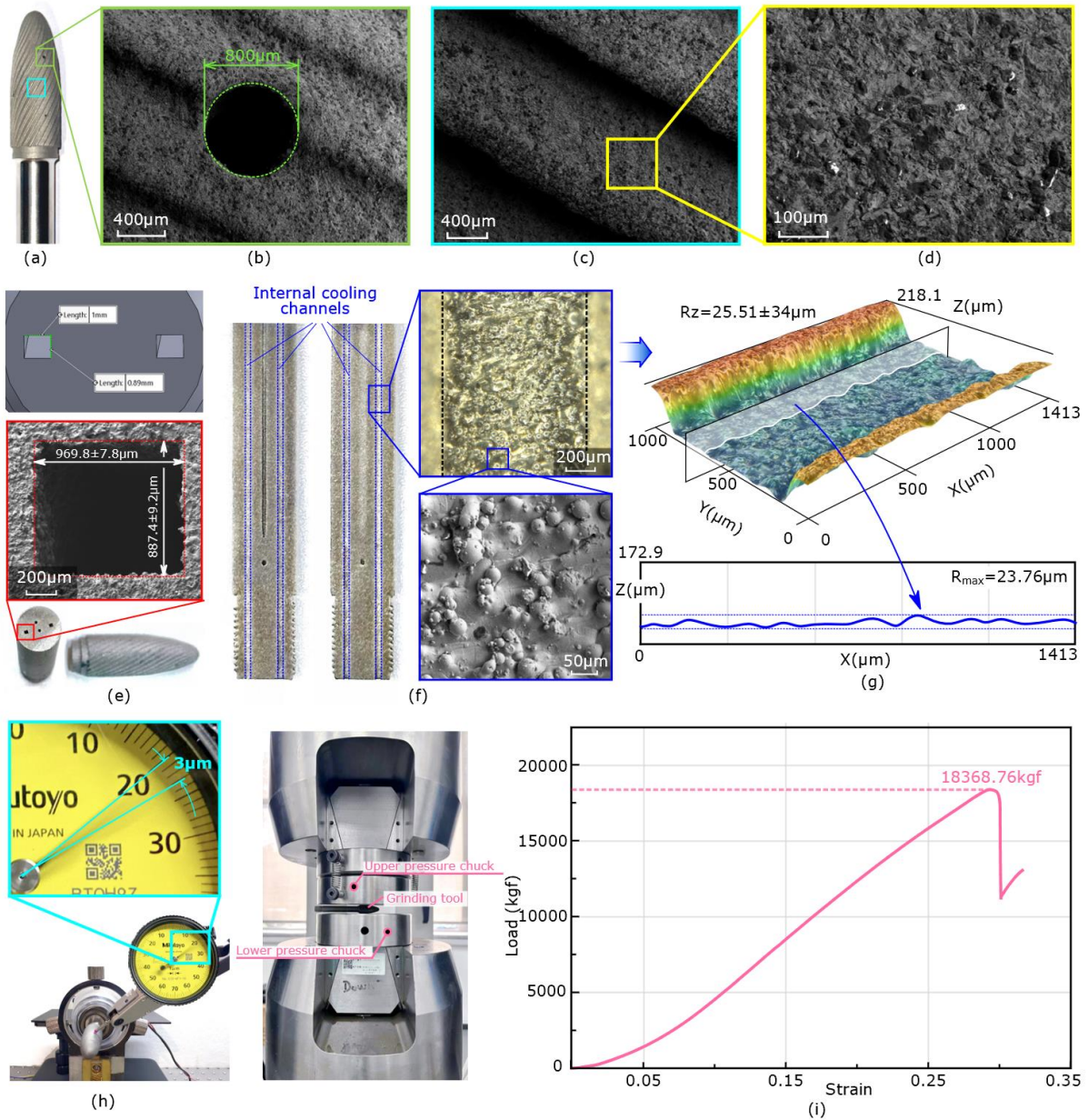


Figure 4-6: Evaluation of the printed grinding tools: (a) sample picture and (b-d) SEM morphological images of 3D printed grinding tools; (e) transverse cross section and (f) longitudinal cross section of the printed cooling channel; (g) 3D morphology of the internal cooling channel surface using ultra-depth three-dimensional microscope; (h) dynamic balancing results; (i) tensile test and obtained load-strain curve.

The rotation error is a critical parameter for evaluating rotating tools and devices, and it is assessed here through a dynamic balance test (see Figure 4-7e). A dial indicator probe is delicately positioned against the rotating grinding

tool (at 6000 rpm), and the vibration range of the pointer indicates a rotation error of 3 $\mu$ m. This minimal error is negligible in actual surgical scenarios, considering potential external factors like hand jitter [88, 89]. The strength (another key indicator of the mechanical properties of the grinding tool) is tested as shown in Figure 4-6f. The tool withstood a load of 1836.76 kgf before failure, demonstrating that it is sufficiently robust to be used as a surgical tool for bone tissue removal [90, 91].

### 4.4 CFD simulation of internal cooling channel

To verify that the coolant effectively traverses the designed double-helical conformal inner cooling channels and is expelled from the jet ports, CFD models are utilized to simulate coolant flow behavior.

#### 4.4.1 Method

All the CFD simulation calculations presented in this chapter are performed using STAR-CCM+. The coolant is modeled as an incompressible fluid. The Standard K-Epsilon turbulence model is employed to simulate the rotational dynamics of the coolant around the grinding tool. For boundary conditions: the inlet is configured as a mass flow inlet with a flow rate of 0.0133 kg/s, and the outlet is designated as a pressure outlet at atmospheric pressure (0 Pa).

The mesh is configured with a base size of 1 mm, incorporating 5 element layers and a boundary layer expansion factor of 1.2. The boundary layer thickness is 25% of the base size. The rotational speed of the tool is set to 6000 rpm to

simulate the rotational motion. To achieve optimal convergence, the time step is set to 0.001s to keep the Courant number below 1. The maximum number of inner iterations is limited to 10, and the simulation is run for a maximum physical time of 4.54s. This corresponds to 10 complete coolant rotations, ensuring that the flow reaches a sufficiently stable state.

### 4.4.2 Results and discussion

Figure 4-7a illustrates the velocity vectors of the coolant within the double-helical conformal inner cooling channels. The simulation revealed that the coolant exhibited high flow rates before exiting through the lower two jet ports (jet port 1 and jet port 2) in each cooling channel. Conversely, the velocity notably diminished in the segment of the cooling channel situated between the lower and upper jet ports (jet port 3 and jet port 4). Once the coolant exited through the jet ports (jet port 3 and jet port 4), there was a cessation of coolant flow in the upper channels. Despite this reduction in coolant velocity within the inner cooling channels, it was unlikely to impact the conformal cooling efficiency significantly. This might be because the coolant adequately cools the grinding tool and subsequently the grinding area. Additionally, due to the high thermal conductivity of metal materials, the conformal cooling effect was effectively distributed throughout the grinding head component.

To ensure uniform coolant flow through the four jet ports, the two lower jet ports (jet port 1, 2) were designed with smaller diameters, while the two upper

jet ports (jet port 3, 4) were designed with larger diameters. To assess the effectiveness of this design, the velocity distribution across the four jet ports was analyzed (see Figure 4-7b and c). The results showed that jet port 1 had the highest coolant flow velocity at 38 m/s, which was 17% higher than the maximum velocity observed at jet port 4. Despite this variation, the average velocities across the jet ports were relatively similar, with the highest average flow velocity being only 2.52 m/s greater than the lowest. This consistency may be attributed to jet port 2, which was less affected by the spiral blade and retained a more intact shape. These findings confirm that (i) the coolant is expelled at a consistent rate from the jet ports to efficiently dissipate heat in the grinding area and remove bone debris, and (ii) the design allows the coolant to flow inward, effectively cooling the grinding tool.

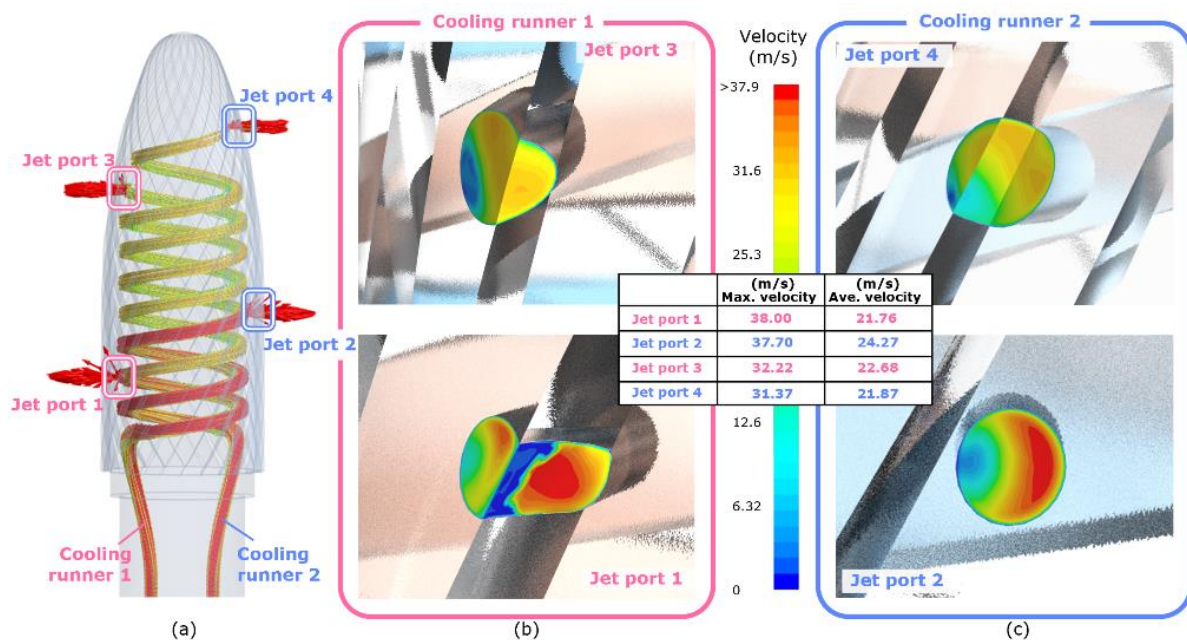


Figure 4-7: Simulated result of the coolant behaviours: (a) the coolant velocity vector in double cooling runners of proposed grinding tool and the velocity map of two jet ports in (b) cooling runner 1 and (c) cooling runner 2.

## 4.5 Closed-loop and temperature control test

### 4.5.1 Closed-loop test

To verify the response of the proposed grinding device to temperature changes, a validation experiment is conducted. The experimental setup is depicted in Figure 4-8: a beaker filled with water is placed on a magnetic stirrer (SH-2, FAITHFUL) for heating. A digital thermometer (TP300, Naz Trading Co., Ltd.) is inserted into the beaker to monitor the water temperature. The grinding device is mounted upside down on a support frame, with the grinding head containing an embedded thermocouple (KPS-JY-TT-K-44-SLE-1000-CZ, KAIPUSEN) immersed in the water. The temperature readings from the thermocouple are displayed on an OLED module (0.69-inch 4-pin, telesky, China). The coolant is pre-colored with blue dye for visibility.

Figure 4-8 illustrates the evaluation results for the closed-loop control performance of the designed grinding device. The digital thermometer (marked in yellow) and OLED display (marked in blue) shown in Figure 4-8 indicate the ambient water temperature and the temperature detected by the thermocouple embedded in the grinding tool, respectively. As depicted in Figure 4-8a, the temperatures recorded by the digital thermometer (26.5°C) and the OLED display (27°C) were consistent. Prior to reaching the threshold temperature, the coolant's water pump remained inactive. Once the water in the beaker was heated to the pre-set threshold of 37°C, blue coolant was

observed spraying from the internal cooling channels in the grinding tool (see Figure 4-8b). Note that a transparent resin-printed grinding tool was used in this experiment to clearly visualize the coolant injection process.

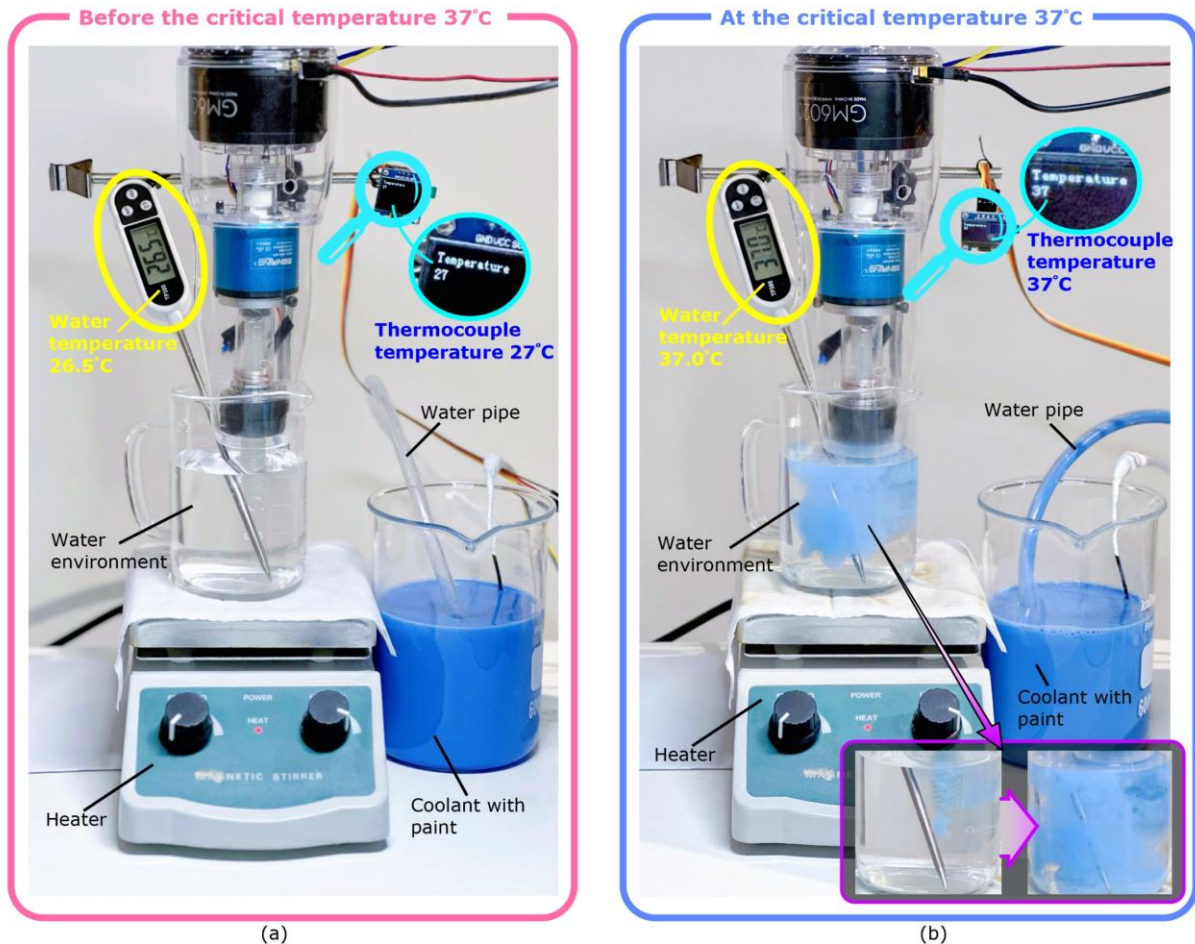


Figure 4-8: Closed loop experiment result for (a) before and (b) at critical temperature 37°C.

#### 4.5.1 Temperature Fluctuation Assessment

This test is designed to monitor temperature fluctuations at the grinding position (see Figure 4-9). The customized setup is created with a clamping stage, where a bone sample is secured in place using screws and plywood. Thermocouple 1 (KPS-JY-TT-K-44-SLE-1000-CZ, KAIPUSEN) is embedded in a through hole in the bone sample. A data acquisition device (KPS04A0R,

KAIPUSEN) is connected to the other end of the Thermocouple 1 to record the temperature at the surgical area. Another Thermocouple 2 (KPS-JY-TT-K-44-SLE-1000-CZ, KAIPUSEN) is inserted into the sensor channel of the designed grinding tool, with the measurement junction positioned at the tool surface. The tool temperature is monitored in real-time and transmitted to a laptop via Bluetooth. The grinding tool is then used to grind the bone where Thermocouple 1 is embedded, operating at 6000 rpm [106].

To assess whether the temperature measured by the Thermocouple 2 (yellow mark) embedded in the grinding tool accurately reflects the real temperature of the grinding zone (blue mark), a bone grinding temperature control comparison evaluation was conducted, revealing several noteworthy observations and results:

(i) When Thermocouple 2 reached the threshold temperature of 37°C, the coolant system activated, leading to a rapid cooling of both the grinding tool and the grinding area. Subsequently, when Thermocouple 2 dropped to the lower threshold temperature of 25°C, the coolant was deactivated, causing the temperature of the grinding tool and grinding area to gradually increase again. This confirmed that the temperature control device functioned as intended.

(ii) Figure 4-9c illustrates that the temperature trends of the two curves were consistent, with both showing simultaneous increases when the pump was off and decreases when the pump was on. Upon reaching the maximum grinding

temperature for the second time, the temperature recorded by Thermocouple 2 was only 0.8°C higher than that measured by Thermocouple 1, demonstrating the effectiveness of using thermocouples embedded in the grinding tool to gauge the temperature in the grinding zone.

(iii) The rate of temperature increase was notably slower during the second cycle when the water pump was turned off compared to the first cycle, with a temperature stabilization period lasting several seconds. This might be attributed to the coolant filling the internal cooling channels of the grinding tool, which altered the overall heat conductivity of the tool and delayed the rise in grinding area temperature even after the water pump was turned off.

(iv) The maximum temperature recorded by Thermocouple 2 was typically slightly higher than that of Thermocouple 1. This discrepancy might be due to the superior thermal conductivity of the metal grinding tool compared to bone, which efficiently conducted heat within the grinding area. Nonetheless, the highest temperature observed in the grinding area was only 36.4°C, well below the critical temperature of 47°C required to cause bone necrosis [96, 97].

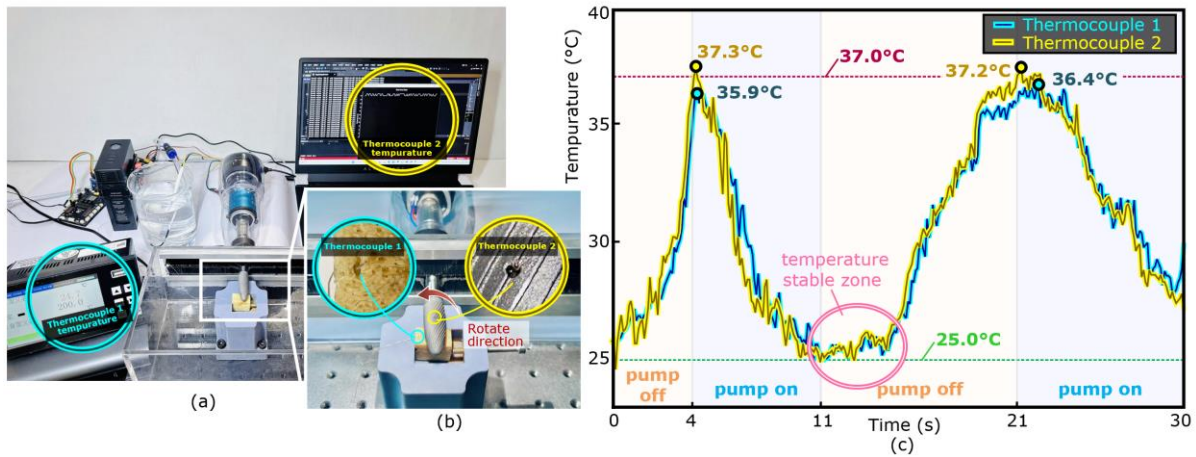


Figure 4-9: temperature control assessment; (a) global and (b) detailed images of the experiment setup, and (c) temperature control results for both grinding tool and grinding area.

#### 4.6 Grinding trial on real bone

The grinding test using real bone was conducted with the experimental setup detailed in Figure 4-9a and b. The observations from Figure 4-10 revealed several notable phenomena:

(i) Figure 4-10a illustrates the surface morphology of a bone specimen with its lower half ground. Prior to grinding, the bone exhibited a clear trabecular structure, a slightly flat surface, and noticeable reflections. After grinding, the surface became slightly rough with no visible reflections, though the trabecular structure remained discernible. This indicates that the proposed grinding tool preserved the original bone structure.

(ii) A comparison between Figure 4-10b and d shows that the trabecular edges of the bone were clear and intact before grinding. Post-grinding, some residual

bone debris remained, as noted in Figure 4-10c (blue mark). The 3D topography in Figure 4-10c confirms that while a small number of debris was present, the trabecular bone pores remained intact. This demonstrates that the internal coolant flow system of the closed-loop control grinding tool effectively removed most of the bone chips, significantly reducing the risk of postoperative complications from residual debris [98].

(iii) Figure 4-10d and f revealed minor wear on the edges of the grinding tool blade (yellow mark) after the bone grinding. This wear had minimal impact on the efficiency of short-term bone grinding procedures [35, 92].

(iv) SEM and EDS images of the grinding tool in Figure 4-10e show that while the tool surface was coated with bone debris, the coolant jet ports remained unobstructed and retained their original shape. This indicates that the high-velocity coolant jets effectively cleared away residual bone debris, allowing for smooth coolant ejection from the internal channels and effective cooling of the grinding area.

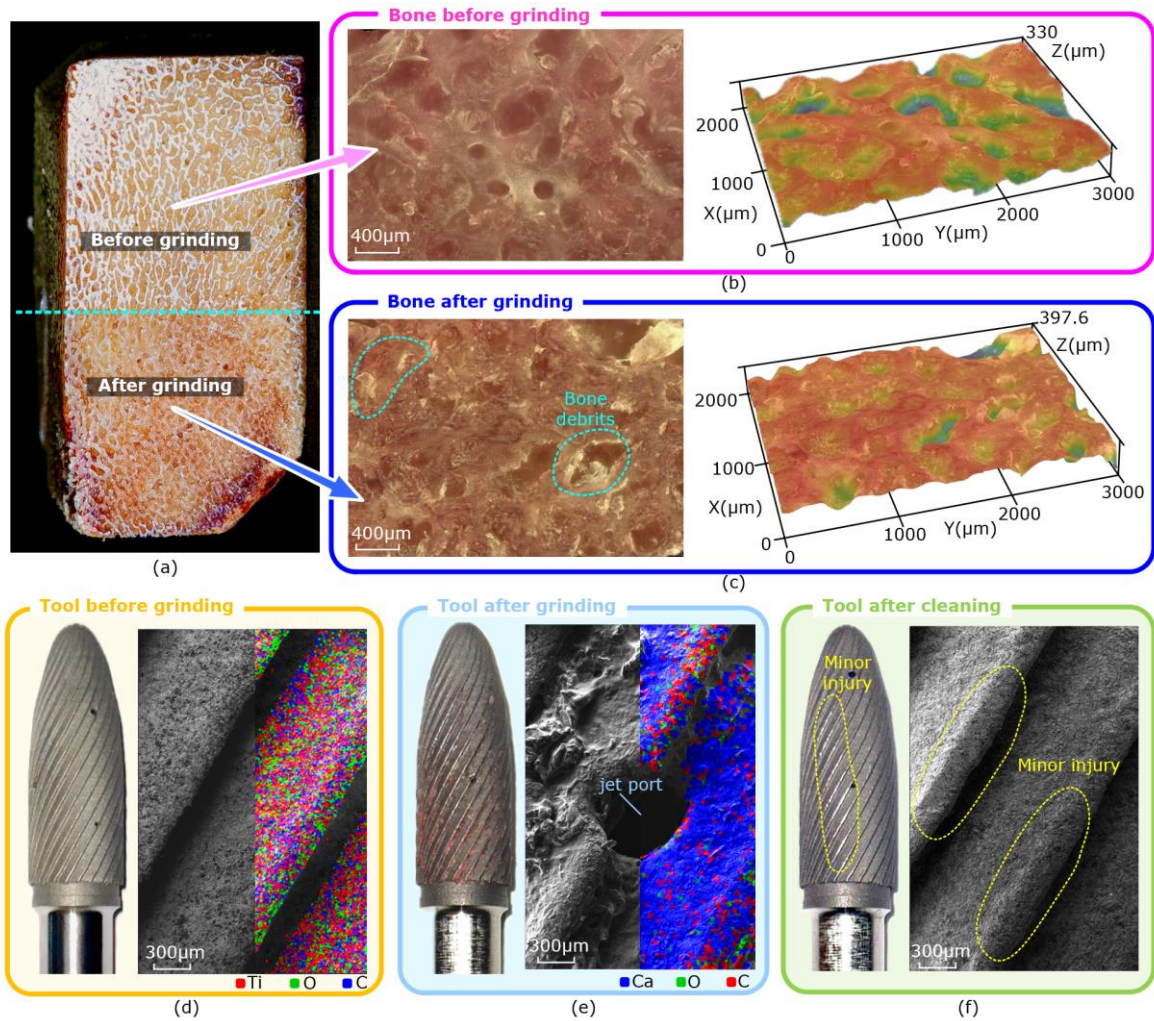


Figure 4-10: Comparison of the surface texture for the bone and tool before and after grinding: (a)bone sample in grinding test; 2D and 3D morphology of the real bone (b) before grinding and (c) after grinding; real picture, microscopic images and EDS of proposed grinding tool (d) before and (e) after grinding and (f) after cleaning.



## Chapter 5 Multifunctional ceramic tool

### 5.1 Introduction and motivation

ONFH is a common and challenging condition in orthopedics. With the extension of ONFH duration, osteocyte apoptosis and trabecular bone loss can decrease the femoral head's load-bearing capacity, leading to the collapse of the articular cartilage and subchondral bone [107]. The most prevalent approach for averting ONFH is core decompression surgery, which can considerably relieve intraosseous hypertension and pain [108, 109]. However, this surgical program is an interventional treatment in the middle and late stages of ONFH. In addition, core decompression needs a large number of surgical tools such as guide wires, surgical drills, cannulated reamers, and curettes [110]. Such complex surgical procedures are not only troublesome, but also expensive and have a high failure rate (20%-40%). Therefore, the integration of multiple complex tools (at least including drilling, implantation, tapping, and drug delivery) into a multifunctional tool would be beneficial for both patients and surgeons to shorten the operating time and minimize potential complications [107].

In this chapter, we design the new kind of multifunctional ceramic tool to achieve early intervention for ONFH, shorten surgical procedures, and minimize surgical incision. The proposed tool has multiple functions including: (i) perform as a bone drilling tool, (ii) load and deliver medicinal substances, and (iii) retain

## Chapter 5 Multifunctional ceramic tool

itself in the drilled hole as a bone scaffold. In the concept design (Section 5.2, Figure 5-1a), biological pore structures similar to bone tissue are introduced to the tool body to improve its compatibility with surrounding cells. In the fabrication (Section 5.3.1, Figure 5-1b), additive manufacturing technique based on nanoparticle jetting is used. To evaluate the tool, mechanical performance (Section 5.3.2), drug releasing ability (Section 5.4, Figure 5-1c), bone drilling performance (Section 5.5, Figure 5-1d), and implantation capability in terms of cell adhesion and growth (Section 5.6, Figure 5-1e) are tested in detail.

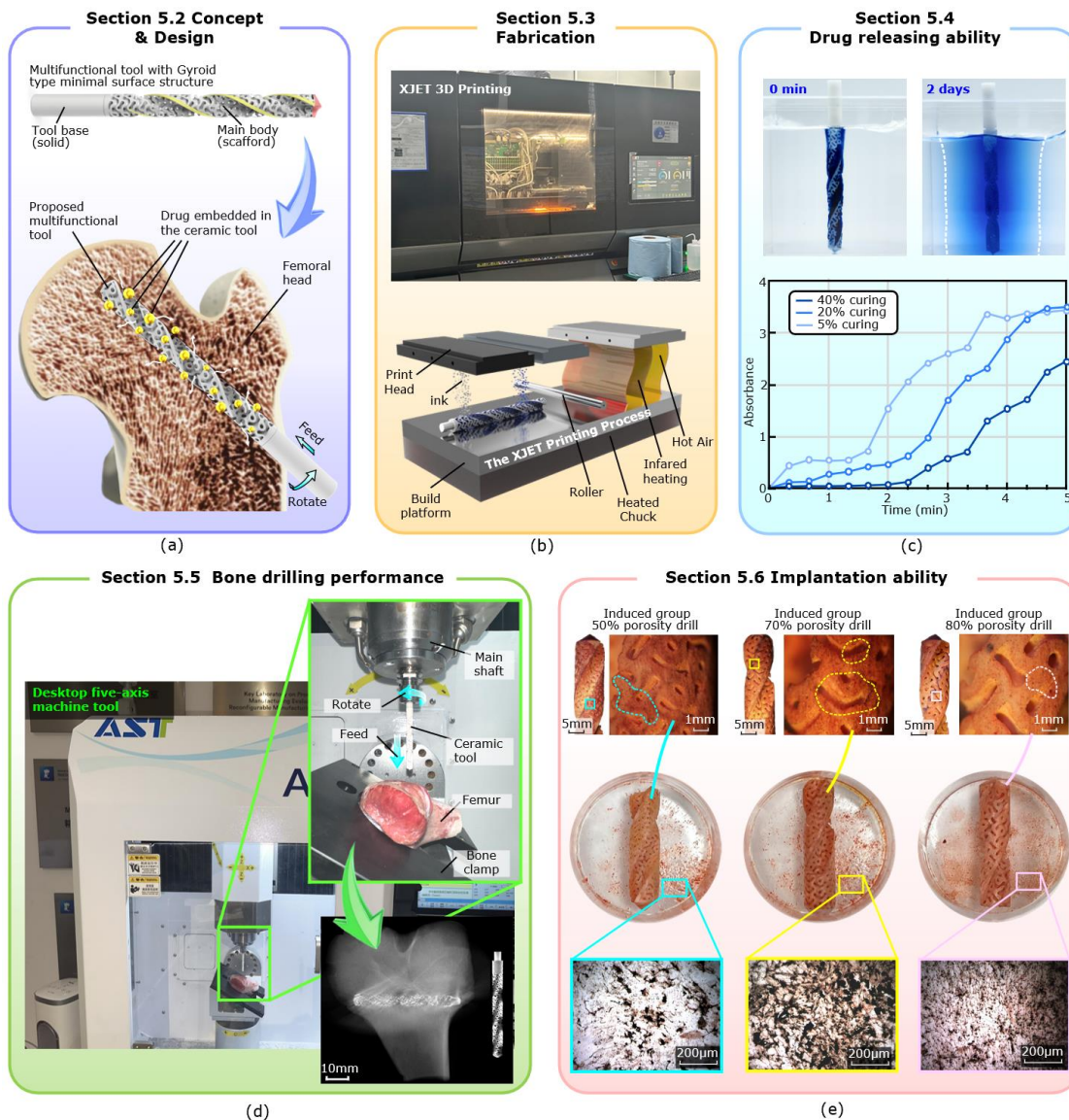


Figure 5-1: the methodology that we followed to design, fabricate and verify our proposed multifunctional ceramic tool: (a) concept and design of proposed multifunctional ceramic tool, (b) fabrication of designed ceramic tool; verification of the multifunctional ceramic tool in (c) drug releasing ability, (d) bone drilling ability, and (e) implantation ability.

## 5.2 Multifunctional ceramic tool concept and design

### 5.2.1 Concept

The tool concept presented is the completely redesigned zirconia ceramic tool (Figure 5-2a) that maintains the self-retention benefits of traditional clinical treatments. This feature enables early intervention before the femoral head undergoes complete necrosis (Figure 5-2b). The zirconia ceramic tool is also designed with a drug-loaded coating that can be cured in advance and released in vivo, delivering therapeutic effects within the body (Figure 5-2c).

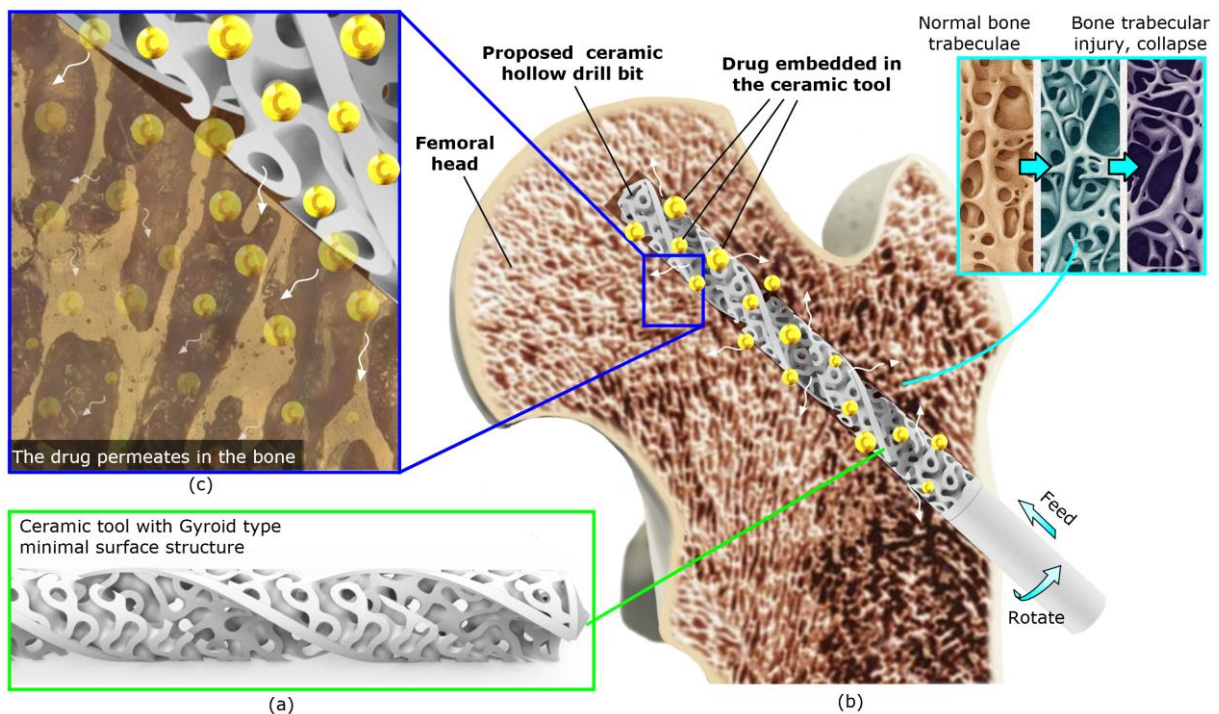


Figure 5-2: Conceptual diagram of (a) proposed ceramic tool; schematic diagram of (b) early treatment of femoral head necrosis and (c) drug permeates in bone.

### 5.2.2 Structural design

The proposal tool concept can be understood from (i) the main tool body, (ii) the cutting edges, and (iii) the detachable structure.

#### **(i) The main body of the ceramic tool**

The designed ceramic tool, as depicted in (Figure 5-3), incorporates a Gyroid type minimal surface structure. This porous design not only possesses exceptional mathematical properties such as low density, stable and uniform load distribution under stress [111, 112], but also offers an ideal environment for cell activity. This micro-porous structure is similar to the structure found in human tissues and organs, such as the bone framework [113], making it suitable for addressing conditions such as trabecular collapse. Additionally, the Gyroid type minimal surface structure features a large specific surface area and a continuous surface characterized by zero mean curvature, which enhances cell adhesion and growth [114]. The pores of the scaffold can also be used to accommodate therapeutic drugs for the treatment of trabecular collapse after the femoral drilling operation. The tool's geometry features a diameter of 5mm, a length of 63mm, and a porosity of 50%. The hollow tool model is developed using Rhino and the Grasshopper plug-in (version 7.20.22193), alongside ANSYS Fluent 2023 R1, before being exported to an STL file.

#### **(ii) the cutting edges of the ceramic tool**

The cutting section of the ceramic tool is composed of two solid regions: the drill front cutter face (Figure 5-3, red area) and the cutting edge (Figure 5-3, yellow area). These regions utilize a solid structure rather than a scaffold design to ensure greater strength and resistance to pressure, as they constitute the primary cutting components of the tool.

### **(iii) The detachable structure of the ceramic tool**

The ceramic tool is designed to be detachable, allowing it to remain in the bone after surgery and act as a scaffold for recovery. The tool base retains a solid structure to withstand the significant torque and compression forces encountered during drilling. To ensure secure attachment during the procedure, the one-way quick-change coupler (see Figure 5-3d) is employed. This design prevents the connection point from disengaging during drilling and allows for easy removal afterward. The coupler only permits counterclockwise rotation, enabling the tool base to be removed once the bit is fully embedded in the bone.

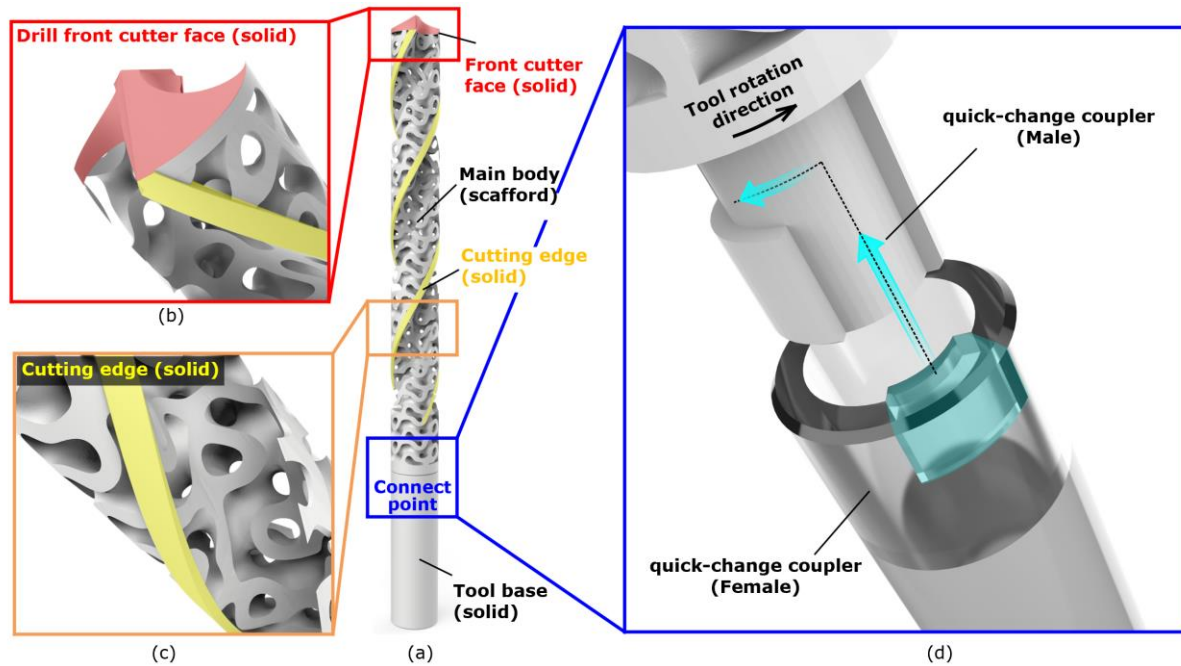


Figure 5-3: A schematic of the (a) proposed ceramic tool having: (b) solid front cutter face, (c) solid cutting edge and (d) quick-change coupler connection point.

### 5.3 The Fabrication and the geometrical/mechanical evaluation

#### 5.3.1 Fabrication route

The designed Gyroid scaffold ceramic tool was horizontally printed (Figure 5-4a, b). The STL model was sliced for fabrication (Figure 5-4c). The entire ceramic tool was fabricated using an NPJ 3D Printer (XJET, Carmel 1400C, Israel, as shown in Figure 5-4d). The printing process is schematically depicted in Figure 5-4e. The system utilized a liquid containing nano-scale ceramic powder, which was sprayed onto a heated substrate at 180°C. This method allowed for the volatilization of excess organic solvents in the inks, effectively bonding the remaining nanoparticles. The NPJ 3D printer had ultra-high resolution (1200 DPI, 20 μm), ultra-thin layer thickness (10.5 μm), and ultra-high accuracy (±25 μm)

facilitating the creation of highly detailed prints. Nanoparticle based structural and support inks were co-printed to form 3D structures and both inks were provided by XJET. A shrinkage factor of 17.8% was incorporated into the design to accommodate shrinkage during the sintering process [86]. After printing, the structure was removed from the printing stage, and the co-printed water-soluble support was dissolved. The sample was sintered in a programmable furnace (FMJ-19/17, FaceRom, China). The sintering process involved heating the part to 1450°C, maintaining this temperature for 180 minutes, and then allowing it to cool to room temperature.

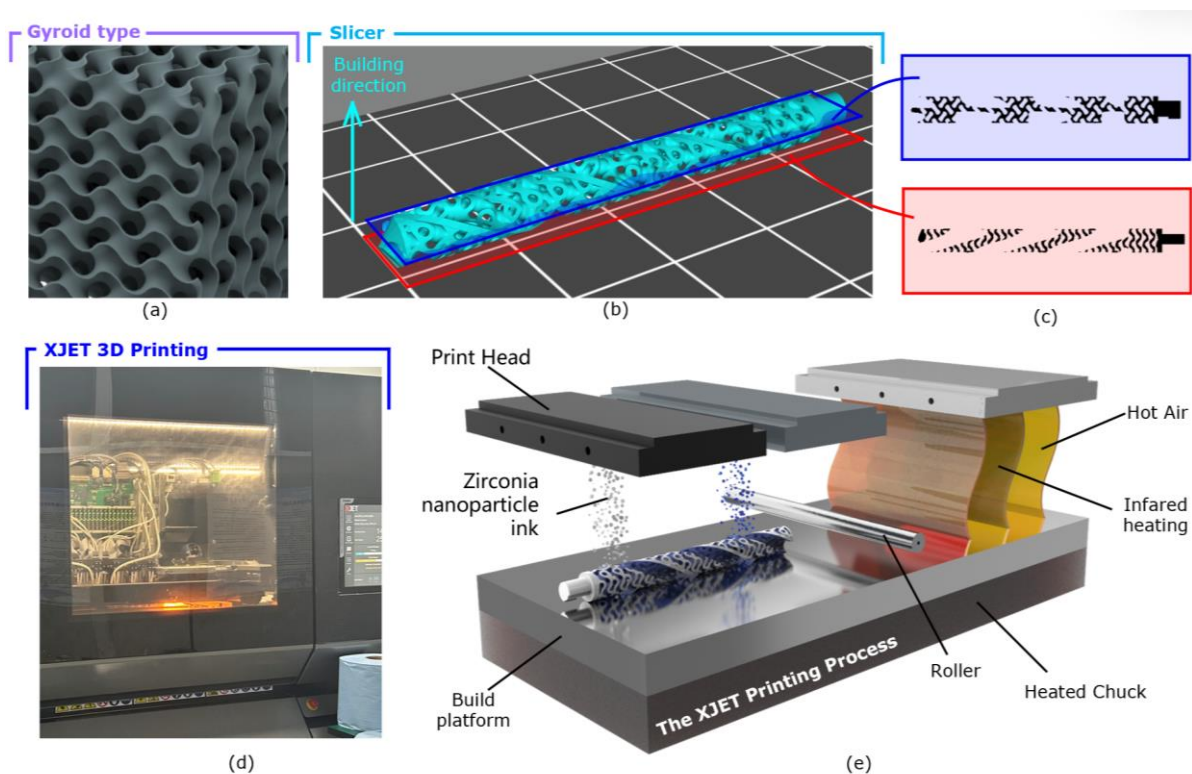


Figure 5-4: Design and Fabrication flow diagram: (a) Gyroid Triply Periodic Minimal Surface (Gyroid TPMS); (b) slicing process and (c) slice shape of each layer; (d) XJET ceramic 3D printing process and (e) XJET printing principle.

### 5.3.2 Geometrical and mechanical evaluation

Figure 5-5b reveals the presence of droplets and streamlined microstructures on the edge surface of the XJET 3D printed ceramic tool (Figure 5-5c). The droplets resulted from the aggregation of ceramic nanoparticle inks during the printing process, while the streamlined microstructure arose from the removal of co-printed water-soluble supports during material ejection [115]. It is important to note that these micro/nanostructures, with their inherent roughness, can significantly influence cell adhesion and mechanical interaction [116, 117]. Figure 5-5d shows that the printed blade angle was  $89.78^\circ$ , reflecting only 0.2% error from the designed model. Furthermore, the edge tips were observed to be sharp, with a nose radius of  $16.8 \mu\text{m}$ , indicating the potential for effective cutting performance of the ceramic tool. As illustrated in Figure 5-5f, the inner solid region of the ceramic tool was observed to be compact with no gaps [118].

The mechanical performance of the printed ceramic tool serves as a crucial indicator. The ultimate strengths of the ceramic tools with 50%, 70%, and 80% porosities were measured at 451.82 MPa, 638.37 MPa, and 721.06 MPa, respectively. Notably, the ultimate strength of the ceramic tool with 80% porosity was 3.6 times higher than that of cortical bone (the hardest bone tissue) [90], and 45 times higher than that of the trabecular bones [91, 106]. These results confirm that the proposed ceramic tool was sufficiently robust for bone drilling.

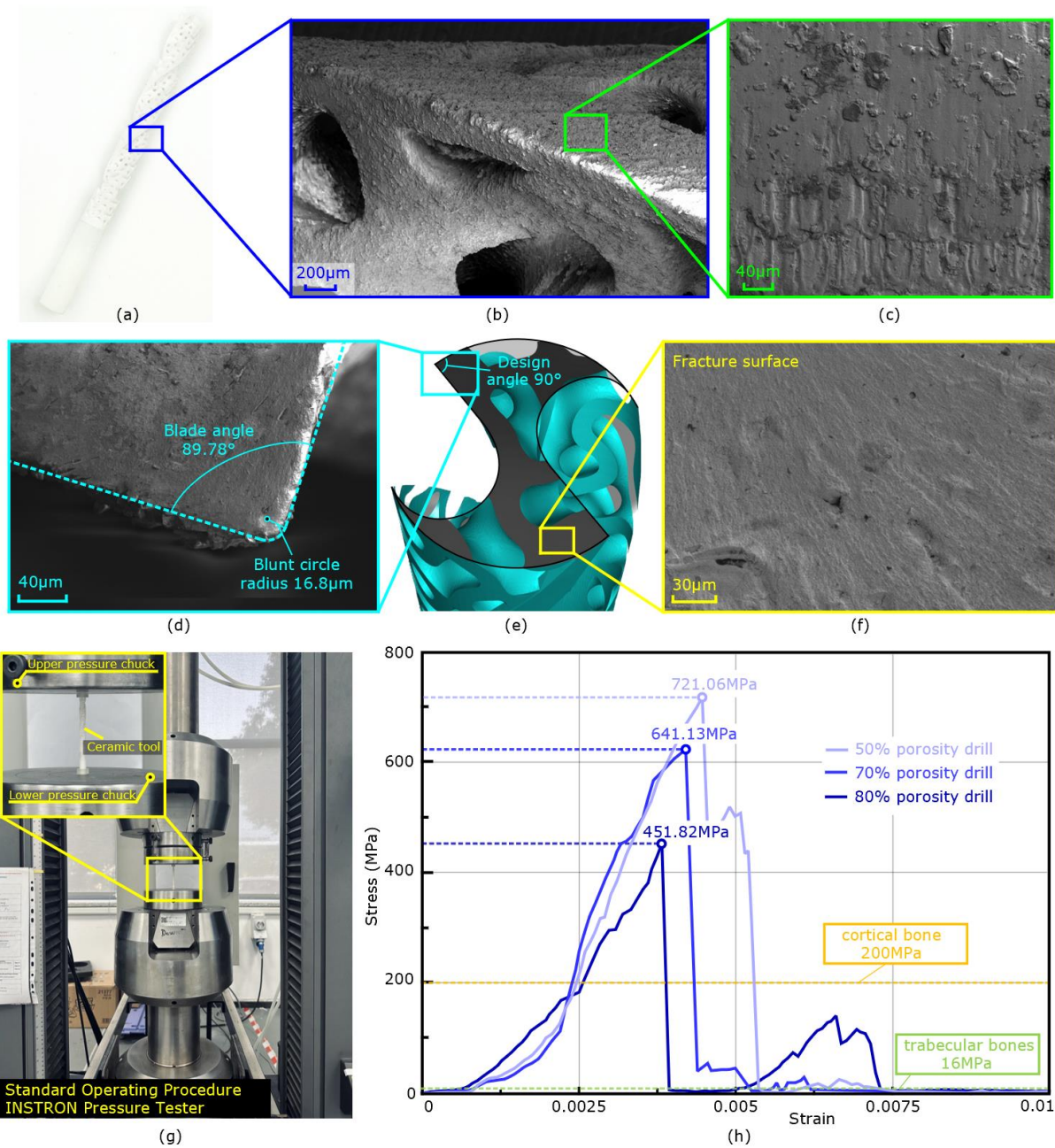


Figure 5-5: Evaluation of the printed ceramic tool: (a) sample picture and (b-c) SEM morphological images of 3D printed tools; (d) cross-section cutting edge accuracy evaluation, (e) tool model and (f) SEM morphological images of fracture surface; (g) tensile test set up and (h) obtained stress-strain curve via different porosity of tool.

### 5.4 Drug releasing ability

The evaluation of the drug release capability of the proposed ceramic tool was conducted from two perspectives: (i) a qualitative drug release experiment and (ii) a quantitative drug release experiment.

#### 5.4.1 Qualitative drug diffusion experiment

##### (i) Method

To evaluate whether the multifunctional ceramic tool could effectively release drugs, a qualitative drug release experiment was conducted to compare drug diffusion with various concentrations of coating excipients. It was worth noting that, because the vitamin C was colorless, blue soluble color powder (JIEYA) was used instead of drugs in the qualitative drug diffusion experiment (Section 5.4.1), to demonstrate the diffusion process in a transparent hydrolyzed micro-gel environment. However, in the further quantitative drug diffusion experiment (Section 5.4.2) and the implantation ability assessment (Section 5.6), vitamin C drug was coated and subjected to spectroscopic testing. 5%, 20% and 40% (w/v) excipient (8000PEG, Sinopharm Chemical Reagent Co., Ltd.) were separately added to the ultrapure water to make three groups of coating solutions, and they all contain 25% w/v colorant. The printed zirconia ceramic tool was dipped into the prepared solution for coating ensuring that 50mg solid content were achieved. A transparent soft gel medium was used to simulate the moist environment in the bones. To prepare this, 0.2% (w/v) Carbopol ETD 2020

polymer (Lubrizol Co.) was suspended in ultrapure water (18.2 megohms-cm) together with 0.01 N NaOH. Each set of tools were inserted into a transparent gel medium, and the diffusion effect of different curing agent content at different time points were observed.

## **(ii) Results and discussion**

The drug release behavior with varying excipient loadings was compared (see Figure 5-6a). In the hydrolyzed micro-gel environment, which simulated the internal bone conditions, it was observed that the drug coated in the ceramic tool holes was released slowly. Notably, for the same drug loading, a higher concentration of excipient resulted in a slower drug release rate. This sustained release of the active ingredient can enhance therapeutic efficacy and minimize side effects [119]. The loaded ingredient achieved uniform and stable distribution in the humid environment. This demonstrated that, in actual bone surgery, the drug could gradually diffuse throughout the femur via trabecular pores, thereby facilitating bone regeneration.

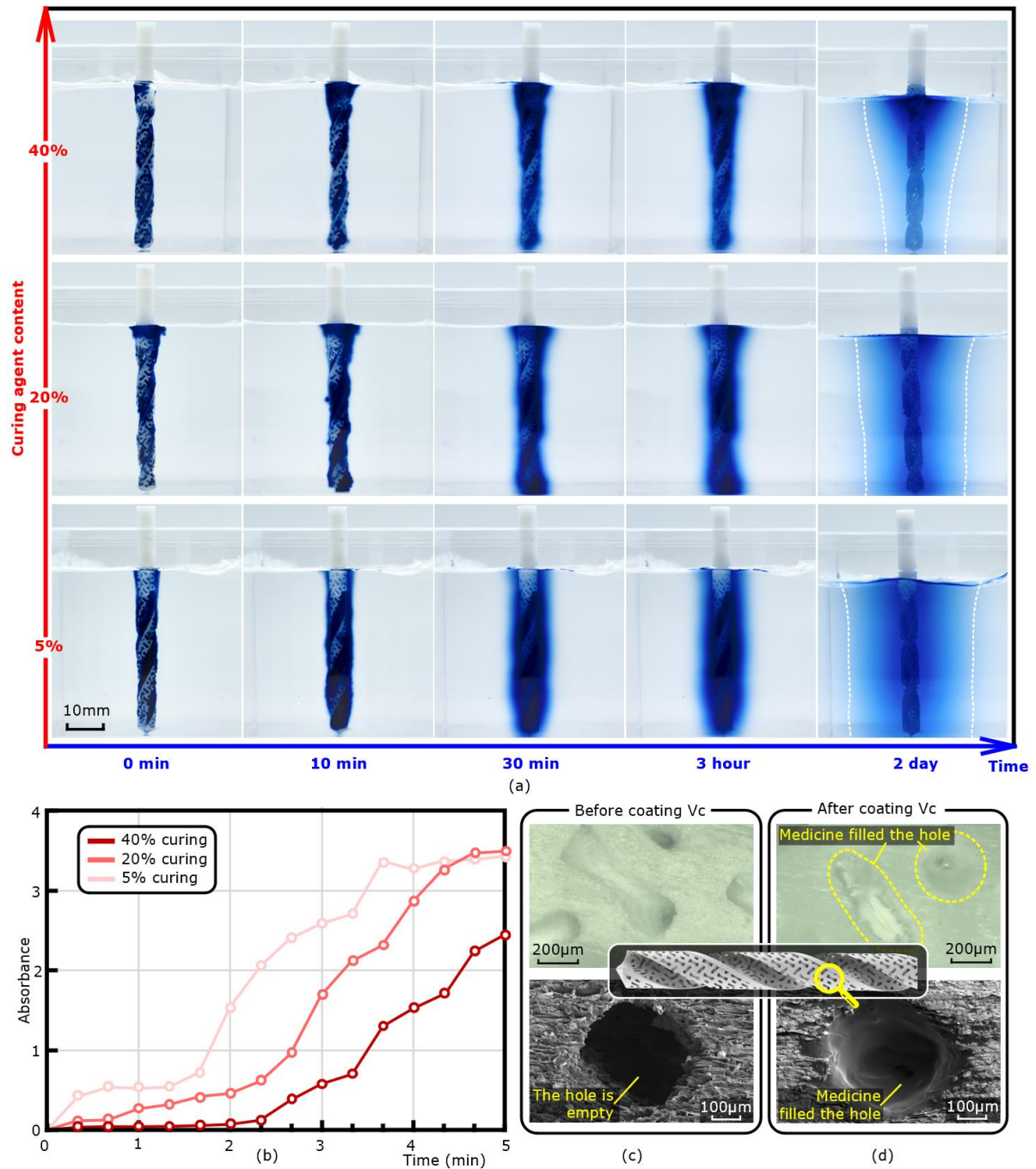


Figure 5-6: Drug release properties: (a) Diffusion time chart of different excipient content (blue soluble color powder instead of drug); (b) Diffusion quantification analysis curve (Vitamin C); Optical microscope and SEM images of zirconia tool (c) before and (d) after dip coating process.

### 5.4.2 Quantitative drug diffusion experiment

The qualitative experimental results demonstrated that the drug could exhibit a sustained release effect in a simulated bone environment. Consequently, the quantitative drug diffusion experiment was conducted to compare the impact of different excipient concentrations on the drug diffusion rate.

### **(i) Method**

The concentration of Vitamin C was maintained at 25% (w/v). Excipient (8000PEG, Shanghai Sinopod Chemical Reagent Co., Ltd.) was added to Vitamin C (SINOPHARM, AR25g 99.7%) solution, creating three different solutions with excipient concentrations of 5%, 20%, and 40% (w/v). The ceramic tools were immersed in these coating solutions to ensure a drug loading of 50 mg. Following this, the ceramic tool holes with varying excipient concentrations were placed in 150 ml of distilled water. Every 20 seconds for a total of 5 minutes, solutions were extracted, resulting in 15\*3 solution samples. These samples were sequentially transferred into colorimetric cups, which were then covered and analyzed using a Thermo Scientific™ Evolution™ 201 Spectrophotometer. The absorbance values of Vitamin C at a wavelength of 245 nm were measured at different time intervals.

### **(ii) Results and discussion**

Figure 5-6b illustrates the light absorption curves of Vitamin C at a wavelength of 245 nm [120] over different diffusion times, with varying excipient concentrations. It can be clearly observed that the three different excipient

content curves also showed an upward trend. As the drug diffusion time increased, the concentration of Vitamin C in the extracted solutions progressively rose, leading to higher light absorption values. Moreover, the curves indicated that lower excipient concentrations resulted in faster drug release. Specifically, with 5% excipient content, light absorption stabilized at approximately  $A=340 \text{ L} \cdot \text{mol}^{-1} \cdot \text{cm}^{-1}$  after 3 minutes and 40 seconds, suggesting that the drug approached complete diffusion at this point. Conversely, with 40% excipient content, the drug began to diffuse after about 3 minutes but had not fully dispersed even after 5 minutes. Microscope image clearly record the tool before and after dip coating process (see Figure 5-6 c, d). These images confirmed that the drug was effectively coated within the tool holes, adhering tightly to the ceramic body, regardless of the hole shape (circular or elongated). Additionally, the ceramic tool with the drug-loaded coating retained its rough surface texture, which facilitated cell adhesion and growth.

### 5.5 Bone drilling performance ability

The experimental setup for drilling trials on real bone is depicted in Figure 5-7a and b. In the evaluation trials of processing (drilling) performances, zirconia ceramic tool with the porosity of 80% was used. This is because the tool with 80% porosity has the worse strength in comparison with that of the other two tools separately with 70% and 50% porosities. If the tool having 80% porosity performs well in the drilling tests, the other two tools' performances can

probably satisfy the processing requirements. The ceramic tool was clamped to the spindle spring clamp of a desktop five-axis machine tool (Ausstattung Company, A5xis). The bone sample was secured onto the bone clamp with screws and plywood. The ceramic tool was fed along the Z-axis at a rate of 2 mm/min and rotated counterclockwise at 2,000 rpm [121] until the main body of the tool was fully embedded in the bones [122].

From Figure 5-7c and d, the printed ceramic tool was successfully drilled into the bone [123]. The CT scan revealed that the tool fit well within the bone, and there was no breakage during the operation. As shown in Figure 5-7d, the majority of the bone fragments were retained and remained in close contact with the grooves and voids of the tool. These fragments were not removed but remained in the bone defect along with the ceramic tool. This incorporation of autogenous bone fragments could facilitate accelerated bone healing and resorption [124].

The pork femur was sectioned along the axis of the drilled hole to examine its rounded surface (see Figure 5-7e). From Figure 5-7f, the trabecular structure in the drilled regions remained visible (indicated by the blue dashed line). These trabecular voids facilitated the entry and absorption of the drug. Vitamin C was able to diffuse throughout the femur via these trabecular voids, aiding in the treatment and metabolism of the diseased bone.

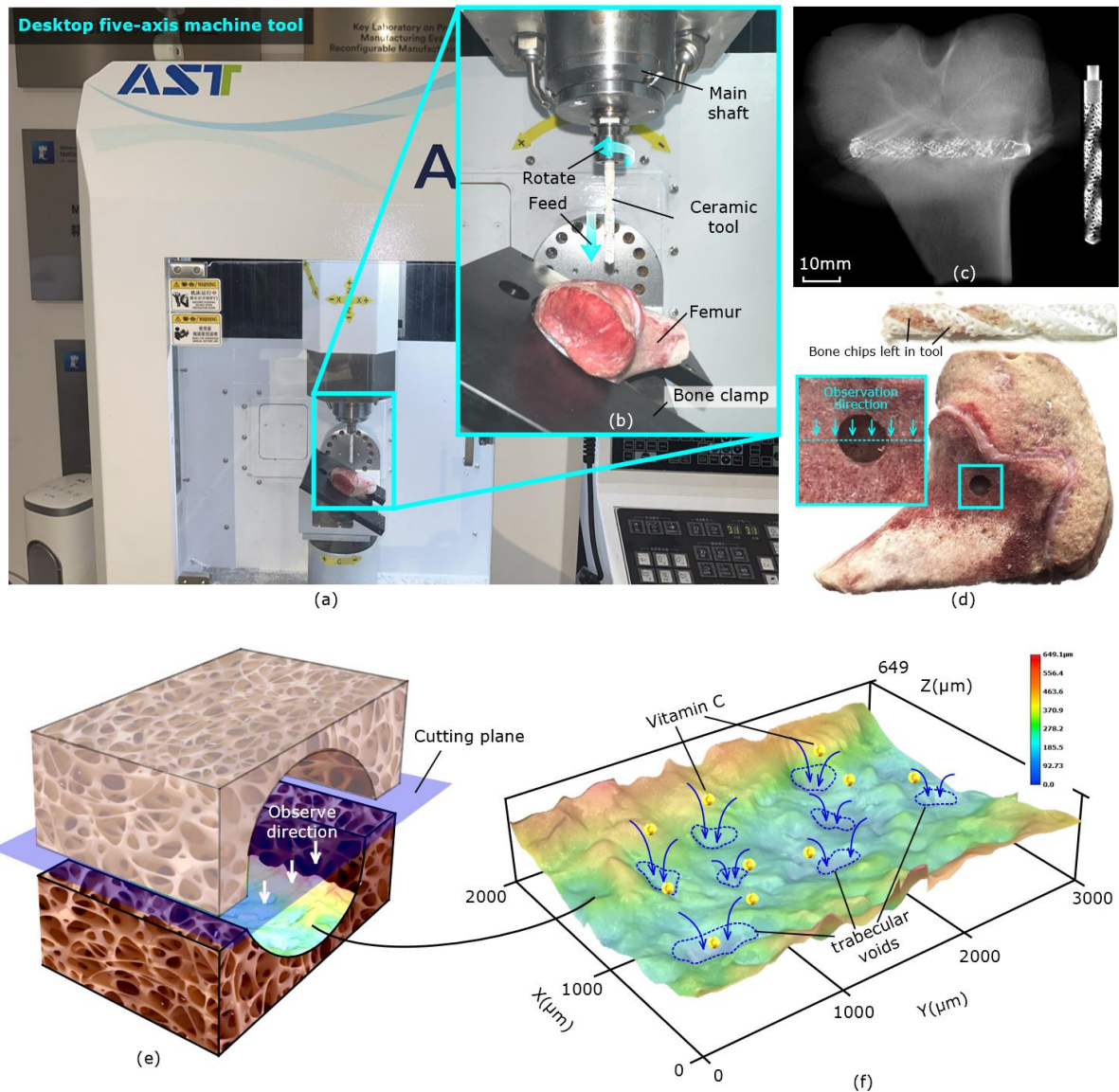


Figure 5-7: Real bone drilling assessment: (a) Global and (b) detailed images of the experiment setup for real bone drilling; (c) CT scan image and (d) sample image of the drilled bone; (e) Schematic diagram and (f) 3D morphology of drilled hole.

The surface morphology of the zirconia ceramic tool with 80% porosity before and after drilling into the bone were compared in Figure 5-8a and c. A large amount of bone fragments remained contained within the tool hole, and the tool surface was also adhered to by the drill fragments. This outcome was

favorable since the bone fragments adhering to the tool could serve as an implant of autogenous bone, thereby minimizing the risk of disease transmission or the rejection of allogeneic bone. The tool surface element X-ray map (Figure 5-8a, b) revealed that the unused tool predominantly exhibited two elements: zirconium (48.55%) and oxygen (40.56%). It might be because the ceramic tool material proposed and prepared in this study was zirconia. Additionally, a minor amount of carbon was detected, comprising only 10.89%, likely originating from residual contaminants. In contrast, the three most abundant elements found on the tool that drilled into the bone were carbon (44.08%), oxygen (27.60%), and calcium (13.94%) (Figure 5-8c, d). This was likely due to the fact that calcium carbonate was the primary constituent of the bone chips that adhered to both the tool surface and within the holes. A small proportion of phosphorus (9.89%) was also identified, which was another trace element present in bones. As a result of the bone covering the tool surface, the proportion of zirconia detected significantly diminished from 48.55% to 4.49%.

To assess the wear behaviors of the cutting edges, drilling trials were conducted using three zirconia ceramic tools with porosities of 50%, 70%, and 80%, respectively (see Figure 5-8e, f, and g). Distinct worn marks were clear after drilling, with the nose radius of the edge tips increasing from 16.8  $\mu\text{m}$  to 38.89  $\mu\text{m}$  for the tool with 80% porosity (see Figure 5-8e), reaching 40.82  $\mu\text{m}$  for the tool with 70% porosity (see Figure 5-8f), and increasing further to 42.42  $\mu\text{m}$  for the tool with 50% porosity (see Figure 5-8g). Notably, the tool with 50% porosity

## Chapter 5 Multifunctional ceramic tool

exhibited the most pronounced wear behavior, likely due to more aggressive friction during the drilling process. This might be because the tool with 50% porosity possessed greater stiffness resulting from its higher structural density. As mentioned above, the ceramic tool will stay and act as a bone scaffold for local repairing after drilling, and the observed levels of edge wearing shall not influence its performance as a scaffold implant.

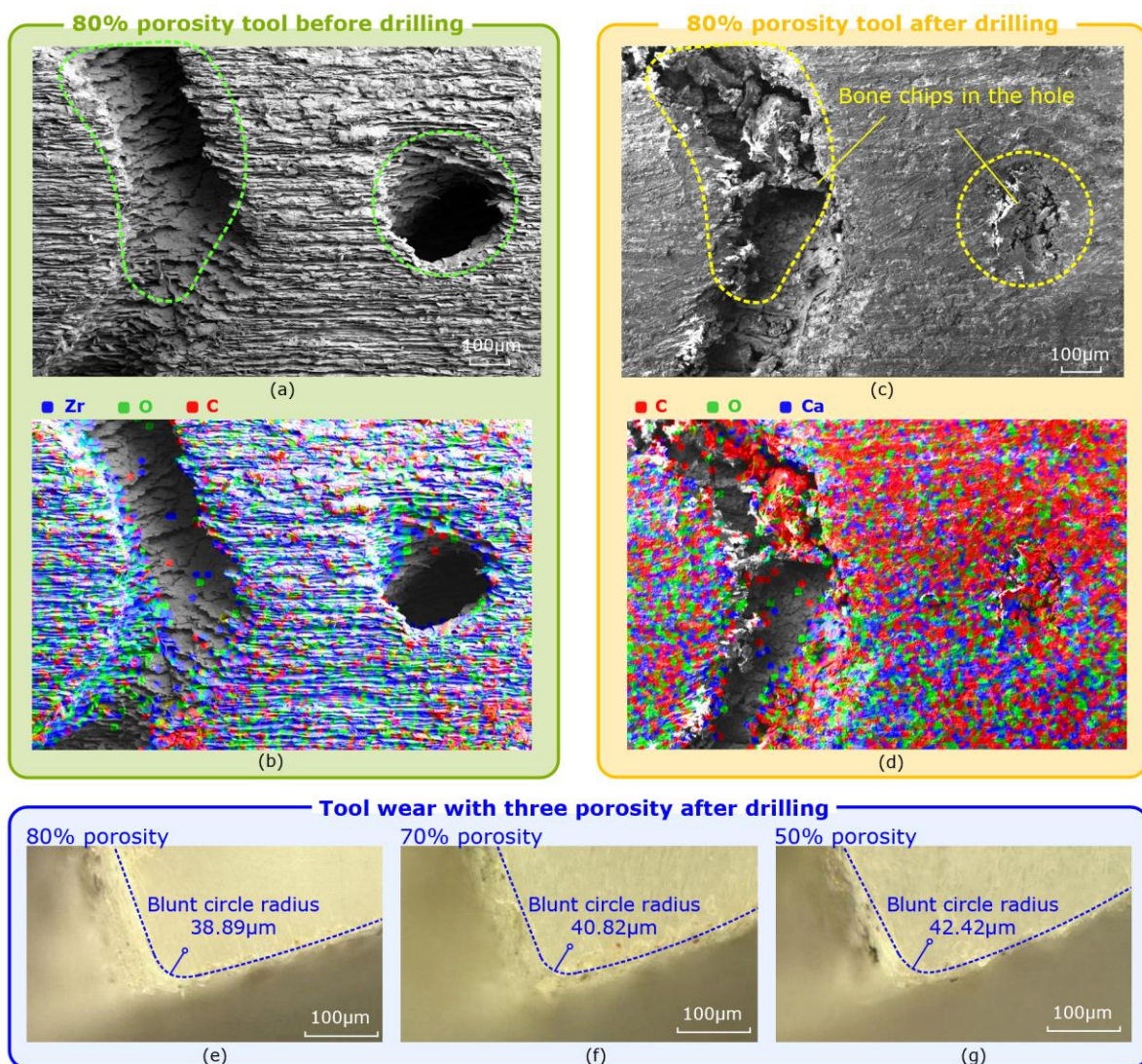


Figure 5-8: Tool surface morphology comparison of the zirconia ceramic tool with 80% porosity before and after drilling: (a) SEM image and (b) EDS mapping of zirconia ceramic tool with 80% porosity before drilling; (c) SEM image and (d) EDS mapping of zirconia ceramic tool

with 80% porosity after drilling. Tool wear comparison of the zirconia ceramic tool with 80%, 70% and 50% porosity after drilling: Optical microscope image of cutting blade of the drilled zirconia ceramic tool with (e) 80%, (f) 70% and (g) 50% porosity

## 5.6 Implantation ability through osteoblast induction assessment

### 5.6.1 Method

To assess the applicability of the proposed drug-loaded ceramic tool in the medical orthopedics field, a series of comparative experiments were conducted to evaluate the growth and adhesion of osteoblasts on the ceramic tools with different porosities. Ceramic tools with porosities of 50%, 70%, and 80% were sterilized for 30 minutes using UV light at a wavelength of 253.7 nm, with each tool incorporating 4.5  $\mu\text{g}$  of vitamin C, as previously detailed. Murine osteoblast precursor cells (MC3T3-E1) were cultured in  $\alpha$ -MEM (GIBCO, C12571500BT) complete medium, which consisted of 10% fetal bovine serum (FBS) and 1% penicillin-streptomycin, within a 5% CO<sub>2</sub> incubator at 37°C. At the logarithmic growth stage,  $3 \times 10^3$  MC3T3-E1 cells were seeded into 12-well plates. The experimental setup included a positive control group (without drug-loaded tools) and three test groups: 50% porosity (G1), 70% porosity (G2), and 80% porosity (G3). Cells were monitored daily, with the medium being replaced every 2 days until day 21. Calcium ion deposition was observed microscopically, and the cells were stained with Alizarin Red S solution (Beyotime Biotechnology, ST1078). The positive control group was maintained in  $\alpha$ -MEM complete medium supplemented with 10 mM  $\beta$ -glycerophosphate (Shanghai Yuanye Bio-

Technology, S27785-5g), 200  $\mu$ M ascorbic acid (Beyotime Biotechnology, ST1434), and 100 nM dexamethasone (Beyotime Biotechnology, ST1254). For the G1, G2, and G3 groups, the culture conditions were the same as the positive control, with the addition of drug-loaded ceramic tools of different porosities.

After 21 days, the four groups of samples were stained using Alizarin Red S solution. The samples were initially washed twice with phosphate-buffered solution (PBS) (Biosciences, C3580-0500) and fixed in 4% paraformaldehyde (Biosharp, BL539A) for 10 minutes. Following fixation, the samples were washed three times with PBS and stained with Alizarin Red S solution at 37°C for 25 minutes. Subsequently, the samples were washed twice with PBS and allowed to air dry in the dark. After drying, imaging was performed using an optical microscope (Leica Microsystems GmbH, Germany) to observe the staining and assess the calcium deposition.

### 5.6.2 Results and discussion

Osteoblasts contribute to bone enhancement and repair by depositing substantial amounts of calcium ions into the bone matrix [125]. Consequently, calcium ion deposition serves as a crucial marker for bone formation. Alizarin Red S stains can interact with calcium ions, imparting a visible red color to the calcium ions, which allows for their observation with the naked eye. The extent of red mineralization is commonly used as an indicator of osteoblast differentiation. Alizarin Red S staining results demonstrated significant red

mineralization in the positive control group under the applied culture conditions (see Figure 5-9a, e), confirming successful osteoblast induction. Upon incorporating the drug-loaded ceramic tool, a notable increase in red mineralization was observed (see Figure 5-9b, c, d), with a corresponding significant rise in calcium ion deposition under microscopic examination (see Figure 5-9f, g, h). This increase was attributed to the enhanced differentiation and proliferation of osteoblasts stimulated by the drug-loaded tool. The cells spread and adhered to the bottom of the culture dish, leading to great calcium ion deposition. Therefore, the drug-loaded ceramic tool effectively promoted osteoblast differentiation and stimulated bone growth.

Furthermore, the observation of calcium ion deposition on the drug-loaded ceramic tool revealed distinct red spots on both the tool surface and within the pores in the osteoblast induction group (see Figure 5-9b, c, d). In contrast, no red deposits were observed on the tool in the uninduced group (see Figure 5-9i). This finding not only confirmed that MC3T3-E1 cells were successfully induced into osteoblasts but also demonstrated that these osteoblasts effectively adhered to the pore walls of the ceramic tool and proliferated on it. Comparing red mineralization across tools with varying porosities, the ceramic tool with 70% porosity exhibited more intense red coloration and greater calcium ion deposition. This might be attributed to the fact that the 70% porosity closely mimics the structure and porosity of trabecular bone (which typically has a porosity of 65%-80%), thereby serving as an optimal scaffold for

## Chapter 5 Multifunctional ceramic tool

bone regeneration. This observation aligns with findings from various studies suggesting that a pore size of 500  $\mu\text{m}$  and a well-distributed, interconnected pore structure best support biological activity and stability, ultimately enhancing bone regeneration [126, 127].

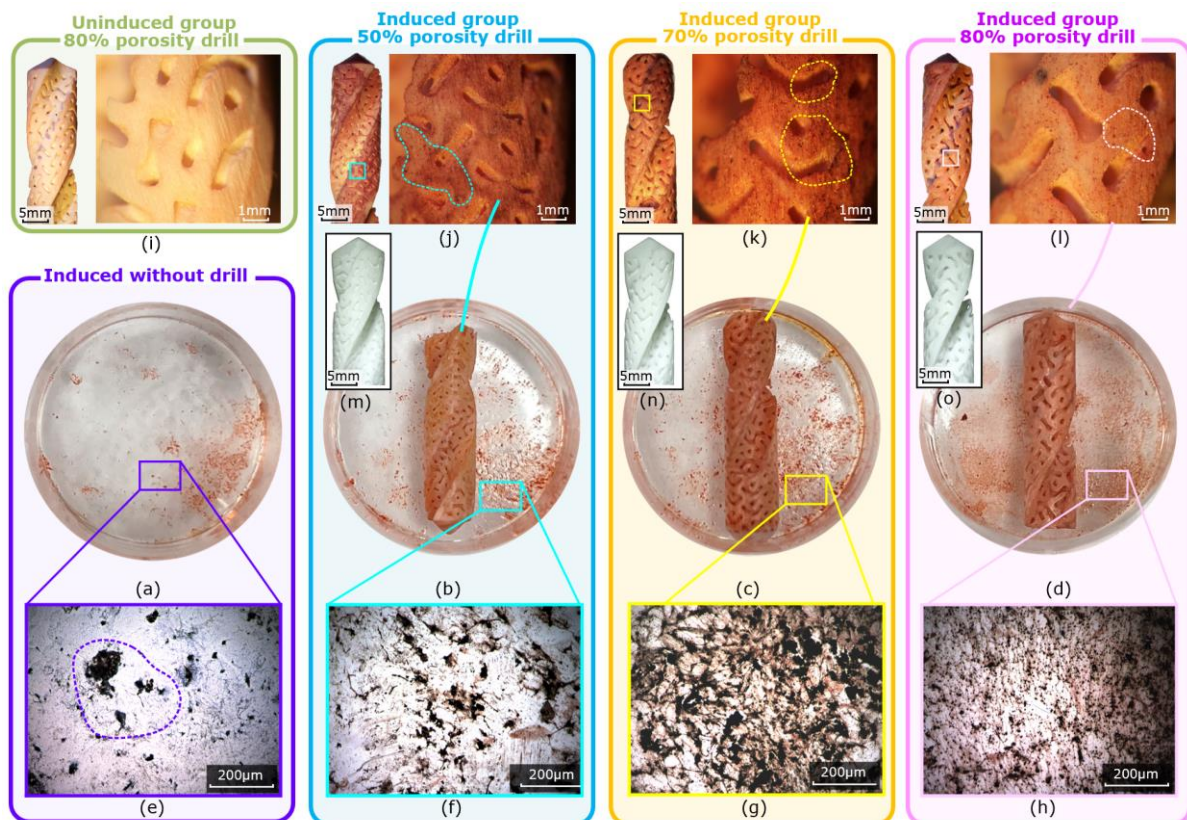


Figure 5-9: Osteoblast experiment designed to prove the efficiency of drug-loaded ceramic tool: (a-d) sample staining figure in POSITIVE CONTROL, G1, G2, and G3 group; (e-h) Microscope figure of calcium ion deposition in POSITIVE CONTROL, G1, G2, and G3 group; (i) Microscope figure of ceramic tool without induced; Microscope figure of ceramic tool in G1, G2, and G3 group (j-l) after stained and (m-o) before stained.

## Chapter 6 Conclusions

This thesis proposed three innovative tool solutions aiming for two typical orthopedic surgeries (craniosynostosis and ONFH) from concept design, tool fabrication based on additive manufacturing, mechanical evaluation, in vitro and in vivo assessments.

### 6.1 Research work summaries

This thesis starts with the pain points in craniosynostosis and ONFH surgeries (Chapter 1). Chapter 2 reviews the current research on cooling strategies to address excessive temperature issue in the grinding area during craniosynostosis surgeries and surgical strategies of specific steps in ONFH surgeries. Additionally, recent research on additively manufactured tools is also reviewed. To fill the research gaps, this research proposes a hollow grinding tool via additive manufacturing that facilitates much more coolant flow onto the tool-bone interface, thereby accelerating heat dissipation in craniosynostosis surgeries (Chapter 3). A closed-loop temperature control grinding device is suggested to address the lack of precise temperature monitoring and regulating in craniosynostosis surgical area (Chapter 4). A multifunctional ceramic tool is proposed to address the complexities of ONFH surgeries and the excessive use of surgical tools, thereby minimizing surgical incisions and potential complications (Chapter 5).

### 6.2 Research findings and outcomes

The main research outcomes of this thesis can be summarized as follow:

This thesis addresses the pain points in craniostyostosis and ONFH surgeries by proposing a series of innovative tool solutions. This research not only fill the gaps in the medical field, but also provides safe and efficient tools for surgical procedures.

#### **(i) Hollow grinding tool**

- The proposed tool enabled 48% of the applied coolant to be delivered to the grinding zone, and the coolant speed was reduced by only 35% when the coolant reached the bone-tool interface. The in vitro and in vivo tests demonstrated that the surgical temperature could be stabilized at 33.3°C and 35.6°C respectively, well below the threshold for bone necrosis (47°C).
- In vitro bone grinding tests revealed the presence of only a few small bone fragments within the trabecular structures when using the proposed tool. In vivo tests revealed minimal apoptotic cells and no edema in the rat brain following skull grinding, confirming that the tool concept effectively preserves tissue viability during surgeries.

#### **(ii) Closed-loop temperature control grinding device**

- The proposed closed-loop grinding device was validated to successfully eject coolant from the designed grinding tool once the predetermined

temperature threshold was reached. The CFD simulation indicated that the coolant achieved the highest flow velocity at the jet port 1 (38 m/s), with the consistent average flow velocity (22.6 m/s) across all four jet ports.

- In the temperature fluctuation experiment, the highest temperature observed in the grinding area was only 36.4°C. The temperature measured by the grinding device was only 0.8°C higher than the actual temperature of the grinding zone, confirming accurate temperature monitoring.

**(iii) multifunctional ceramic tool**

- Drug release tests confirmed that the drug-loaded coating was successfully integrated into the ceramic tool's pores. The drug reached near-complete diffusion in the water environment at approximately 3 minutes and 40 seconds in quantification of diffusion experiment.
- The multifunctional ceramic tool was successfully inserted into the bone without breaking and maintained a stable fit. The ceramic tool with 70% of porosity showed the highest level of osteoblast proliferation and adhesion.

The findings have profound clinical significance and application prospects, advancing surgical techniques and tools, and potentially improving patients' surgery experiences and recovery outcomes.



---

## References

- [1] Chronic musculoskeletal conditions. 2023; Available from: <https://www.aihw.gov.au/reports/chronic-musculoskeletal-conditions/musculoskeletal-conditions/contents/summary>.
- [2] Musculoskeletal health. 2022; Available from: <https://www.who.int/news-room/fact-sheets/detail/musculoskeletal-conditions>.
- [3] J.A. Persing, MOC-PS(SM) CME Article: Management Considerations in the Treatment of Craniosynostosis. *Plastic and Reconstructive Surgery*, 2008. 121(4).
- [4] D. Johnson and A.O. Wilkie, Craniosynostosis. *European Journal of Human Genetics*, 2011. 19(4): p. 369-376.
- [5] D. Kamal, R. TRĂISTARU, D. Alexandru, D. Grecu, and L. Mogoanta, Epidemiologic Study of Avascular Necrosis of the Femoral Head. *Current health sciences journal*, 2013. 39(3).
- [6] S. Chaudhary, V. Garg, D. Mishra, R. Yasam, S. Barik, S.K. Sinha, V. Singh, D. Chaudhary Sr, R.P. Yasam, and S. Sinha, Risk factors for avascular necrosis of the femoral head in pediatric femoral neck fractures. *Cureus*, 2021. 13(7).
- [7] Craniosynostosis. Available from: <https://pediatricimaging.org/diseases/craniosynostosis/>.

## References

---

- [8] Paediatric Craniosynostosis. Available from: <https://store.upsurgeon.com/products/paediatric-craniosynostosis/>.
- [9] S.J. Shin, H.-S. Kwak, T.-J. Cho, M.S. Park, W.J. Yoo, C.Y. Chung, and I.H. Choi, Application of Ganz surgical hip dislocation approach in pediatric hip diseases. *Clinics in Orthopedic Surgery*, 2009. 1(3): p. 132-137.
- [10] M. Michael R Aiello. Avascular Necrosis (AVN) of the Femoral Head Imaging and Diagnosis. Dec 27, 2021.
- [11] M.C.A. Arnold, S. Zhao, R.J. Doyle, J.R.T. Jeffers, and O.R. Boughton, Power-Tool Use in Orthopaedic Surgery: Iatrogenic Injury, Its Detection, and Technological Advances: A Systematic Review. *JBJS Open Access*, 2021. 6(4).
- [12] L. Lin, W. Han, M. Sun, B.S. Kim, X. Chen, Z.M. Aung, Z. Zhang, Y. Zhou, X. Yang, G. Chai, and H. Xu, Current Practices for Esthetic Facial Bone Contouring Surgery in Asians. *Clinics in Plastic Surgery*, 2023. 50(1): p. 71-80.
- [13] H. De Vrind, J. Wondergem, and J. Haveman, Hyperthermia-induced damage to rat sciatic nerve assessed in vivo with functional methods and with electrophysiology. *Journal of neuroscience methods*, 1992. 45(3): p. 165-174.
- [14] S. Singh, B. Hooda, R. Goyal, and P. Taank, A case of Perioperative Visual Loss Following Spine Surgery: Can NIRS monitoring give us a clue? *Medical Journal Armed Forces India*, 2022.

- 
- [15] Y. Shen, M. Drum, and S. Roth, The prevalence of perioperative visual loss in the United States: a 10-year study from 1996 to 2005 of spinal, orthopedic, cardiac, and general surgery. *Anesthesia & Analgesia*, 2009. 109(5): p. 1534-1545.
- [16] O. Salomó-Coll, B. Auriol-Muerza, N. Lozano-Carrascal, F. Hernández-Alfaro, H.-L. Wang, and J. Gargallo-Albiol, Influence of bone density, drill diameter, drilling speed, and irrigation on temperature changes during implant osteotomies: an in vitro study. *Clinical Oral Investigations*, 2021. 25(3): p. 1047-1053.
- [17] G. Augustin, S. Davila, K. Mihoci, T. Udiljak, D.S. Vedrına, and A. Antabak, Thermal osteonecrosis and bone drilling parameters revisited. *Archives of Orthopaedic and Trauma Surgery*, 2008. 128(1): p. 71-77.
- [18] S.A. Gehrke, M.K. Pazetto, S. de Oliveira, S. Corbella, S. Taschieri, and F.E.C. Mardegan, Study of temperature variation in cortical bone during osteotomies with trephine drills. *Clinical Oral Investigations*, 2014. 18(7): p. 1749-1755.
- [19] M. Bakovic, L. Starsiak, S. Bennett, R. McCaffrey, E. Mantilla-Rivas, M. Manrique, G.F. Rogers, and A.K. Oh, Socioeconomic Influence on Surgical Management and Outcomes in Patients with Craniosynostosis-A Systematic Review. *The Cleft Palate Craniofacial Journal*, 2024: p. 10556656241261838.

## References

---

- [20] G.D. Strbac, E. Unger, R. Donner, M. Bijak, G. Watzek, and W. Zechner, Thermal effects of a combined irrigation method during implant site drilling. A standardized in vitro study using a bovine rib model. *Clinical oral implants research*, 2014. 25 6: p. 665-74.
- [21] Y. Hou, C. Li, H. Ma, Y. Zhang, M. Yang, and X. Zhang, An experimental research on bone drilling temperature in orthopaedic surgery. *The Open Materials Science Journal*, 2015. 9(1).
- [22] M. Sasaki, S. Morris, T. Goto, K. Iwatsuki, and T. Yoshimine, Spray-Irrigation System Attached to High-Speed Drills for Simultaneous Prevention of Local Heating and Preservation of a Clear Operative Field in Spinal Surgery. *Neurologia medico-chirurgica*, 2010. 50(10): p. 900-904.
- [23] M. Jamil, A.M. Khan, H. Hegab, M. Mia, and M.K. Gupta, Modeling, multi-objective optimization and cost estimation of bone drilling under micro-cooling spray technique: an integrated analysis. *International Journal on Interactive Design and Manufacturing (IJIDeM)*, 2020. 14(2): p. 435-450.
- [24] I. Barrak, A. Joób-Fancsaly, E. Varga, K. Boa, and J. Piffko, Effect of the Combination of Low-Speed Drilling and Cooled Irrigation Fluid on Intraosseous Heat Generation During Guided Surgical Implant Site Preparation: An In Vitro Study. *Implant Dent*, 2017. 26(4): p. 541-546.
- [25] S. Takenaka, N. Hosono, Y. Mukai, K. Tateishi, and T. Fuji, Significant reduction in the incidence of C5 palsy after cervical laminoplasty using

- chilled irrigation water. *The Bone & Joint Journal*, 2016. 98-B(1): p. 117-124.
- [26] S. Murphy, Does the use of cooled saline irrigation during third molar surgery affect post-operative morbidity? *Evid Based Dent*, 2022. 23(4): p. 142-143.
- [27] A.S. Greenwald, S.D. Boden, V.M. Goldberg, Y. Khan, C.T. Laurencin, and R.N. Rosier, Bone-graft substitutes: facts, fictions, and applications. *Jbjs*, 2001. 83(2): p. S98-103.
- [28] R.J.M.D. Lee and S.C.M.D.P. Mears, Greening of Orthopedic Surgery. *Orthopedics (Online)*, 2012. 35(6): p. e940-4.
- [29] A. Babbar, V. Jain, D. Gupta, D. Agrawal, C. Prakash, S. Singh, L.Y. Wu, H.Y. Zheng, G. Królczyk, and M. Bogdan-Chudy, Experimental analysis of wear and multi-shape burr loading during neurosurgical bone grinding. *Journal of Materials Research and Technology*, 2021. 12: p. 15-28.
- [30] A.J. Shih, B.L. Tai, L. Zhang, S. Sullivan, and S. Malkin, Prediction of bone grinding temperature in skull base neurosurgery. *CIRP annals*, 2012. 61(1): p. 307-310.
- [31] G.G. Luna, D. Axinte, and D. Novovic, Engineered grinding tools reimplemented by precise sharpening: A case study on an ultrahard ceramic matrix composite (CMC). *CIRP Annals*, 2022. 71(1): p. 289-292.

## References

---

- [32] T. Zhou, Y. He, Q. Yu, Z. Liang, S. Li, X. Liu, X. Dong, and X. Wang, Study on electroless composite plating for an NiP bond micro diamond wheel. *Journal of Materials Processing Technology*, 2020. 279: p. 116561.
- [33] G. Augustin, S. Davila, T. Udilljak, T. Staroveski, D. Brezak, and S. Babic, Temperature changes during cortical bone drilling with a newly designed step drill and an internally cooled drill. *Int Orthop*, 2012. 36(7): p. 1449-56.
- [34] K. Gok, L. Buluc, U.S. Muezzinoglu, and Y. Kisioglu, Development of a new driller system to prevent the osteonecrosis in orthopedic surgery applications. *Journal of the Brazilian Society of Mechanical Sciences and Engineering*, 2015. 37(2): p. 549-558.
- [35] A. Babbar, V. Jain, D. Gupta, and D. Agrawal, Finite element simulation and integration of CEM43 °C and Arrhenius Models for ultrasonic-assisted skull bone grinding: A thermal dose model. *Medical Engineering & Physics*, 2021. 90: p. 9-22.
- [36] T. Enomoto, H. Shigeta, T. Sugihara, and U. Satake, A new surgical grinding wheel for suppressing grinding heat generation in bone resection. *CIRP Annals*, 2014. 63(1): p. 305-308.
- [37] T. Mizutani, U. Satake, and T. Enomoto, A study on a cooling method for bone grinding using diamond bur for minimally invasive surgeries. *Precision Engineering*, 2021. 70: p. 155-163.

- 
- [38] D. Zhao, F. Zhang, B. Wang, B. Liu, L. Li, S.-Y. Kim, S.B. Goodman, P. Hernigou, Q. Cui, and W.C. Lineaweaver, Guidelines for clinical diagnosis and treatment of osteonecrosis of the femoral head in adults (2019 version). *Journal of orthopaedic translation*, 2020. 21: p. 100-110.
- [39] D. Yuan, Z. Wu, L. Yang, Q. Zou, D. Hua, Z. Zou, and C. Ye, Biomechanical analysis of the drilling parameters for early osteonecrosis of the femoral head. *Computer Methods and Programs in Biomedicine*, 2022. 219: p. 106737.
- [40] V.D.J. Pellegrini, M.J. Kelly, M.N. Rumi, M. Kothari, K.J. Bailey, W.M. Parrish, and M.A. Parentis, V.D. Pellegrini Jr., M.J. Kelly, M.N. Rumi, M. Kothari, K.J. Bailey, W.M. Parrish, and M.A. Parentis reply. *JBJS*, 2007. 89(11): p. 2551.
- [41] S. Mohanty, K. Singh, R. Kundangar, and V. Shankar, Management of non-traumatic avascular necrosis of the femoral head—a comparative analysis of the outcome of multiple small diameter drilling and core decompression with fibular grafting. *Musculoskeletal surgery*, 2017. 101: p. 59-66.
- [42] A. Al Omran, Multiple drilling compared with standard core decompression for avascular necrosis of the femoral head in sickle cell disease patients. *Archives of orthopaedic and trauma surgery*, 2013. 133: p. 609-613.

## References

---

- [43] S. Kim, D. Kim, I. Park, B. Park, P. Kim, and J. Ihn. Multiple drilling compared with standard core decompression for the treatment of osteonecrosis of the femoral head. in Orthopaedic proceedings. 2004. Bone & Joint.
- [44] F. Alambeigi, Y. Wang, S. Sefati, C. Gao, R.J. Murphy, I. Iordachita, R.H. Taylor, H. Khanuja, and M. Armand, A curved-drilling approach in core decompression of the femoral head osteonecrosis using a continuum manipulator. IEEE Robotics and Automation Letters, 2017. 2(3): p. 1480-1487.
- [45] S.V. Muley, A.N. Vidvans, G.P. Chaudhari, and S. Udainiya, An assessment of ultra fine grained 316L stainless steel for implant applications. Acta Biomaterialia, 2016. 30: p. 408-419.
- [46] J.D. Majumdar, A. Kumar, S. Pityana, and I. Manna, Laser Surface Melting of AISI 316L Stainless Steel for Bio-implant Application. Proceedings of the National Academy of Sciences, India Section A: Physical Sciences, 2018. 88(3): p. 387-403.
- [47] C. Wang, D. Liu, Q. Xie, J. Liu, S. Deng, K. Gong, C. Huang, L. Yin, M. Xie, Z. Guo, and W. Zheng, A 3D Printed Porous Titanium Alloy Rod with Diamond Crystal Lattice for Treatment of the Early-Stage Femoral Head Osteonecrosis in Sheep. Int J Med Sci, 2019. 16(3): p. 486-493.
- [48] C. Wang, Q. Xie, L. Yang, J. Liu, D. Liu, Z. Li, K. Gong, L. Yin, W. Wang, Z. Guo, and W. Zheng, A 3D printed porous titanium alloy rod with biogenic lamellar configuration for treatment of the early-stage femoral head

- osteonecrosis in sheep. *Journal of the Mechanical Behavior of Biomedical Materials*, 2020. 106: p. 103738.
- [49] E. Zhang, L. Xu, G. Yu, F. Pan, and K. Yang, In vivo evaluation of biodegradable magnesium alloy bone implant in the first 6 months implantation. *Journal of Biomedical Materials Research Part A: An Official Journal of The Society for Biomaterials, The Japanese Society for Biomaterials, and The Australian Society for Biomaterials and the Korean Society for Biomaterials*, 2009. 90(3): p. 882-893.
- [50] K. Kumar, R.S. Gill, and U. Batra, Challenges and opportunities for biodegradable magnesium alloy implants. *Materials Technology*, 2018. 33(2): p. 153-172.
- [51] Y. Zhang, T. Lin, H. Meng, X. Wang, H. Peng, G. Liu, S. Wei, Q. Lu, Y. Wang, A. Wang, W. Xu, H. Shao, and J. Peng, 3D gel-printed porous magnesium scaffold coated with dibasic calcium phosphate dihydrate for bone repair in vivo. *Journal of Orthopaedic Translation*, 2022. 33: p. 13-23.
- [52] H. Yu, M. Xu, Q. Duan, Y. Li, Y. Liu, L. Song, L. Cheng, J. Ying, and D. Zhao, 3D-printed porous tantalum artificial bone scaffolds: fabrication, properties, and applications. *Biomedical Materials*, 2024. 19(4): p. 042002.
- [53] Y. Liu, L. Yan, S. Zhou, X. Su, Y. Cao, C. Wang, and S. Liu, Tantalum rod implantation for femoral head osteonecrosis: survivorship analysis and

## References

---

- determination of prognostic factors for total hip arthroplasty. *International Orthopaedics*, 2016. 40(7): p. 1397-1407.
- [54] Z. Liu, W. Guo, Z. Li, L. Cheng, Q. Zhang, D. Yue, Z. Shi, B. Wang, W. Sun, and N. Zhang, Porous tantalum rods for treating osteonecrosis of the femoral head. *Genetics and Molecular Research*, 2014. 13(4): p. 8342-8352.
- [55] B. Liu, W. Sun, D. Yue, Z. Li, and W. Guo, Combined tantalum implant with bone grafting for the treatment of osteonecrosis of the femoral head. *Journal of Investigative Surgery*, 2013. 26(3): p. 158-162.
- [56] C. Park, Y.J. Seong, I.G. Kang, E.H. Song, H. Lee, J. Kim, H.D. Jung, H.E. Kim, and T.S. Jang, Enhanced Osseointegration Ability of Poly(lactic acid) via Tantalum Sputtering-Based Plasma Immersion Ion Implantation. *ACS Appl Mater Interfaces*, 2019. 11(11): p. 10492-10504.
- [57] C. Hwang, S. Park, I.-G. Kang, H.-E. Kim, and C.-M. Han, Tantalum-coated polylactic acid fibrous membranes for guided bone regeneration. *Materials Science and Engineering: C*, 2020. 115: p. 111112.
- [58] D. Pathote, P. Kumari, V. Singh, D. Jaiswal, R.K. Gautam, and C.K. Behera, Biocompatibility evaluation, wettability, and scratch behavior of Ta-coated 316L stainless steel by DC magnetron sputtering for the orthopedic applications. *Surface and Coatings Technology*, 2023. 459: p. 129392.

- [59] D. Pathote, D. Jaiswal, V. Singh, and C.K. Behera, Electrochemical corrosion behavior of tantalum coated 316L stainless steel by D.C. Magnetron sputtering for orthopedic applications. *Applied Surface Science Advances*, 2023. 13: p. 100365.
- [60] X.M. Zhang, Y. Li, Y.X. Gu, C.N. Zhang, H.C. Lai, and J.Y. Shi, Ta-Coated Titanium Surface With Superior Bacteriostasis And Osseointegration. *Int J Nanomedicine*, 2019. 14: p. 8693-8706.
- [61] R. Sarkar and G. Banerjee, Ceramic based bio-medical implants. *Interceram*, 2010. 59(2): p. 98-102.
- [62] Q. Li, W. Liao, G. Fu, J. Liao, R. Zhang, M. Li, Y. Yang, Y. Ma, M. Zheng, and Q. Zheng, Combining autologous bone marrow buffy coat and angioconductive bioceramic rod grafting with advanced core decompression improves short-term outcomes in early avascular necrosis of the femoral head: a prospective, randomized, comparative study. *Stem Cell Research & Therapy*, 2021. 12(1): p. 1-10.
- [63] D. Shtansky, I. Bashkova, P.V. Kiryukhantsev-Korneev, A. Sheveiko, E. Levashov, J. Moore, and N. Gloushankova. Bioactive ceramic tantalum-doped films for implants. in *Doklady. Biochemistry and Biophysics*. 2008. Springer Nature BV.
- [64] N. Donkov, J. Walkowicz, V. Zavaleyev, A. Zykova, V. Safonov, S. Dudin, and S. Yakovin. Mechanical properties of tantalum-based ceramic coatings for

## References

---

- biomedical applications. in *Journal of Physics: Conference Series*. 2018. IOP Publishing.
- [65] B. Rahmati, E. Zalnezhad, A.A.D. Sarhan, Z. Kamiab, B. Nasiri Tabrizi, and W.A.B.W. Abas, Enhancing the adhesion strength of tantalum oxide ceramic thin film coating on biomedical Ti–6Al–4V alloy by thermal surface treatment. *Ceramics International*, 2015. 41(10, Part A): p. 13055-13063.
- [66] D.H. Neustadt, Intra-articular injections for osteoarthritis of the knee. *Cleveland Clinic journal of medicine*, 2006. 73(10): p. 897.
- [67] E. Kon, A. Boffa, L. Andriolo, A. Di Martino, B. Di Matteo, N. Magarelli, M. Marcacci, F. Onorato, N. Trenti, and S. Zaffagnini, Subchondral and intra-articular injections of bone marrow concentrate are a safe and effective treatment for knee osteoarthritis: a prospective, multi-center pilot study. *Knee Surgery, Sports Traumatology, Arthroscopy*, 2021. 29(12): p. 4232-4240.
- [68] P.A. Clark, E.K. Moiola, D.R. Sumner, and J.J. Mao, Porous implants as drug delivery vehicles to augment host tissue integration. *The FASEB Journal*, 2008. 22(6): p. 1684-1693.
- [69] C. Tian, X. Li, S. Zhang, G. Guo, L. Wang, and Y. Rong, Study on design and performance of metal-bonded diamond grinding wheels fabricated by selective laser melting (SLM). *Materials & Design*, 2018. 156: p. 52-61.

- 
- [70] Y. Peng, J. Ren, C. Jia, G. Zhong, Q. Ma, and W. Zhang, Structural design and mechanical properties of porous structured diamond abrasive tool by selective laser melting. *Ceramics International*, 2023. 49(4): p. 6508-6521.
- [71] H. Tian, X. Dang, D. Meng, B. Tian, and J. Li, Influence of drilling parameters on bone drilling force and temperature by FE simulation and parameters optimization based Taguchi method. *Alexandria Engineering Journal*, 2023. 75: p. 115-126.
- [72] B. Denkena, A. Krödel, J. Harmes, F. Kempf, T. Griemsmann, C. Hoff, J. Hermsdorf, and S. Kaierle, Additive manufacturing of metal-bonded grinding tools. *The International Journal of Advanced Manufacturing Technology*, 2020. 107: p. 2387-2395.
- [73] T. Tanaka and Y. Isono, New development of a grinding wheel with resin cured by ultraviolet light. *Journal of materials processing Technology*, 2001. 113(1-3): p. 385-391.
- [74] X. Meng, W. Yang, and X. Deng, Research on 3D printing process and properties of diamond–resin composites based on digital light processing. *Diamond and Related Materials*, 2021. 120: p. 108715.
- [75] Q. Ai, J. Khosravi, B. Azarhoushang, A. Daneshi, and B. Becker, Digital light processing-based additive manufacturing of resin bonded SiC grinding wheels and their grinding performance. *The International Journal of Advanced Manufacturing Technology*, 2022: p. 1-17.

## References

---

- [76] M. Barmouz, B. Azarhoushang, A. Zahedi, F. Rabiei, and F. Steinhäuser, Progress in grinding performance by additive manufacturing of grinding wheels integrated with internal venturi cooling channels and surface slots. *Journal of Manufacturing Processes*, 2023. 99: p. 485-500.
- [77] R. He, W. Liu, Z. Wu, D. An, M. Huang, H. Wu, Q. Jiang, X. Ji, S. Wu, and Z. Xie, Fabrication of complex-shaped zirconia ceramic parts via a DLP-stereolithography-based 3D printing method. *Ceramics international*, 2018. 44(3): p. 3412-3416.
- [78] K. Sandhu, G. Singh, S. Singh, R. Kumar, C. Prakash, S. Ramakrishna, G. Królczyk, and C.I. Pruncu, Surface characteristics of machined polystyrene with 3D printed thermoplastic tool. *Materials*, 2020. 13(12): p. 2729.
- [79] K.D. Traxel and A. Bandyopadhyay, Diamond-reinforced cutting tools using laser-based additive manufacturing. *Additive manufacturing*, 2021. 37: p. 101602.
- [80] K.D. Traxel and A. Bandyopadhyay, First demonstration of additive manufacturing of cutting tools using directed energy deposition system: Stellite™-based cutting tools. *Additive Manufacturing*, 2019. 25: p. 460-468.
- [81] M. Skrzyniarz, L. Nowakowski, and S. Blasiak, Geometry, structure and surface quality of a maraging steel milling cutter printed by direct metal laser melting. *Materials*, 2022. 15(3): p. 773.

- 
- [82] S. Fries, S. Genilke, M.B. Wilms, M. Seimann, A. Weisheit, A. Kaletsch, T. Bergs, J.H. Schleifenbaum, and C. Broeckmann, Laser-based additive manufacturing of WC–Co with high-temperature powder bed preheating. *steel research international*, 2020. 91(3): p. 1900511.
- [83] F. Matos, H. Coelho, O. Emadinia, R. Amaral, T. Silva, N. Gonçalves, J. Marouvo, D. Figueiredo, A. de Jesus, and A. Reis, Additively manufactured milling tools for enhanced efficiency in cutting applications. *Procedia Structural Integrity*, 2024. 53: p. 270-277.
- [84] N. Sugita, T. Osa, and M. Mitsuishi, Analysis and estimation of cutting-temperature distribution during end milling in relation to orthopedic surgery. *Medical Engineering & Physics*, 2009. 31(1): p. 101-107.
- [85] R.V. Muratov, P.N. Ryabov, and S.A. Dyachkov, Dynamic domain decomposition method based on weighted Voronoi diagrams. *Computer Physics Communications*, 2023. 290: p. 108790.
- [86] S. Zhong, Q. Shi, Y. Deng, Y. Sun, C. Politis, and S. Yang, High-performance zirconia ceramic additively manufactured via NanoParticle Jetting. *Ceramics International*, 2022. 48(22): p. 33485-33498.
- [87] P. Ma, C. Zhao, X. Lu, C. Gong, and X. Niu, Rotation error measurement technology and experimentation research of high-precision hydrostatic spindle. *The International Journal of Advanced Manufacturing Technology*, 2014. 73: p. 1313-1320.

## References

---

- [88] B. Davies, K. Fan, R. Hibberd, M. Jakopec, and S. Harris. Acrobot-using robots and surgeons synergistically in knee surgery. in 1997 8th International Conference on Advanced Robotics. Proceedings. ICAR'97. 1997. IEEE.
- [89] J. Xu, C. Wang, P. Feng, E. Jiang, and F. Feng, Meso-scale cracks initiation of Nomex honeycomb composites in orthogonal cutting with a straight blade cutter. *Composites Science and Technology*, 2023. 233: p. 109914.
- [90] D.R. Carter and D.M. Spengler, Mechanical properties and composition of cortical bone. *Clinical Orthopaedics and Related Research (1976-2007)*, 1978. 135: p. 192-217.
- [91] S.M. Ott, Cortical or trabecular bone: what's the difference? *American journal of nephrology*, 2018. 47(6): p. 373-376.
- [92] F.D. Burstein, C. Simms, S.R. Cohen, F. Work, and M. Paschal, Iliac crest bone graft harvesting techniques: a comparison. *Plastic and reconstructive surgery*, 2000. 105(1): p. 34-39.
- [93] F.-L. Zavalan and A. Rona, A workflow for designing contoured axisymmetric nozzles for enhancing additively manufactured cold spray deposits. *Additive Manufacturing*, 2023. 62: p. 103379.
- [94] S. Garmeh, M. Jadidi, and A. Dolatabadi, Three-Dimensional Modeling of Cold Spray for Additive Manufacturing. *Journal of Thermal Spray Technology*, 2020. 29(1): p. 38-50.

- 
- [95] J. Roberts, P. Wypych, D. Hastie, and R. Liao, Analysis and validation of a CFD-DPM method for simulating dust suppression sprays. *Particulate Science And Technology*, 2021(459): p. 1-12.
- [96] G.C. Van Rhoon, T. Samaras, P.S. Yarmolenko, M.W. Dewhirst, E. Neufeld, and N. Kuster, CEM43° C thermal dose thresholds: a potential guide for magnetic resonance radiofrequency exposure levels? *European radiology*, 2013. 23: p. 2215-2227.
- [97] H. Deramond, N. Wright, and S. Belkoff, Temperature elevation caused by bone cement polymerization during vertebroplasty. *Bone*, 1999. 25(2): p. 17S-21S.
- [98] E. Alp, D. Bijl, R.P. Bleichrodt, B. Hansson, and A. Voss, Surgical smoke and infection control. *Journal of Hospital Infection*, 2006. 62(1): p. 1-5.
- [99] L. Zhang, B.L. Tai, G. Wang, K. Zhang, S. Sullivan, and A.J. Shih, Thermal model to investigate the temperature in bone grinding for skull base neurosurgery. *Medical engineering & physics*, 2013. 35(10): p. 1391-1398.
- [100] A. Abbott, T. Gibson, G.P. Tandon, L. Hu, R. Avakian, J. Baur, and H. Koerner, Melt extrusion and additive manufacturing of a thermosetting polyimide. *Additive Manufacturing*, 2021. 37: p. 101636.
- [101] C. Tian, X. Li, Z. Chen, G. Guo, L. Wang, and Y. Rong, Study on formability, mechanical property and finite element modeling of 3D-printed composite for metal-bonded diamond grinding wheel application. *Journal of Manufacturing Processes*, 2020. 54: p. 38-47.

## References

---

- [102] J. Zhang, R. Hong, and H. Wang, 3D-printed functionally-graded lattice structure with tunable removal characteristics for precision polishing. *Additive Manufacturing*, 2022. 59: p. 103152.
- [103] P.P. Nalavade, P. Soni, V. Salokhe, and T. Niyamapa, Comparative performance of standard, notched and spiral-notched tillage discs. *Int. Agric. Eng. J*, 2011. 20: p. 18-26.
- [104] R. Vignesh and N. Arunachalam, Design and development of spiral grooved grinding wheel and their influence on the performance of vertical surface grinding process. *Procedia Manufacturing*, 2021. 53: p. 251-259.
- [105] R. Agarwal, V. Gupta, and J. Singh, orthopaedic bone drilling: An experimental and histological study. *Applied Acoustics*, 2023. 211: p. 109520.
- [106] B. Wang, Y. Zhao, G. Liu, C.K. Thein, W. Su, S. Long, H. Qi, P. Wei, Y. He, and H.N. Li, Preventing Thermal Osteonecrosis through 3D Printed Ceramic Grinding Tool. *Additive Manufacturing*, 2023: p. 103878.
- [107] H. Quan, C. Ren, Y. He, F. Wang, S. Dong, and H. Jiang, Application of biomaterials in treating early osteonecrosis of the femoral head: Research progress and future perspectives. *Acta Biomaterialia*, 2023. 164: p. 15-73.
- [108] L. Arbeloa-Gutierrez, C.S. Dean, J. Chahla, and C. Pascual-Garrido, Core Decompression Augmented With Autologous Bone Marrow Aspiration

- Concentrate for Early Avascular Necrosis of the Femoral Head. *Arthroscopy Techniques*, 2016. 5(3): p. e615-e620.
- [109] R.S. Kamrani, E. Najafi, H. Azizi, and L. Oryadi Zanjani, Outcomes of Arthroscopic Lunate Core Decompression Versus Radial Osteotomy in Treatment of Kienböck Disease. *The Journal of Hand Surgery*, 2022. 47(7): p. 692.e1-692.e8.
- [110] D. Li, S. Sun, Z. Yang, Y. Luo, and P. Kang, Efficacy of Modified Lightbulb Technique by Percutaneous Femoral Neck-Head Fenestration Combined With Compacted Artificial Bone Graft for Treating Precollapse Osteonecrosis of the Femoral Head. *The Journal of Arthroplasty*, 2023.
- [111] Y. Xu, H. Pan, R. Wang, Q. Du, and L. Lu, New families of triply periodic minimal surface-like shell lattices. *Additive Manufacturing*, 2023. 77: p. 103779.
- [112] S. Wang, L. Zhang, M. Tang, C. Cai, J. Wu, Z. Zhang, and Y. Shi, Field-driven design and performance evaluation of dual functionally graded triply periodic minimal surface structures for additive manufacturing. *Materials & Design*, 2023. 233: p. 112257.
- [113] M. Li, J. Jiang, W. Liu, X. Huang, X. Wu, W. Wei, H. Zhu, J. Zhang, J. Xiao, and H. Dai, Bioadaptable bioactive glass- $\beta$ -tricalcium phosphate scaffolds with TPMS-gyroid structure by stereolithography for bone regeneration. *Journal of Materials Science & Technology*, 2023. 155: p. 54-65.

## References

---

- [114] S. Seehanam, W. Chanchareon, and P. Promoppatum, Assessing the effect of manufacturing defects and non-Newtonian blood model on flow behaviors of additively manufactured Gyroid TPMS structures. *Heliyon*, 2023. 9(5): p. e15711.
- [115] L. Zhu, H. Li, and W. Wang, Research on rotary surface topography by orthogonal turn-milling. *The International Journal of Advanced Manufacturing Technology*, 2013. 69(9): p. 2279-2292.
- [116] H. Lei, T. Yi, H. Fan, X. Pei, L. Wu, F. Xing, M. Li, L. Liu, C. Zhou, Y. Fan, and X. Zhang, Customized additive manufacturing of porous Ti6Al4V scaffold with micro-topological structures to regulate cell behavior in bone tissue engineering. *Materials Science and Engineering: C*, 2021. 120: p. 111789.
- [117] J. Li, W. Hou, Y. Yang, Q. Deng, H. Fu, Y. Yin, K. Duan, B. Feng, T. Guo, and J. Weng, Micro/nano-topography promotes osteogenic differentiation of bone marrow stem cells by regulating periostin expression. *Colloids and Surfaces B: Biointerfaces*, 2022. 218: p. 112700.
- [118] B. Huang, C. Li, Y. Zhang, W. Ding, M. Yang, Y. Yang, H. Zhai, X. Xu, D. Wang, S. Debnath, M. Jamil, H.N. Li, H.M. Ali, M.K. Gupta, and Z. Said, Advances in fabrication of ceramic corundum abrasives based on sol–gel process. *Chinese Journal of Aeronautics*, 2021. 34(6): p. 1-17.
- [119] N. Dixit, S.D. Maurya, and B.P. Sagar, Sustained release drug delivery system. *Indian Journal of Research in Pharmacy and Biotechnology*, 2013. 1(3): p. 305.

- 
- [120] M. Mat, A quantitative analysis of ascorbic acid in vitamin C related products by high performance liquid chromatography. 2014.
- [121] H.A.M. Marzook, E.A. Yousef, M. Denewar, and M.R.L. Farahat, In-vitro assessment of bone viability with different implant drill speeds. *British Journal of Oral and Maxillofacial Surgery*, 2020. 58(10): p. e301-e306.
- [122] H.N. Li and D. Axinte, On a stochastically grain-discretised model for 2D/3D temperature mapping prediction in grinding. *International Journal of Machine Tools and Manufacture*, 2017. 116: p. 60-76.
- [123] H.N. Li, T.B. Yu, Z.X. Wang, L.D. Zhu, and W.S. Wang, Detailed modeling of cutting forces in grinding process considering variable stages of grain-workpiece micro interactions. *International Journal of Mechanical Sciences*, 2017. 126: p. 319-339.
- [124] K. Yagihara, S. Okabe, J. Ishii, T. Amagasa, M. Yamashiro, S. Yamaguchi, S. Yokoya, T. Yamazaki, and Y. Kinoshita, Mandibular reconstruction using a poly(l-lactide) mesh combined with autogenous particulate cancellous bone and marrow: a prospective clinical study. *International Journal of Oral and Maxillofacial Surgery*, 2013. 42(8): p. 962-969.
- [125] G. Borciani, G. Montalbano, N. Baldini, G. Cerqueni, C. Vitale-Brovarone, and G. Ciapetti, Co-culture systems of osteoblasts and osteoclasts: Simulating in vitro bone remodeling in regenerative approaches. *Acta Biomaterialia*, 2020. 108: p. 22-45.

## References

---

- [126] M. Shen, Y. Li, F. Lu, Y. Gou, C. Zhong, S. He, C. Zhao, G. Yang, L. Zhang, X. Yang, Z. Gou, and S. Xu, Bioceramic scaffolds with triply periodic minimal surface architectures guide early-stage bone regeneration. *Bioactive Materials*, 2023. 25: p. 374-386.
- [127] F. Baino, G. Magnaterra, E. Fiume, A. Schiavi, L.P. Tofan, M. Schwentenwein, and E. Verné, Digital light processing stereolithography of hydroxyapatite scaffolds with bone-like architecture, permeability, and mechanical properties. *Journal of the American Ceramic Society*, 2022. 105(3): p. 1648-1657.